RESONANT OPTICAL NONLINEARITIES IN CASCADE AND COUPLED QUANTUM WELL STRUCTURES

A Dissertation

by

FENG XIE

Submitted to the Office of Graduate Studies of
Texas A&M University
in partial fulfillment of the requirements for the degree of

DOCTOR OF PHILOSOPHY

December 2008

Major Subject: Applied Physics

RESONANT OPTICAL NONLINEARITIES IN CASCADE AND COUPLED QUANTUM WELL STRUCTURES

A Dissertation

by

FENG XIE

Submitted to the Office of Graduate Studies of
Texas A&M University
in partial fulfillment of the requirements for the degree of

DOCTOR OF PHILOSOPHY

Approved by:

Chair of Committee,	Alexey Belyanin
Committee Members,	Vitaly Kocharovsky
	Jairo Sinova
	Yue Kuo
Head of Department,	Edward Fry

December 2008

Major Subject: Applied Physics

ABSTRACT

Resonant Optical Nonlinearities in Cascade and Coupled Quantum Well Structures.

(December 2008)

Feng Xie, B.S.; M.S., University of Science and Technology of China

Chair of Advisory Committee: Dr. Alexey Belyanin

Resonant or near resonant optical nonlinearities in semiconductor coupled quantum-well systems are discussed. Quantum engineered coupled or cascade quantum-well structures can provide giant nonlinear susceptibilities for various optical nonlinear processes. Nonlinearities integrated within quantum cascade lasers (QCL) showed great potential in various applications in the infrared range. Several schemes of nonlinearities are proposed and discussed in this work.

Integrating difference frequency generation (DFG) with QCL can yield long wavelength radiation, such as terahertz light. The DFG process does not require population inversion at a transition associated with low photon energy; however, this requirement is necessary to lasers, such as QCL, and is hard to meet, because of the thermal backfilling and inefficient injection or pumping at room temperature. Therefore terahertz radiation due to DFG QCL for room temperature is proposed. On the other hand, the second harmonic generation can double laser frequency, and then push radiation frequency of AlInAs/GaInAs/InP based QCL to short wavelengths such as 3 μm and shorter.

Optical nonlinearities can extend working frequencies of light sources, and also can help to improve light detection. For example, a sum frequency generation can up-convert mid/far-IR signal into near-IR signal with strong near-IR pump light, namely high efficient near-IR photon detector could be employed to detect mid/far-IR light. A specific designed quantum well structure of this frequency up-conversion scheme is discussed.

A scheme of monolithic in-plane integration of the optical nonlinearities with QCL is also proposed. In this scheme, an optical nonlinear section is made from the same quantum well structure of a QCL, and is under an independent applied bias. Due to the independence of the applied bias, the nonlinearities can be tuned flexibly. In particular, a widely tunable Raman laser based on this scheme could be achieved.

A frequency up-conversion based on sum frequency generation process in coupled quantum-well structure is also proposed for mid-infrared detection. By converting mid-IR signal to near-IR, superior near-IR detector such as silicon avalanche photo diode (APD) can be employed. The scheme can provide lower noise equivalent power (NEP) or higher detectivity compared with regular semiconductor photo detectors.

A scheme of lasing without inversion (LWI) based on QCL for THz radiation is proposed. A ladder type three-level system for LWI process is integrated into a bound-to-continue high power QCL at 10 μm. The proposed LWI generates THz signal at 69 μm. An optical gain about 80 cm^{-1} is achieved, against a waveguide loss about 30 cm^{-1} in a semi insulator (SI) surface plasmon waveguide.

ACKNOWLEDGEMENTS

I would like to thank my committee chair, Dr. Belyanin, and my committee members, Dr. Kocharovsky, Dr. Sinova, and Dr. Kuo, for their guidance and support throughout the course of this research.

Thanks also go to Dr. Wojcik in our group, my friends and colleagues and the department faculty and staff for making my time at Texas A&M University a great experience. I also want to thank Dr. Gmachl at Princeton University, Dr. Capasso at Harvard University, and Dr. Kono at Rice University, who provided me great opportunities to participate in various experimental projects, that were essential to this dissertation work. I also want to extend my gratitude to the National Education Foundation, MIRTHE (Mid-InfraRed Technologies for Health and the Environment) program which provided financial support for my research.

Finally, thanks to my mother and father for their encouragement and to my fiancée for her patience and love.

TABLE OF CONTENTS

Page

ABSTRACT iii

ACKNOWLEDGEMENTS v

TABLE OF CONTENTS vi

LIST OF FIGURES viii

LIST OF TABLES xii

1. INTRODUCTION 1

    1.1 Nonlinear Optics and Nonlinear Susceptibilities 1
    1.2 Quantum-Well Structures and Intersubband Transitions 8
    1.3 Optical Nonlinearities in Quantum-Well Structures 11
    1.4 Quantum Cascade Lasers 13
    1.5 Integrating Optical Nonlinearities with Quantum Cascade Lasers 18
    1.6 Waveguide and Phase Matching Consideration in Optical Nonlinear QCLs 21

2. ROOM TEMPERATURE TERAHERTZ SOURCE BASED ON DIFFERENCE FREQUENCY QUANTUM CASCADE LASERS 25

    2.1 Introduction 25
    2.2 Difference Frequency Generation in a QCL and the Nonlinear Susceptibility 27
    2.3 Laser Gain Spectra and Two Wavelength Operation 33
    2.4 A New Design of THz DFG Quantum Cascade Laser with Doubled Resonant Nonlinear Active Cores 34
    2.5 The Experimental Results of DFG QCL Device N970A 39

3. SECOND HARMONIC GENERATION QUANTUM CASCADE LASER AND THE CHARACTERIZATION OF THE OPTICAL NONLINEARITRY 46

    3.1 Introduction 46

Page

3.2 The Design of SHG QCL Device D3056 and the Second Order Susceptibility 47
3.3 The Experimental Setup and Results for Device D3056 49
3.4 The Analysis of the Nonlinear Susceptibility of SHG in Device 3056 54

4. IN-PLANE MONOLITHIC INTEGRATION OF NONLINEARITIES WITH QCL 61

4.1 Introduction 61
4.2 The Scheme of In-Plane Integration 62
4.3 Widely Tunable Raman Laser Based on the In-Plane Integration Scheme 64
4.4 The In-Plane Integration for Second Harmonic Generation 69

5. FREQUENCY UP-CONVERSION IN COUPLED QUANTUM-WELL STRUCTURE FOR MID/FAR-IR DETECTION 72

5.1 Introduction 72
5.2 Frequency Up-Conversion Scheme with Quantum-Well Structures ... 76
5.3 The Nonlinear Susceptibility for Frequency Up-Conversion 78
5.4 Optimization of Double Quantum-Well Structure for Frequency Up-Conversion 81
5.5 The Optical Geometry for the Frequency Up-Conversion Scheme 84
5.6 The Figure of Merit of Frequency Up-Conversion Scheme for Mid-IR Detection 86

6. LASING WITHOUT INVERSION IN THE QUANTUM CASCADE LASER FOR TERAHERTZ EMISSION 89

6.1 Introduction 89
6.2 The Upper Ladder Scheme of LWI and the Basic Equations 91
6.3 The Quantum-Well Structure of a QCL for LWI at THz 96
6.4 The Waveguide Design for THz Radiation 98

7. SUMMARY AND FUTURE WORK 101

REFERENCES 103

VITA 111

LIST OF FIGURES

FIGURE		Page
1.1	The sketch of a three-level system	3
1.2	A sketch of a Type I semiconductor quantum-well structure	8
1.3	The sketch of an intersubband transition and an inter-band transition, where C_1 and C_2 are two subbands of the conduction band and V_1 is one of the valence subbands	9
1.4	Four configurations of asymmetric quantum-well structures.	13
1.5	A summary plot of (a) maximum CW operation temperature, and (b) maximum CW power at room temperature of high performance QCLs	14
1.6	The Band diagram of a typical quantum cascade laser, including laser active layers forming laser upper level 3 and lower level 2, and injector layers.	15
1.7	The structure of a typical quantum cascade laser	16
1.8	The band diagram of the SHG QCL	19
1.9	The band-diagram of one period of Raman injection laser	20
1.10	The dispersion of refractive indices in GaAs material	22
1.11	The waveguide structure of a SHG QCL	23
1.12	Different dispersion relationships of effective refractive indices of TM_0 and TM_2 modes with the width of the waveguide.	23
2.1	A typical three-level system for difference frequency generation process.	27
2.2	The band diagram of the DFG QCL design	28
2.3	The waveguide modes for fundamental frequencies and DFG frequency.	32
2.4	Three level system with one lasing transition 3-2	33

FIGURE Page

2.5 The scratches of gain spectra indicate two wavelengths operation. 35

2.6 The band diagrams of two active layers, under a bias of 30kV/cm. 36

2.7 The gain spectrum of new DFG QCL design has two peaks. 37

2.8 The profiles of absolute values of nonlinear susceptibilities of (a) laser 'a' and (b) laser 'b'. The dashed lines indicate the frequencies of the other working laser. 38

2.9 The experimental setup for the measurement of a DFG QCL 39

2.10 Mid-IR emission spectra at 80K, 150K, 250K and 300K.. 41

2.11 The total mid-IR peak power of the device at various temperatures versus the pump current 42

2.12 THz emission of the device N970A at various temperatures from 80K to 250K. 42

2.13 The peak power of THz emission versus the product of two mid-IR powers at 80K, showing the maximum peak power reached 1.5 μW.. 43

2.14 The spectra simulation matched the experimental results. 45

3.1 The band diagram with modulus squared of essential electron wave functions 48

3.2 The spectra of fundamental pump light. 50

3.3 The spectra of SHG signal at various injection current 51

3.4 The L-I-V curve of device D3056 51

3.5 The nonlinear power conversion efficiency vs the pump current. 52

3.6 The schematic of electron energy states in laser active region. 54

3.7 The experimental result of the second order susceptibility and simulation results from two methods 58

3.8 The band diagrams of device D3056 at (a) 41 kV/cm, and (b) 45 kV/cm . 60

FIGURE Page

4.1 The scheme of the vertical integration of nonlinearities with QCL. 62

4.2 The scheme of in-plane integration of nonlinearities. 63

4.3 The QCL structure under different biases. 67

4.4 The band diagrams of a couple double quantum-well structure. 70

5.1 Detectivity curves for various type infrared photodetectors at room temperature and the background limit. 74

5.2 The scheme of frequency up-conversion.. 75

5.3 A sketch of near-resonant SFG employing interband and intersubband transitions, (a), or intersubband transition only, (b), ... 75

5.4 The profile of cascade double wells structure for frequency-up conversion scheme. 77

5.5 The band diagram of the double quantum-well structure for the frequency up-conversion. 77

5.6 The sketch of band dispersion of conduction and valence subbands vs $k_{\|}$ vector. 79

5.7 The spectrum of absolute square of $\chi^{(2)}$ vs detuning $\Delta_{v\text{-}c2}$ with 20 meV detuning of pump. 81

5.8 The asymmetric effect of the product of dipole moments. 82

5.9 The asymmetry ratio of energy separation of states e_1 and e_2 82

5.10 The effects of total thickness on the energy separation of states e_1 and e_2, and the product of three dipole moments. 83

5.11 The optical geometry of the quantum-well structure for mid-IR detection frequency up-conversion. 84

6.1 Various schemes of LWI in three-level systems 90

6.2 The upper ladder scheme of a three-level system. 91

FIGURE Page

6.3 The band structure under applied electric field of 43 kV/cm.. 97

6.4 The scheme of (a) the semi-insulator (SI) surface plasmon waveguide, and (b) the metal-metal waveguide structures..... 99

6.5 The refractive index profile (the black line), and the TM mode profile (green line) with a 2DEG surface plasmon waveguide. 100

LIST OF TABLES

TABLE Page

3.1 (a) Parameters of transitions between energy states from 1 to 4..... 57

3.1 (b) Life time τ from energy states to injector..... 57

4.1 Parameters of energy separation and dipole moments at different applied electric fields. 68

6.1 The life time of transitions from level 1, 2 and 3. 98

1. INTRODUCTION

1.1 Nonlinear Optics and Nonlinear Susceptibilities

The field of nonlinear optics began in 1961, when the first second-harmonic generation was observed by Franken and co-workers [1]. It is basically the study of the interaction of intense laser light with matter. Most nonlinear optical phenomena involve frequency change due to the nonlinear response of a material system to the strength of the optical field. Therefore, optical nonlinearities are largely used to modify the frequency of laser light in order to extend the spectral range of coherent light sources for various applications.

In an optical medium, the response of optical field, or the dielectric polarization $\widetilde{P}(t)$, depends on the strength of the applied optical field $\widetilde{E}(t)$ and some constants of proportionality, which are known as susceptibilities, as described in Eq. (1.1).

$$\widetilde{P}(t) = \chi^{(1)}\widetilde{E}(t) + \chi^{(2)}\widetilde{E}^2(t) + \chi^{(3)}\widetilde{E}^3(t) + \cdots, \qquad (1.1)$$

where $\chi^{(1)}$ is linear susceptibility. $\chi^{(2)}$ and $\chi^{(3)}$ are the second and third-order nonlinear susceptibilities respectively. With other higher order terms, they are called nonlinear susceptibilities. Starting from Maxwell's equations, we have the equation:

This dissertation follows the style and format of *Applied Physics Letter*.

$$-\nabla^2\widetilde{E}+\frac{1}{c^2}\frac{\partial^2}{\partial t^2}\widetilde{E}=-\frac{4\pi}{c^2}\frac{\partial^2}{\partial t^2}\widetilde{P}\ , \qquad (1.2)$$

where we can split the $\widetilde{P}(t)$ into linear and nonlinear parts as:

$$\widetilde{P}(t)=\widetilde{P}^{(1)}+\widetilde{P}^{NL}\ . \qquad (1.3)$$

However, given the linear term of the displacement field $\widetilde{D}$ as

$$\widetilde{D}=\widetilde{E}+4\pi\widetilde{P}^{(1)}=\varepsilon^{(1)}\widetilde{E}\ , \qquad (1.4)$$

the wave equation (1.2) becomes

$$-\nabla^2\widetilde{E}+\frac{\varepsilon^{(1)}}{c^2}\frac{\partial^2}{\partial t^2}\widetilde{E}=-\frac{4\pi}{c^2}\frac{\partial^2}{\partial t^2}\widetilde{P}^{NL}\ . \qquad (1.5)$$

In this equation, the nonlinear polarization acts as a source term of a wave equation, which results in the generation of electric field at the nonlinear frequency [1].

There are various nonlinear optical processes. Some of them involve generation of new frequency which is different from that of pump source, some other do not. The former includes second harmonic generation (SHG), sum frequency generation (SFG), and different frequency generation (DFG). They are also the topics that will be involved in this thesis. The later one includes optical Kerr effect which is the reason of self-focusing effect, and two photon absorption, in which a single electron absorbs two photons simultaneously. Those will not be discussed in here.

The processes of SHG, SFG and DFG are all due to the second order optical nonlinearity. As mentioned above, in this case, the nonlinear polarization can be simply described as:

$$\widetilde{P}^{(2)}=\chi^{(2)}\widetilde{E}_1\widetilde{E}_2\ , \qquad (1.6)$$

where $\widetilde{E}_1$ and $\widetilde{E}_2$ are electric fields of two mixed optical fields, and they can be represented as the discrete sum of a number of frequency components as [1]:

$$\widetilde{E}_i(r,t) = \sum_n E_i(\omega_n) e^{-i\omega_n t} + c.c. \ , \qquad (1.7)$$

We also can do similar thing for the polarization. At each frequency component, the equation of (1.6) can be rewritten as:

$$P^{(2)}(\omega_3) = \chi^{(2)}(\omega_1, \omega_2, \omega_3) E_1(\omega_1) E_2(\omega_2) \ . \qquad (1.8)$$

This equation can be suitable for all the second order nonlinearities. For the second harmonic generation, E_1 and E_2 should be identical, and so are ω_1 and ω_2, while we have $\omega_3 = 2\omega_1 = 2\omega_2$. For the SFG or DFG case, we just have the relationship $\omega_3 = \omega_1 + \omega_2$, or $\omega_3 = \omega_1 - \omega_2$ respectively. However, the second order susceptibility $\chi^{(2)}$ is different for different cases.

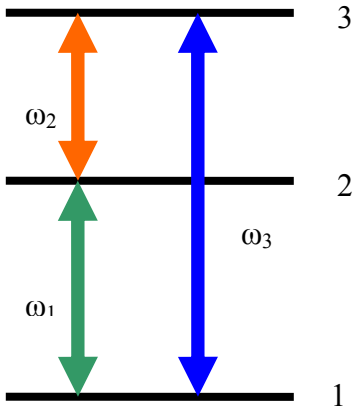

Fig. 1.1. The sketch of a three-level system. It includes energy states 1, 2, and 3, in the presence of three optical fields, at frequency of ω_1, ω_2, and ω_3 respectively.

The second-order susceptibility is an intrinsic property of a material system. It can be calculated with density matrix formalism of quantum mechanics. For example, in a material system, such as an atomic system with many energy states, any three energy states can form a system, which sometimes is called a three-level system, as shown in Fig. 1.1.

Given the Hamiltonian operator $\hat{H}$ of the system, the density matrix equation of this system can be written as:

$$\dot{\rho}_{nm} = \frac{-i}{\hbar}[\hat{H}, \hat{\rho}]_{nm} \ , \tag{1.9}$$

where ρ_{nm} is the density matrix element, *n* and *m* are the indices of energy levels or states. If the decay rate γ_{nm} of each density matrix element is counted, then under a certain approximation the equation has the form:

$$\dot{\rho}_{nm} = \frac{-i}{\hbar}[\hat{H}, \hat{\rho}]_{nm} - \gamma_{nm}(\rho_{nm} - \rho_{nm}^{eq}) \ , \tag{1.10}$$

where ρ_{nm}^{eq} is the equilibrium value of density matrix element.

With the presence of an external electric field, we can simply write down the Hamiltonian as

$$\hat{H} = \hat{H}_0 + \hat{V}(t) = \hat{H}_0 - \hat{\mu} \cdot \tilde{E}(t) \ , \tag{1.11}$$

where $\hat{H}_0$ represents the Hamiltonian of a free atomic system, and $\hat{V}(t)$ is the energy of interaction of the system and external electric field $\tilde{E}(t)$, with the electric dipole moment operator $\hat{\mu} = -e\hat{r}$. Then the equation (1.10) can be expended to the form:

$$\dot{\rho}_{nm} = -i\omega_{nm}\rho_{nm} - \frac{i}{\hbar}\sum_{v}(V_{nv}\rho_{vm} - \rho_{nv}V_{vm}) - \gamma_{nm}(\rho_{nm} - \rho_{nm}^{eq}), \tag{1.12}$$

where we define the transition frequency as

$$\omega_{nm} = \frac{E_n - E_m}{\hbar}. \tag{1.13}$$

In most physical problems, we can solve (1.12) approximately. For small perturbation or weak interaction, we are looking for the solution similar to

$$\rho_{nm} = \rho_{nm}^{(0)} + \lambda\rho_{nm}^{(1)} + \lambda\rho_{nm}^{(2)} + \cdots, \tag{1.14}$$

where λ is a factor proportional to the energy of interaction. By applying perturbation theory of quantum mechanics and combining Eq. (1.12) and (1.11), we can solve the density matrix equations and get the first three orders of density matrix elements as [1]

$$\rho_{nm}^{(0)} = \rho_{nm}^{eq}, \tag{1.15}$$

$$\rho_{nm}^{(1)} = \frac{\rho_{mm}^{(0)} - \rho_{nn}^{(0)}}{\hbar}\sum_{p}\frac{\mu_{nm}\cdot E(\omega_p)e^{-i\omega_p t}}{(\omega_{nm} - \omega_p) - i\gamma_{nm}}, \tag{1.16}$$

and

$$\begin{aligned}
\rho_{nm}^{(2)} &= \sum_{v}\sum_{pq} e^{-i(\omega_p+\omega_q)t} \times \\
&\{\frac{\rho_{mm}^{(0)} - \rho_{vv}^{(0)}}{\hbar^2}\frac{[\mu_{nv}\cdot E(\omega_q)][\mu_{vm}\cdot E(\omega_p)]}{[(\omega_{nm} - \omega_p - \omega_q) - i\gamma_{nm}][(\omega_{vm} - \omega_p) - i\gamma_{vm}]} \\
&- \frac{\rho_{vv}^{(0)} - \rho_{nn}^{(0)}}{\hbar^2}\frac{[\mu_{nv}\cdot E(\omega_q)][\mu_{vm}\cdot E(\omega_p)]}{[(\omega_{nm} - \omega_p - \omega_q) - i\gamma_{nm}][(\omega_{nv} - \omega_p) - i\gamma_{nv}]}\} \\
&\equiv \sum_{v}\sum_{pq} K_{nmv}e^{-i(\omega_p+\omega_q)t}
\end{aligned}. \tag{1.17}$$

With the solution of density matrix elements, we are free to calculate the expectation value of any operator, including the induced dipole moment and polarization:

$$P = N\langle\tilde{\mu}\rangle = N \cdot tr(\hat{\rho}\hat{\mu}) = N(tr(\hat{\rho}^{(1)}\hat{\mu}) + tr(\hat{\rho}^{(2)}\hat{\mu}) + \cdots) \equiv P^{(1)} + P^{(2)} + \cdots \quad (1.18)$$

Consequently we have the expression for the second-order polarization as

$$P^{(2)}(\omega_p + \omega_q) = N\langle\tilde{\mu}(\omega_p + \omega_q)\rangle = N\sum_{nmv}\sum_{pq} K_{nmv}\mu_{mn} \quad . \quad (1.19)$$

We should keep in mind that all the variables of electric field, dielectric polarization, and dipole moment are vectors. Nevertheless, combining Eq. (1.18), (1.19), (1.8), and after a few steps of derivation, we obtain the second-order susceptibility tensor as

$$\chi^{(2)}_{ijk}(\omega_p + \omega_q, \omega_p, \omega_q) = \frac{N}{\hbar^2}\sum_{mnv} \{(\rho^{(0)}_{mm} - \rho^{(0)}_{vv})\frac{\mu^i_{nv}\mu^j_{mn}\mu^k_{vm}}{[(\omega_{nm} - \omega_p - \omega_q) - i\gamma_{nm}][(\omega_{vm} - \omega_p) - i\gamma_{vm}]} \quad , \quad (1.20)$$
$$-(\rho^{(0)}_{vv} - \rho^{(0)}_{nn})\frac{\mu^i_{nv}\mu^j_{mn}\mu^k_{vm}}{[(\omega_{nm} - \omega_p - \omega_q) - i\gamma_{nm}][(\omega_{nv} - \omega_p) - i\gamma_{nv}]}\}$$

where the indices *i*, *j*, *k* are used for coordinates, *m*, *n*, *v* are used for the number of energy states, *p,* and *q* are used for different photons at different frequencies.

Obviously, we obtain the second-order susceptibility for SFG process. However the Eq. (1.20) can also be used to describe SHG and DFG processes. When ω_p=ω_q, the Eq. (1.20) is automatically changed to the second-order susceptibility of SHG process; while if we substitute ω_p with -ω_p , we obtain the expression for DFG process. However, instead of having Eq. (1.8), we have relationship between dielectric polarization and electric field as:

$$P^{(2)}(2\omega) = \chi^{(2)}(2\omega, \omega)E^2(\omega), \quad (1.21)$$

for a SHG process, and

$$P^{(2)}(\omega_1 - \omega_2) = \chi^{(2)}(\omega_1 - \omega_2, \omega_1, \omega_2) E_1(\omega_1) E_2^*(\omega_2) , \tag{1.22}$$

for a DFG process.

In the thesis, the second-order nonlinearities will be discussed a lot, especially the SHG, SFG and DFG processes. The nonlinear susceptibilities will be directly taken from Eq. (1.20), although slight modification of formulas will be applied.

Due to the capability of switching frequency of a laser source, optical nonlinearities can be implemented in various applications. As mentioned above, the nonlinear susceptibility is an intrinsic property of a material system. Although all media can provide optical nonlinearities [2], for practical purposes an optical medium with a large nonlinear susceptibility is required in order to greatly enhance the interaction of photons. Otherwise the effect of optical nonlinearities is too weak to be observed, not even to be utilized in any application. The most widely used nonlinear material system is transparent crystals which have specific crystal symmetry, and usually an optical setup based on the nonlinear crystals is bulky and inconvenient.

Nowadays, people are looking for compact opto-electronics devices with low energy dissipation and low cost. Great progress in compact semiconductor laser systems has been achieved due to the development of semiconductor growth technologies. It also gives great opportunity of developing a new generation of nonlinear optical devices which can be integrated with nonlinear medium and compact laser source. In particular, combining optical nonlinearities within low-dimensional semiconductor heterostructures could be an interesting and attractive field of research.

1.2 Quantum-Well Structures and Intersubband Transitions

A typical low-dimensional semiconductor material system is a quantum-well structure. Semiconductor quantum-well structure is a material system built from two or more semiconductor materials, which can be III-V or II-IV compound semiconductor alloys, such as AlGaAs and GaInAs, on a substrate with the same or close lattice constant. The two semiconductor materials are grown alternately on each other, as shown in Fig. 1.2.

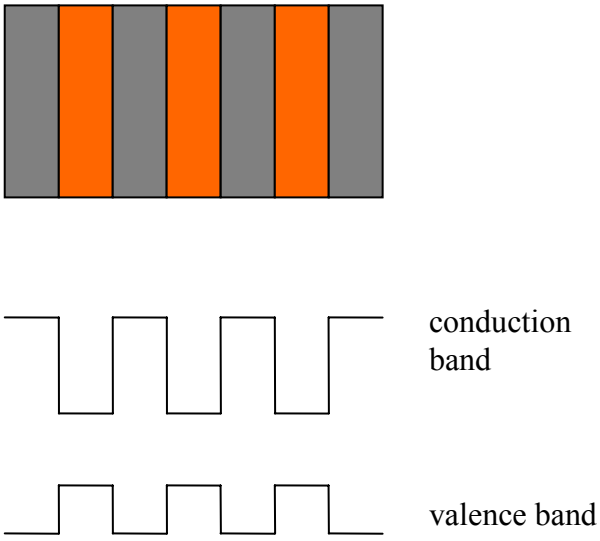

Fig. 1.2. A sketch of a Type I semiconductor quantum-well structure.

Due to the offset of conduction band and valence band between materials, electrons and holes are confined in the thin films' growth coordinate, and the quantum

confinement of electrons and holes makes conduction band and valence bands split into subbands. The transitions between subbands of the same conduction or valence band are called intersubband transitions (ISBT) [3-4], as shown in Fig. 1.3. On the opposite, the transitions between different bands, such as from the valence band to the conduction band, are called inter-band transitions (IBT).

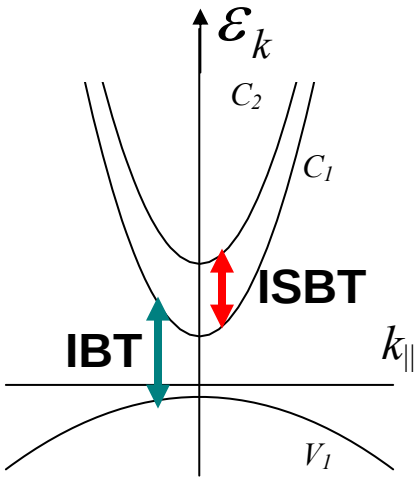

Fig. 1.3. The sketch of an intersubband transition and an inter-band transition, where C_1 and C_2 are two subbands of the conduction band and V_1 is one of the valence subbands.

Based on Kane's **k·P** theory [5], ISBTs have some unique features. In the quantum-well structure, the motion of carriers (electrons) is confined in the z-direction, which is the growth direction of semiconductor thin films. However, the carriers are not limited to move on the plane parallel to thin films. If we ignore a small non-parabolic effect, the energy of carriers can be described as

$$E = E_{ni} + \frac{\hbar^2 k_{||}^2}{2m_n^*}, \tag{1.23}$$

where E_{ni} is the energy eigen value of i-th subband of n-th energy band, $k_{||}$ is the momentum vector of carriers in the parallel plane, and m_n^* is the effective mass of carriers in the n-th energy band. Therefore, subbands from same energy band share almost the same energy dispersion in the $k_{||}$ space, especially around Γ-point. Based on this, optical ISBT has a very sharp absorption or emission spectrum, because the transition energy keeps the same for carriers at different $k_{||}$ values.

Other features of ISBTs include that an ISBT only couples with z-polarized electric field; and it has a parity selection rule different from IBTs [6]. For example, in a symmetric quantum-well structure, ISBT is only allowed when the difference of quantum numbers for subbands is odd [6], for the infinitely deep quantum-well approximation. In order to allow all transitions between subbands, the symmetry of a quantum-well structure must be broken. Compared to IBT and transitions between atomic states, the dipole moments of ISBT, especially in the conduction band, can be strong, and strong dipole moments are essential for giant optical nonlinearities. One reason for this is that energies for ISBTs are usually smaller than for IBTs and lie in the mid/far infrared range. More details will be discussed in later sections.

Another amazing feature of a quantum-well structure and ISBTs is that we can manipulate them as an artificial atom. Under the basic principle of quantum mechanics, the energy eigen-value of electrons (holes) energy state is determined by the thickness and depth of quantum wells. By adjusting the thicknesses of quantum wells and barriers,

one can modify the energy states on purpose, and also change the energy of ISBT or IBT. Moreover, one can also modify the shape of the wave functions and consequently design dipole moments and relaxation rates etc. It enables 'quantum engineering' of semiconductor quantum-well structures, which is greatly helpful to various optical devices design.

Last but not least, an ISBT is a very fast process. The transition time of ISBTs is usually at the scale of picoseconds and is determined by optical phonons, while the time scale of IBTs is in nanoseconds. The Modulator based on ISBTs had been investigated due to the potential high speed operation and high on/off ratio [7-8].

1.3 Optical Nonlinearities in Quantum-Well Structures

Large second order optical nonlinearities based on ISBTs in quantum-well structures were first predicted theoretically by Gurnick and DeTemple in 1983 [9]. Since then, different groups have observed giant second order nonlinearities in asymmetric quantum-well structures [10-20].

P. Boucaud *et al.* observed SHG process in asymmetric GaAs/AlGaAs quantum-well structures at 10.9 μm, and found giant nonlinear susceptibility about $7.2*10^{-7}$ m/V [12], which is about 1900 times greater than that found in bulk GaAs material. H. C. Liu *et al.* also found giant nonlinear susceptibility about $3.4*10^{-7}$ m/V for SFG process [17]. F. Capasso *et al.* found SHG and third harmonic generation (THG) in coupled quantum

well structures, with tunability by applied electrical bias on the quantum well structures [19]. M. J. Shaw *et al*. did pseudopotential calculation for second harmonic generation in p-type semiconductor quantum well structures [18]. They predicted and observed experimentally the nonlinear susceptibility 8 times larger than that in bulk GaAs material.

Overall, they observed mostly SHG or SFG processes in various types of quantum-well structures, and found giant nonlinear susceptibilities. Another common feature of their semiconductor material systems was that they were all asymmetric quantum-well structures, due to necessity to break symmetry to allow all transitions, as mentioned above. There were four different ways to break the symmetry, as shown in Fig. 1.4.

As mentioned before, the resonant frequency of SHG in asymmetric quantum wells is dependent on the thicknesses of wells and barriers. With the tunability by applying electrical bias, it opened an era of quantum engineering of optical nonlinearities. Due to the promising giant nonlinear susceptibility in quantum-well structures, optical nonlinearities have great potential application in various photonic devices.

Although with compact nonlinear quantum-well structures, the usefulness in nonlinear frequency conversion is still limited due to difficulties of efficiently coupling external optical pump with the ISBT nonlinearities and the lack of a suitable phase-matching scheme in most of III-V semiconductors. To integrate nonlinear optical elements with semiconductor lasers serving as optical pumps is the best solution to overcome the difficulties. Quantum Cascade laser (QCL) is one of such semiconductor lasers that can be easily integrated with nonlinear optical elements based on QW systems.

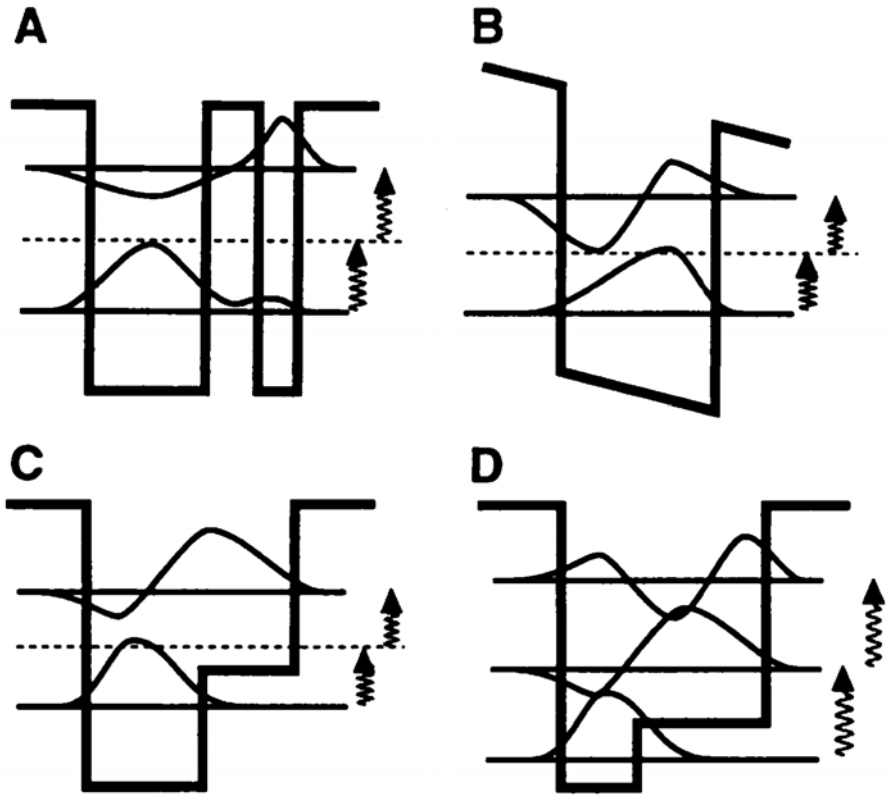

Fig.1.4. Four configurations of asymmetric quantum-well structures. (A) asymmetric coupled quantum wells; (B)electrically biased QWs; (C) step asymmetric QWs; where dash line are virtual states, arrows symbolize two photon process leading SHG. (D)Doubly resonant step asymmetric QWs with real intermediate state. [20]

1.4 Quantum Cascade Lasers

Quantum cascade laser (QCL) was theoretically proposed in 1970's [21], however, the first quantum cascade laser was demonstrated in 1994 [22]. After being rapidly developed for longer than a decade, QCLs have been demonstrated operating in a wide wavelength range, from 3 to 130 μm, and room temperature continuous wave (CW)

operation in the mid-IR range (4-10 μm) was achieved [23-45]. Now, QCL has become a powerful laser source at frequencies from near-IR to Terahertz. In the mid-IR range, the record high temperature for CW operation is about 400K, and the record high power at room temperature is about 680 mW, as shown in Fig. 1.5, which is a summary for high power and high temperature QCLs from various groups.

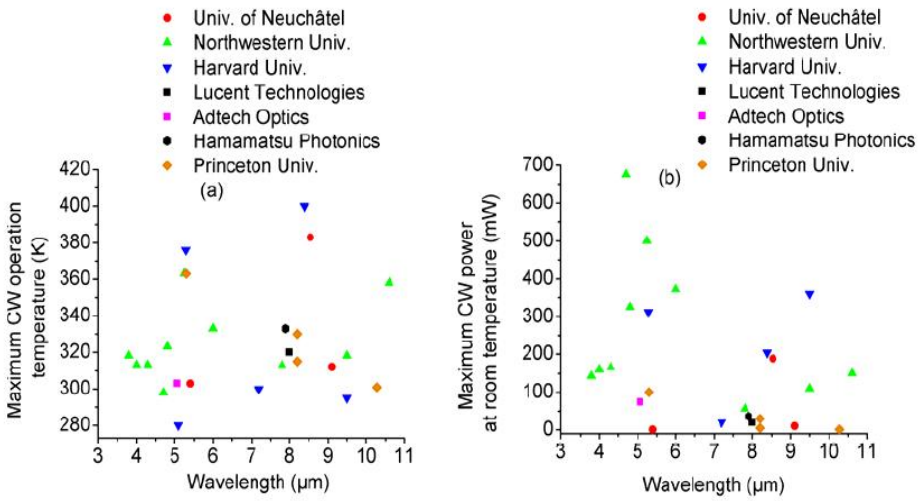

Fig. 1.5. A summary plot of (a) maximum CW operation temperature, and (b) maximum CW power at room temperature of high performance QCLs [46].

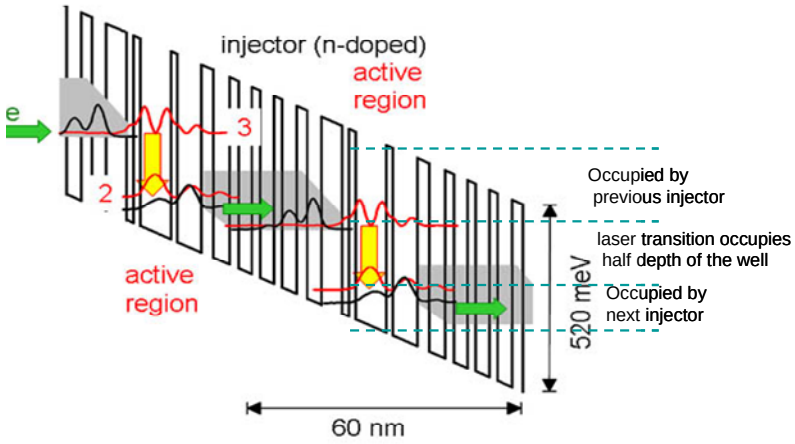

Fig.1.6. The Band diagram of a typical quantum cascade laser, including laser active layers forming laser upper level 3 and lower level 2, and injector layers. In the quantum well, laser transition can only occupy one third or half of the depth of well, because part of well is needed to accommodate previous and next injector.

QCL is a type of quantum device where fundamental properties such as the emission wavelength are the result of the design of the epitaxial layers, instead of being an intrinsic property of semiconductors. As a result, one stage of the electron energy states and the sequence of epitaxial semiconductor layers in a typical QCL, shown in Fig.1.6, is designed in such a way that the upper laser level in the active region is aligned with the previous injector, when the structure is under certain applied bias, and the lower laser level is aligned with the next injector, where each injector is made of a bunch of electron energy states, or a mini-band. Electrons are injected into the upper laser level and depleted from the lower lasing level through injectors. The dynamic process is very fast. The time scale of electron scattering is around one picosecond.

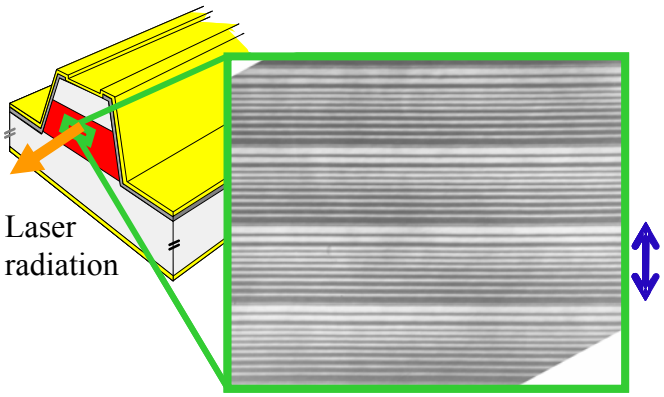

Fig.1.7. The structure of a typical quantum cascade laser. It includes a laser active core, cladding layers, an electrical contact layer (gold), and a substrate.

One QCL usually has 20-50 periods of active region. Every time one electron cascades down one stage it would emit a photon with energy of the laser transition. The stages of active region are grown on a substrate and covered by certain cladding and buffer layers, which form a waveguide to guide the radiation. After processing, a QCL device also has an insulating layer and a metal conducting layer which are used to apply pump electric current and bias to the device. A micro structure view of a QCL is shown in Fig. 1.7.

Although the quantum-well structures of QCL can be made from any two semiconductor materials, the majority of QCL are based on $Ga_{0.47}In_{0.53}As$/ $Al_{0.48}In_{0.52}As$ heterostructures lattice matched to InP substrate. However, the conduction band-offset in this heterostructure, or the difference of conduction bands of two semiconductor materials, is only 0.52 eV. It determines the depth of quantum well. Limited by the depth of quantum well, the photon energy of lasing transition is normally a few hundred milli-

electron-Volt (meV) for this material system, because QCL can not generate photons with energy larger than the depth of a quantum-well in QCL. Actually, the photon energy could barely be one third or one half the depth of quantum-well. The reason is the injectors in a QCL. In the energy diagram, as shown in Fig. 1.6, both upper and lower laser levels have to be located between previous and next neighbor injectors. However the energy levels of both previous and next injectors have to be lower than the top of quantum wells. Therefore the energy of a laser transition can only be about one third of the energy depth of a quantum-well.

The result is that QC lasers with lattice matched GaInAs/AlInAs materials system are not able to provide laser signal with wavelength shorter than 4μm. There are a few different methods to get around this obstacle. One is using lattice mismatched GaInAs/AlInAs material system, such as compressed $Ga_{0.36}In_{0.64}As$ and tensile $Al_{0.62}In_{0.38}As$ [31], which provides deeper quantum-well with band-offset about 700 meV- 900 meV.

One can also use antimony based semiconductor quantum-well structures, such as InAs/AlSb [35,36,39], GaSb/AlSb [37], or GaInAs/AlAsSb [40]. For example, a quantum-well structure of GaInAs/AlAsSb can provide quantum well depth of 1.6 eV. However, the problem with this type of material system is that the energy edge of X-valley or L-valley of the well or barrier material is located much lower than the top of the barrier at the Gamma-point. Electrons are very easily scattered into the X- or L-valley. Therefore one has to avoid design the laser transition across the X- or L-valley point at the energy band diagram, namely only a portion of the quantum well depth can

be utilized. Currently the shortest wavelength of this type of QCLs was pushed to 2.5 μm [39]. Similar situation happens in InAs (or InSbAs)/AlSb material systems, which can provide quantum well with depth of 1.3-1.6eV.

Another method is to use different design of QCLs, such as type-II quantum-well structures for inter-band QCLs [25], but people have to face more complicated design and structures. Last but not the least, we can combine or integrate optical nonlinearities with QCL.

1.5 Integrating Optical Nonlinearities with Quantum Cascade Lasers

As mentioned above, integrating optical nonlinearities with a laser system can switch the wavelength of the system. The wavelength of quantum cascade lasers can cover mid-IR and far-IR very well. However, it is difficult to build QCLs at shorter wavelength and longer wavelength, namely in the near-IR range, from 2μm to 4μm, and Terahertz range. Both regions are very important in various application fields such as telecommunication, molecular identification, and homeland security. Therefore, integrating optical nonlinearities with QCL and extending the operation wavelength to both shorter and longer wavelength region is an attractive topic.

Some pioneering work had been done, such as Raman injection QCL by M. Troccoli and A. Belyanin *et al.* [47], second harmonic generation QCL by N. Owschimikow and C. Gmachl *et al.* [48, 49], sum frequency generation QCL by J.-Y.

Bengloan *et al.* [50], and difference frequency generation QCL by M. Belkin and A. Belyanin *et al.* [51].

Due to the multi-quantum-well structures in QCL, there is artful method to integrate optical nonlinearities. People can manipulate the energy states in a laser active region and make them in such a way that giant nonlinearities are achieved inside the laser active region. For example, a three-level system for SHG is designed in the active layers of a QCL in ref. [49]. The band diagram of the SHG QCL is shown in Fig. 1.8. An energy state was purposely located over the upper lasing level with an energy separation close to the laser frequency. This energy state and two laser levels form a three-level system, which converts laser frequency to double frequency. With current shortest QCL wavelength, we expect to generate near-IR wavelengths up to 1.5 um.

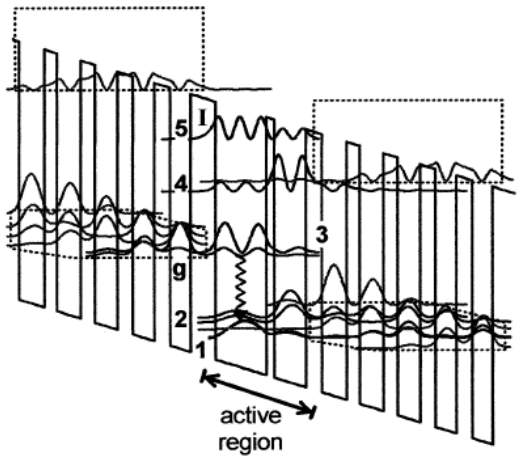

Fig. 1.8. The band diagram of the SHG QCL. One active region is sandwiched between two injector regions. Energy level 3 and 2 are the upper and lower lasing level respectively. Energy level 4 with 3 and 2 form a three level system. The QCL is designed to work at 9 μm, and SHG signal is 4.5 μm. [49]

The method of integrating nonlinearities within active region of a QCL can also be applied on other nonlinear optical QCLs, such as DFG QCL. The QCLs with DFG process must provide two lasing frequencies. Usually in this case, two active cores with different design and working at different frequency are stacked together. The three-level system for DFG process is then inserted into one of or both of the active cores [51]. More details will be discussed in the later section.

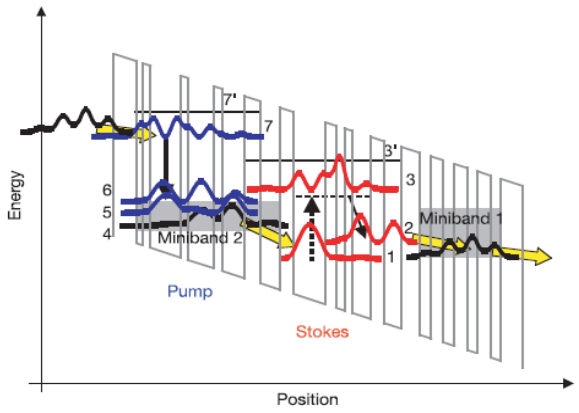

Fig. 1.9. The band-diagram of one period of Raman injection laser [57]. Level 7 and 5 are regular active regions of a QCL, which serves as a pump laser. Level 1, 2, and 3 form a Raman (Stokes) active region, which absorbs pump photons and emits photons at longer wavelength.

Another interesting example is Raman QCL. The first quantum-well based Raman laser utilizing external pump of a CO_2 laser was reported in 2001 [52]. However, if we could integrate Raman scattering with a QCL, we would obtain a compact Raman laser without bulky external pump and corresponding setup. The compact Raman injection laser was reported in 2005 [47]. Fig. 1.9 is the band diagram of the Raman

injection QCL. The motivation of making Raman QCL is to explore a new path to a widely tunable laser. It will be discussed in later section 4.

1.6 Waveguide and Phase Matching Consideration in Optical Nonlinear QCLs

In optical nonlinear processes, usually the phase matching should be achieved in order to achieve high efficiency. For example in the process of SHG, the intensity of doubled frequency in the absence of losses is [1]:

$$I(2\omega) = I_{\max} \frac{\sin^2(\Delta kL/2)}{(\Delta kL/2)^2}, \qquad (1.24)$$

where I_{max} is proportional to $I^2(\omega)$, L is the distance of light propagating in the nonlinear medium, and the wave-vector mismatch Δk can be expressed as

$$\Delta k = 2k(\omega) - k(2\omega). \qquad (1.25)$$

The condition of vanishing of wave-vector mismatch is

$$n(\omega) = n(2\omega). \qquad (1.26)$$

However, this usually is not true. In most cases, the dispersion of the refractive indices causes Eq. (1.26) invalid, as shown in Fig. 1.10.

There are a couple of methods people used to compensate phase mismatch. One of them is using different waveguide modes for different frequencies. In most of photonics devices, light propagates in a waveguide as a set of modes. The longitudinal mode of a semiconductor laser cavity is a standing wave pattern, and the transverse

modes are classified into different types, such as TE modes (transverse electric), TM modes (transverse magnetic), TEM modes, and hybrid modes. Usually in a QCL device, the laser transition, which is an ISBT, is only coupled with z-polarized electric field, and only TM modes survive. However, different transverse modes (even all TM modes), as shown in Fig.1.11, have different dispersion of effective refractive indices, which have different relationships with the width of waveguide, as shown in Fig. 1.12. Therefore, one can choose the right width of waveguide, and make the phase mismatch compensated. So, the phase matching is achieved.

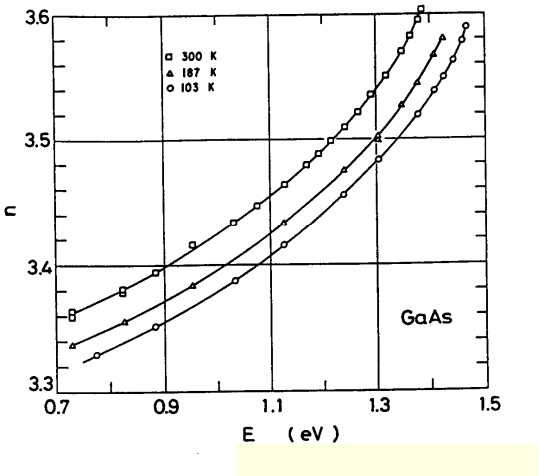

Fig. 1.10. The dispersion of refractive indices in GaAs material. In this case, n(2ω) is larger than n(ω).

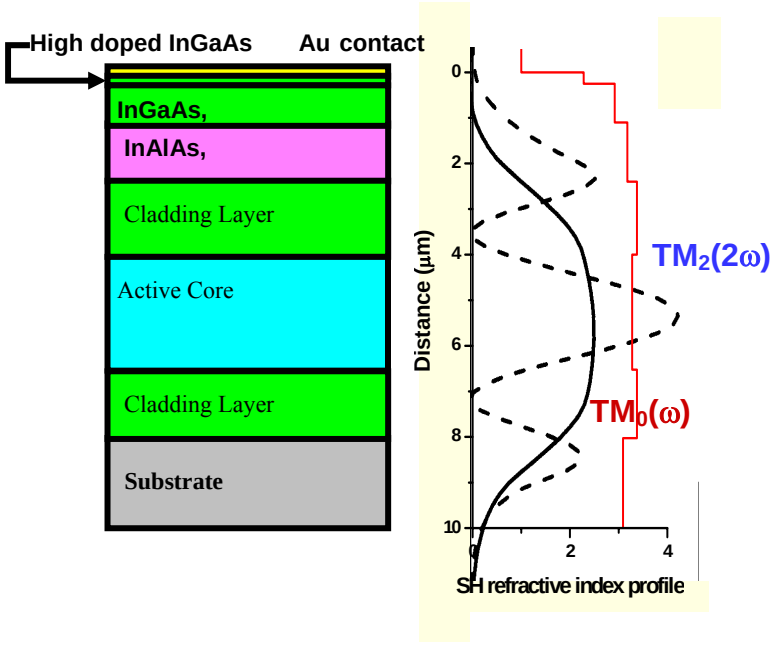

Fig. 1.11. The waveguide structure of a SHG QCL. Left is the layer structure of a SHG QCL. Right is refractive index (red thin line) profile and profiles of TM_0 and TM_2 modes. The former is the mode of fundamental frequency and the later is that of double frequency.

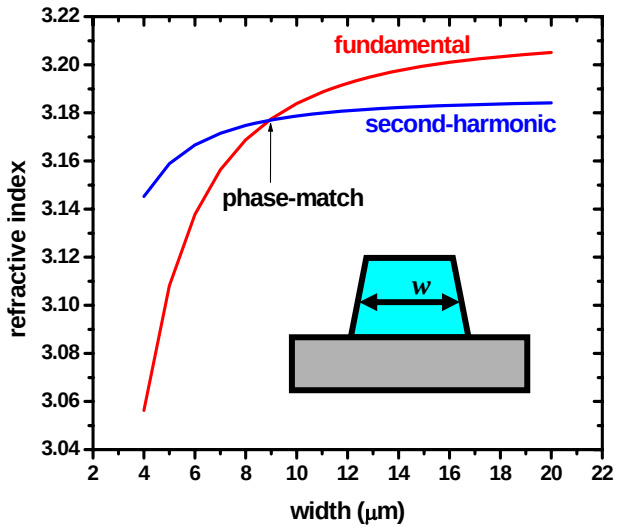

Fig.1.12. Different dispersion relationships of effective refractive indices of TM_0 and TM_2 modes with the width of the waveguide. At the phase matching point, the phase mismatch due to materials is compensated by that of different TM modes.

Another method to achieve phase matching is called quasi-phase-matching [1]. The idea of quasi-phase matching is using periodically poled material, which is a structure with the orientation of one of the crystalline axes periodically inverted as the function of position. Consequently, by periodically inverting the sign of the nonlinear coupling efficient one can compensate non-zero phase mismatch. For more information, please refer to chapter 2.9 of Ref. [1]. M. Belkin *et al.* reported quasi-phase-matching in a SHG QCL by periodically applying bias voltage and no bias voltage along the ridge of the device, in which they periodically modulated the refractive index and the nonlinear susceptibility of SHG process [53]. They observed ten times enhancement of the SHG conversion efficiency by achieving quasi-phase-matching.

2. ROOM TEMPERATURE TERAHERTZ SOURCE BASED ON DIFFERENCE FREQUENCY QUANTUM CASCADE LASERS *

2.1 Introduction

The THz radiation, or called T-ray, is an electromagnetic radiation in the wavelength range of 30 μm to 300 μm. T-rays can penetrate dry optically opaque cover, such as envelop, cloth and suitcase. They can be used to identify or locate objects under cloth or in a suitcase. Moreover, they can be used to distinguish big molecules and to detect explosive powder or drugs, which have unique spectra in the THz range. This makes T-rays extremely valuable in security applications. The low energy of a T-ray photon makes it relatively harmless to human bodies or tissues. Therefore T-rays can also be used for medical imaging. THz radiation is so important that people are eager to have THz devices for various applications, especially at room temperature.

As of 2004, there were only several viable THz sources. They were either huge device systems, such as gyrotron, the backward wave oscillator, the free electron lasers, and synchrotron light source [54], or required cryogenic cooling, such as far-IR QCL [32,44,45,55-58]. Currently many groups and companies are working on increasing the

---

* Part of the data reported in this section is reprinted with permission from "Room Temperature Terahertz Quantum Cascade Laser Source Based on Intracavity Difference Frequency Generation" by M. A. Belkin, F. Capasso, F. Xie, A. Belyanin, M. Fischer, A. Wittmann, and J. Faist, 2008, *Appl. Phys. Lett.* **92**, 201101, Copyright [2008] by American Institute of Physics journals (AIP).

operating temperature of THz QCLs [56-63]. The highest operating temperature is 178 K which still requires cryogenic cooling [57]. The progress has been slow because of fundamental difficulties related to thermal backfilling of the lower laser state, lower injection efficiency and faster depopulation of the upper state as the temperature increases.

An alternative method is frequency mixing or utilizing optical nonlinearities. Some pioneer works include far-IR generation by DFG process in coupled quantum-well structure [59], and THz generation by DFG process in quasi-phase- matched GaP [60], or GaAs [61], with two external pumping lights. This approach offers broad spectral tunability and does work at room temperature, but requires powerful external laser pumps and bulky setup.

Integrating DFG process with quantum cascade lasers is an approach that has been pursued by our group since 2001 [64]. It does not need external optical pump and complicated setup, but can also work at room temperature, since the THz generation mechanism is still the frequency mixing. DFG in the mid-IR range in butt-joined diode lasers has been demonstrated in [72]. With QCL technology the development of integrated DFG sources has been facilitated by the fact that dual wavelength, room temperature high performance QCLs have been already demonstrated [62-63]. THz generation by integrating DFG process with QCL was realized for the first time in 2007 in collaboration between our group and Capasso group in Harvard [51]. Radiation of DFG signal at 65 μm was achieved. The advantage of this approach is no population inversion is required at THz transition, since the latter is extremely difficult to achieve at

room temperature. However, the device only worked at liquid nitrogen temperature [51]. There was still room to improve, and the ultimate purpose was to achieve a room temperature operated THz source. Below we report such a device [65].

2.2 Difference Frequency Generation in a QCL and the Nonlinear Susceptibility

Due to high optical loss of THz radiation in the moderately doped semiconductor materials, and low collecting efficiency of T-rays, in this design, a nonlinear optical medium with giant nonlinear susceptibility is necessary to achieve significant DFG power. The process is described by a nonlinear polarization of the form

$$P(\omega_p - \omega_q) = 2\chi^{(2)} E_p E_q^* , \qquad (2.1)$$

where $\chi^{(2)}$ is the second order nonlinear susceptibility, E_p and E_q are the electric field amplitudes of two pumps.

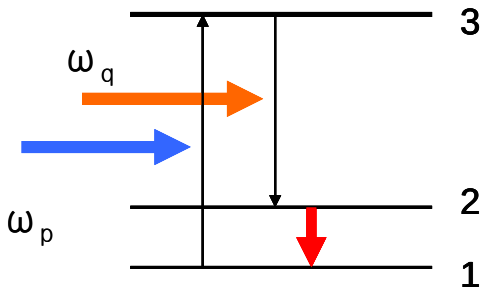

Fig.2.1. A typical three-level system for difference frequency generation process.

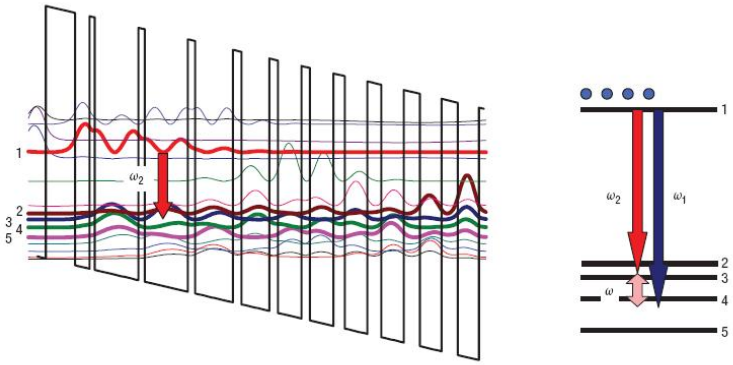

Fig.2.2. The band diagram of the DFG QCL design. A three-level system of energy states of 1, 3 and 4 is shown in the active region. The active region is lasing at frequency ω_2, and is also the active region of DFG process [51].

In order to provide a giant nonlinear susceptibility, the medium must have three proper atomic or electronic energy states, or a three-level system, as shown in Fig.2.1. Similar to Eq. (1.20), the nonlinear susceptibility in the three-level system can be expressed as:

$$\chi^{(2)}(\omega_p-\omega_q,\omega_p,\omega_q)=\frac{\mu_{12}\mu_{23}\mu_{13}}{2\hbar^2}\sum_{\substack{ijk\\ i\neq j\neq k}}^{3}n_i\{\frac{1}{[\omega_{ki}-\omega_p-\omega_q-i\gamma][\omega_{ji}-\omega_p-i\gamma]}$$
$$+\frac{1}{[\omega_{ki}-\omega_p-\omega_q-i\gamma][\omega_{ji}-\omega_q-i\gamma]}+\frac{1}{[\omega_{jk}-\omega_p-\omega_q-i\gamma][\omega_{ki}+\omega_p+i\gamma]}$$
$$+\frac{1}{[\omega_{jk}-\omega_p-\omega_q-i\gamma][\omega_{ki}+\omega_q+i\gamma]}+\frac{1}{[\omega_{ji}+\omega_p+\omega_q+i\gamma][\omega_{ki}+\omega_p+i\gamma]}$$
$$+\frac{1}{[\omega_{ji}+\omega_p+\omega_q+i\gamma][\omega_{ki}+\omega_q+i\gamma]}+\frac{1}{[\omega_{kj}+\omega_p+\omega_q+i\gamma][\omega_{ji}-\omega_p-i\gamma]}$$
$$+\frac{1}{[\omega_{kj}+\omega_p+\omega_q+i\gamma][\omega_{ji}-\omega_q-i\gamma]} \qquad ,(2.2)$$

where μ_{ij} is the dipole moment between level i and j, n_i is the electron population at level i, γ is the dephasing rate or the homogeneous broadening and is considered as a constant value, ω_{ij} is the energy difference between level i and j, ω_p and ω_q are frequencies of two pump radiations.

One smart way to integrate DFG process with a QCL is to design an active region of a QCL with a three-level system mentioned above. Therefore the laser active region itself serves as nonlinear medium at the same time, so that no extra nonlinear section is needed. This design is achieved in Ref. [51], and the band-diagram of one period of the QCL is shown in Fig.2.2.

In this case, when the quantum-well structure is under applied bias of operating condition, electrons are injected mainly into the upper laser level, the level 1 in Fig. 2.2, or the level 3 in Fig. 2.1. The second order susceptibility (2.2) then can be simplified as:

$$\chi^{(2)}(\omega_p-\omega_q,\omega_p,\omega_q)\approx\frac{n_3\mu_{12}\mu_{23}\mu_{13}}{2\hbar^2}\cdot \left[\frac{1}{[\omega_{21}-(\omega_p-\omega_q)-i\gamma][-\omega_{31}+\omega_p+i\gamma]}+\frac{1}{[-\omega_{21}+(\omega_p-\omega_q)-i\gamma][-\omega_{32}+\omega_q+i\gamma]}\right] . \quad (2.3)$$

By plugging Eq. (2.3) into Eq. (2.1) and combining them with wave equations Eq. (1.5), we can calculate the light intensity of the DFG signal as

$$I_3=\frac{8\pi^3\left|\chi^{(2)}\right|^2\omega_3^4 I_1 I_2 n_3}{k_3^2 c^5 n_1 n_2}\left|\frac{e^{i\Delta kL}-1}{\Delta k}\right|^2 , \quad (2.4)$$

where the intensity is given by the magnitude of the time-averaged Poynting vector, and can be expressed as

$$I_i = \frac{n_i c}{2\pi}\left|E_i\right|^2 , \qquad (2.5)$$

where n_i is the refractive index, c is the speed of light, and E_i is the electric field amplitude of a laser mode with i = 1 or 2.

In the actual device, the light is propagating as a TM waveguide mode, as mentioned before. In order to calculate the power of DFG signal, we must consider the transverse intensity distribution, or the mode profile. The magnetic field amplitude of the mode at frequency ω in a waveguide is described as:

$$H(x,y,z,t) = H_\omega(x,z) \times h(y) \times e^{i(\omega t - ky)} , \qquad (2.6)$$

where y is the direction of wave propagating, z is the direction of growth, *h(y)* is a slowly varying amplitude that accounts for the increase of the mode intensity as it propagates in the waveguide. Similar to Eq. (1.5), the wave equation for the magnetic field is given as

$$2ik\frac{\partial h(y)}{\partial y} \times H_\omega(x,z)e^{i(\omega t - ky)} = i4\pi\omega\frac{\partial P^{(2)}(x,y,z,t)}{\partial y} , \qquad (2.7)$$

where $H_\omega(x,z)\times e^{i(\omega t-ky)}$ is the solution of the wave equation for the passive waveguide. Using the orthogonality of waveguide modes of different order, we obtain *h(y)* as

$$\frac{\partial h(y)}{\partial y} = \frac{2\pi\omega}{k}\frac{\int H_\omega(x,z)\frac{\partial P^{(2)}(x,y,z,t)}{\partial y}e^{-i(\omega t-ky)}dxdz}{\int \left(H_\omega(x,z)\right)^2 dxdz} . \qquad (2.8)$$

Then we plugged Eq. (2.1) into Eq. (2.8) and used the relationship between the electric and magnetic field in a TM-polarized mode:

$$E_{\omega_i}^{z}(x,z)=\frac{n_{eff}^{\omega_i}}{\varepsilon_{\omega i}(x,z)}H_{\omega_i}(x,z), \tag{2.9}$$

where $n_{eff}^{\omega_i}$ and k_i are the effective refractive index and the wave vector of the mode at frequency ω_i. Inserting Eq. (2.9) and (2.1) into (2.8), we have

$$h(y)\approx -2\pi\omega\frac{e^{i\Delta ky}}{i\Delta k}\times \frac{\int H_{\omega}(x,z)\frac{n_{eff}^{\omega_1}}{\varepsilon_{\omega 1}(x,z)}H_{\omega_1}(x,z)\frac{n_{eff}^{\omega_2}}{\varepsilon_{\omega 2}(x,z)}H_{\omega_2}(x,z)\chi^{(2)}(x,z)dxdz}{\int (H_{\omega}(x,z))^2 dxdz}, \tag{2.10}$$

where we utilized the fact that that $\omega=\omega_1-\omega_2$ and assumed that $(k_1-k_2)/k\approx 1$. As mentioned above, the power of the DFG signal is the time average of Poynting vector, defined as

$$W(\omega)\approx\left\langle\int E(x,z,t)H(x,z,t)dxdz\right\rangle = \frac{cn_{eff}^{\omega}}{2\pi}\int\frac{(H_{\omega}(x,z))^2}{\varepsilon_{\omega}(x,z)}dxdz\times(h(y))^2 . \tag{2.11}$$

By plugging Eq. (2.9) and (2.10) into (2.11), we obtain the power of DFG emission after some simplification,

$$W\approx\frac{8\pi^3 n_{eff}^{\omega}n_{eff}^{\omega_1}n_{eff}^{\omega_2}\omega^2}{c}\times W_1W_2\times l_{coh}^2\times \left[\int\frac{(H_{\omega}(x,z))^2}{\varepsilon_{\omega}(x,z)}dxdz\left|\int H_{\omega}(x,z)\frac{H_{\omega_1}(x,z)}{\varepsilon_{\omega_1}(x,z)}\frac{H_{\omega_2}(x,z)}{\varepsilon_{\omega_2}(x,z)}\chi^{(2)}(x,z)dxdz\right|^2\right]/ \left[\left(\int(H_{\omega}(x,z))^2dxdz\right)^2\int\frac{(H_{\omega_1}(x,z))^2}{\varepsilon_{\omega_1}(x,z)}dxdz\int\frac{(H_{\omega_2}(x,z))^2}{\varepsilon_{\omega_2}(x,z)}dxdz\right], \tag{2.12}$$

where the coherence length satisfies:

$$l_{coh} = \left| \frac{e^{i\Delta kL} - 1}{\Delta k} \right|. \tag{2.13}$$

Assuming $\varepsilon(x,z) \approx (n_{eff})^2$, we can further simplify Eq. (2.12) as:

$$W \approx \frac{8\pi^3 \omega^2}{c n_{eff}^{\omega} n_{eff}^{\omega_1} n_{eff}^{\omega_2}} \times \frac{\left|\chi^{(2)}\right|^2}{\Gamma_{eff}} W_1 W_2 \times l_{coh}^2 , \tag{2.14}$$

where the effective confinement Γ_{eff} factor is given as

$$\Gamma_{eff} = \left|\chi^{(2)}\right|^2 \frac{\int (H_{\omega}(x,z))^2 dxdz \int (H_{\omega_1}(x,z))^2 dxdz \int (H_{\omega_2}(x,z))^2 dxdz}{\left| \int H_{\omega}(x,z) H_{\omega_1}(x,z) H_{\omega_2}(x,z) \chi^{(2)}(x,z) dxdz \right|^2}. \tag{2.15}$$

It can be calculated once we know the waveguide modes profile for each frequency, as shown in Fig. 2.3.

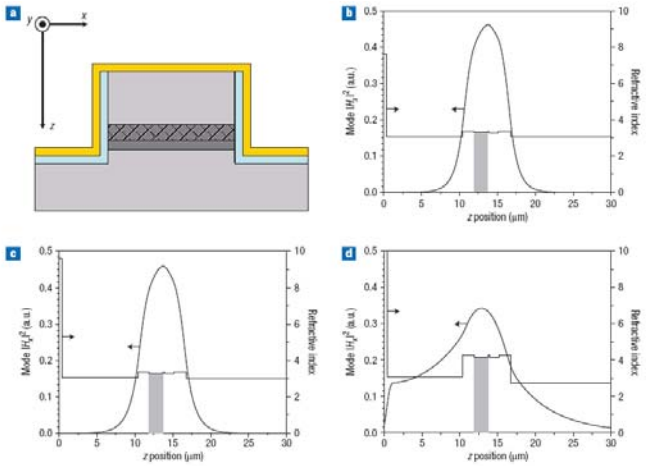

Fig. 2.3. The waveguide modes for fundamental frequencies and DFG frequency. (a) Two QC laser active cores are stacked together inside a waveguide; (b) the profiles of mode for frequency ω_1 and refractive index; (c) the profiles of mode for frequency ω_2 and refractive index; (d) the profiles of mode for DFG frequency ω_3 and refractive index, the gray area is the active region with nonzero nonlinear susceptibility [51].

2.3 Laser Gain Spectra and Two-Wavelength Operation

As we showed in Fig. 2.3, the design of a DFG QCL requires two QCL active cores stacked in one waveguide cavity, in order to provide two pump lights at two different frequencies. However the two frequencies are required to be very close to each other at frequency spectrum, because we want the difference of them at THz range, at which the photon energy is only about 10~20 meV. It is a challenge to ensure lasing at two close frequencies in the cavity at the same time.

As mentioned before, we would have a three level system, in which transition 3-2 is the lasing transition, as shown in Fig. 2.4.

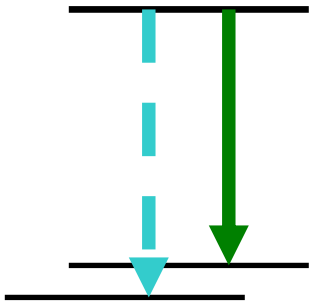

Fig. 2.4. Three level system with one lasing transition 3-2.

We obtain the laser gain by analyzing the wave equation (2.16) in a laser system [64],

$$\frac{d\Omega}{dt}+\kappa\Omega=\frac{2\pi\omega N d_{32}^2}{\hbar n^2}\frac{\rho_3-\rho_2}{\gamma+i\Delta}\Omega, \tag{2.16}$$

where Ω is the Rabi frequency of the laser mode, κ is optical loss in the medium, n is the refractive index, N is total population of carrier, d_{32} is the dipole moment between energy level 3-2, Δ is frequency detuning, ρ_i is the population rate at energy level i. We have the optical gain at the lasing frequency proportional to the square of the dipole moment, as

$$gain \propto \frac{2\pi\omega N d_{32}^2(\rho_3 - \rho_2)}{\hbar n^2} \mathrm{Re}(\frac{1}{\gamma + i\Delta}) . \tag{2.17}$$

Therefore we obtain the expression of gain spectra. In order to have two frequencies lasing simultaneously, we need a laser spectrum with two peaks which are almost equally strong, instead of having one peak much stronger than the other, or two merged peaks, as shown in Fig. 2.5. Otherwise, there would be only one lasing frequency, and therefore no DFG process.

2.4 A New Design of THz DFG Quantum Cascade Laser with Doubled Resonant Nonlinear Active Cores

In previous sections, we introduced the principles for design of a DFG QCL for THz emission. Here I will show a new design of a DFG QCL at λ=16 μm and 12.1 μm, in which the nonlinear susceptibility has been improved several times as compared to the previous device N970A [65].

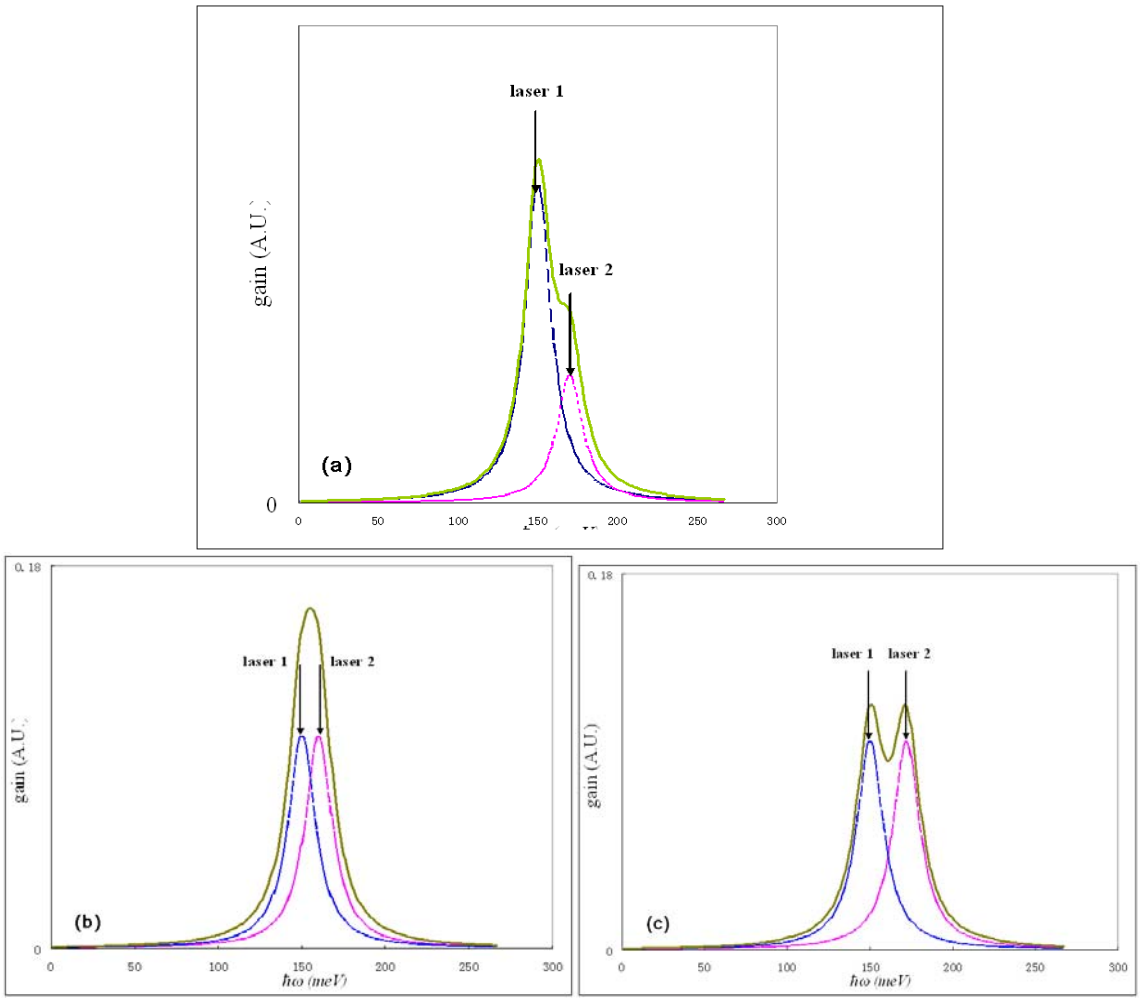

Fig. 2.5. The scratches of gain spectra indicate two wavelengths operation. (a) The total gain spectrum, the solid line, when the gain of one laser frequency is much larger that of the other. (b) The situation when two laser frequencies are too close to each other. (c) The situation we are looking for. Two peaks are equally strong in the total gain spectrum,

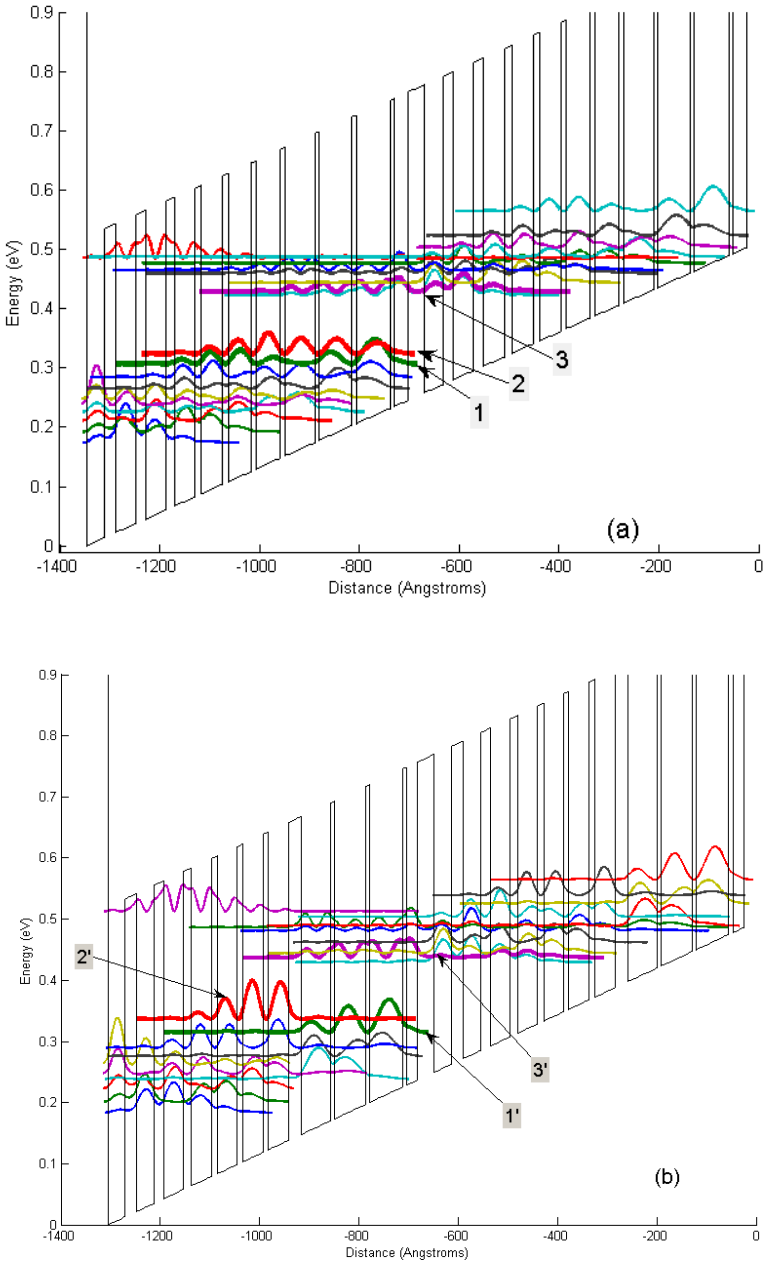

Fig. 2.6. The band diagrams of two active layers, under a bias of 30kV/cm. (a) The lasing transition of laser ‘a’ is 3-2, of which transition energy is about 80 meV (lasing at 16 μm). (b) The lasing transition of laser ‘b’ is 3-1, with transition energy 103 meV (12.1 μm).

The band diagrams of the two QCL active layers are shown in Fig. 2.6. The thickness sequences of quantum wells and barriers in laser 'a' is 46/12/44/14/44/17/42/20/41/22/40/33/32/5/65/6/66/7/63/8/58/10 (starting from well), and that of laser 'b' is 42/12/37/15/42/17/41/20/38/22/36/37/26/5/66/6/64/7/63/10/59/10. As shown in the band diagram, laser 'a' is designed working wavelength of 16 μm, with the three-level system, energy states 1-2-3, in the active region of laser. The dipole moments of transition 3-2, 3-1 and 2-1 are 28.4 Å, 15.5 Å and 112.4 Å respectively. The transition energy of 2-1 is about 16 meV. The laser 'b' has working wavelength at 12.1 μm, containing the other three-level system 3'-2'-1'. The dipole moments of transition 3'-2', 3'-1', and 2'-1' are 22.5 Å, 31.3 Å, and 58.9 Å respectively, and the transition energy of 2'-1' is about 24 meV. The frequency difference of two lasers is about 23 meV, namely a DFG signal of 54 μm, which is about 5 THz, is expected to be generated.

The gain spectrum has been optimized to ensure two wavelengths operation, as shown in Fig. 2.7.

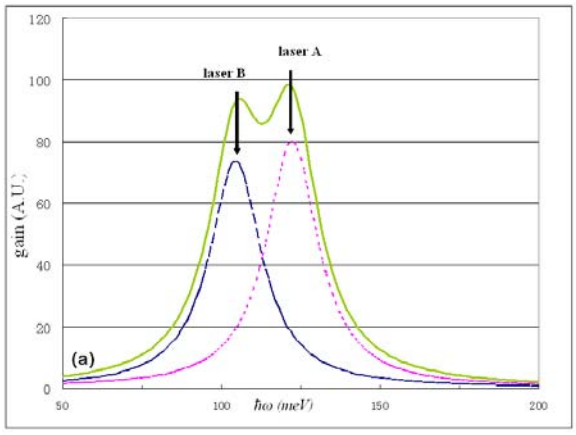

Fig. 2.7. The gain spectrum of new DFG QCL design has two peaks.

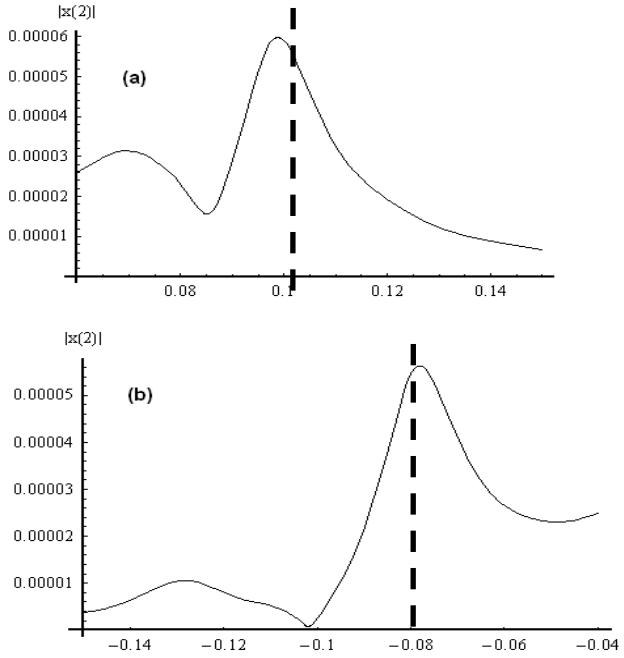

Fig. 2.8. The profiles of absolute values of nonlinear susceptibilities of (a) laser 'a' and (b) laser 'b'. The dashed lines indicate the frequencies of the other working laser.

The nonlinear susceptibilities of both active cores have also been optimized. Since we have all the parameters, such as dipole moments and energies of transitions, we can insert those numbers from above into the Eq. (2.3) to calculate nonlinear susceptibilities for both laser cores. In this design, the combination of two lasing wavelengths enables the maximum nonlinear susceptibilities at both laser sections, as shown in Fig. 2.8. As a result, the absolute values of nonlinear susceptibilities reach 5.4×10^{-5} esu and 5.2×10^{-5} esu. They are about 1.5 times larger than in the previous device N970A [65], which only had one section with nonlinear susceptibility. Therefore,

about 5 times higher DFG power will be expected compared with N970A, if there is similar power of two pump lasers.

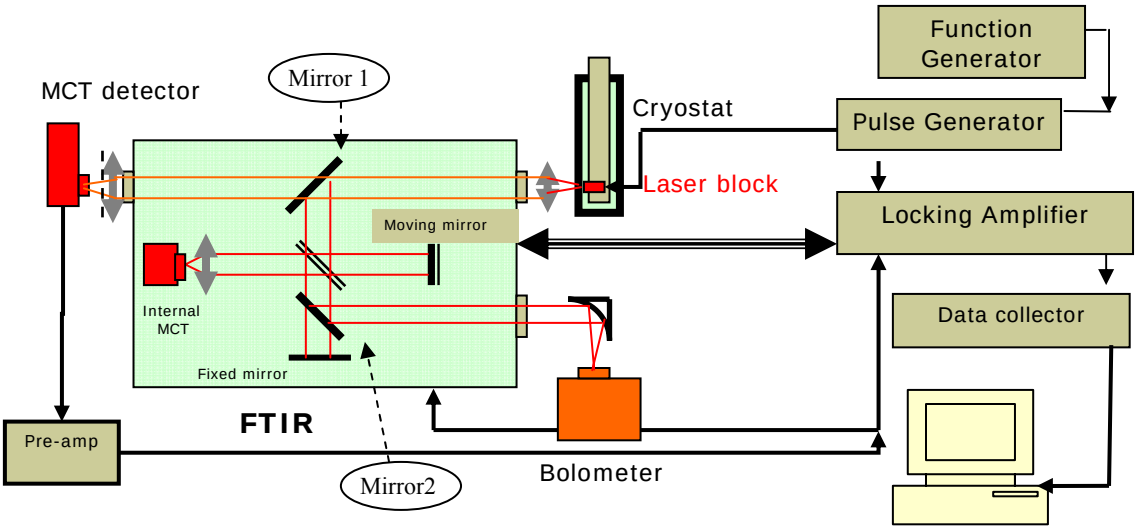

Fig. 2.9. The experimental setup for the measurement of a DFG QCL. A FTIR was used to measure spectra of fundamental pump lasers and the DFG THz signal. When the 'mirror 1' is removed, the system measures the power of fundamental lasers. When the 'mirror 2' is inserted, the system measures the spectrum and power of THz signal by using a liquid helium cooled bolometer.

2.5 The Experimental Results of DFG QCL Device N970A

The new design of DFG QCL discussed in previous section was sent to grow, when I did summer research in Dr. Federico Capasso's group in Harvard University in summer 2007. We didn't wait for the arrival of the new wafer. Instead, we processed and measured the DFG QCL device N970 based on previous design; and achieved

significant results. THz emission at 60 μm was observed at temperature up to 250K before I left the group, and the THz power reached about 1 μW at 80K.

The experiment setup is shown in Fig. 2.9. The laser block was mounted in a cryostat, and cooled with liquid Nitrogen. It can be heated with a temperature controller insider the cryostat. Lasers were driven by a current pulse generator with both 500Hz and 80KHz repetition rates and 1% duty cycle. A Fourier Transform Infrared spectroscopy (FTIR) was used to measure laser spectra. An external MCT photo detector was used to measure mid-IR laser power. We applied a filter in front of the external MCT detector to separate two mid-IR wavelengths. The MCT detector is not suitable for measurement of THz signal. We employed a liquid Helium cooled bolometer, which is very sensitive to heat radiation, to measure both spectra and power of THz signal. A filter which blocked everything shorter than 40 μm was employed before the bolometer. All signals were sent to the lock-in amplifier, and then were sent to the computer.

Here I want to show some experimental results. First, the device N970A successfully lased at two wavelengths, 9 μm and 10.5 μm, simultaneously at different temperatures, as shown in Fig. 2.10. The total peak power of mid-IR emission was over 1.3 W at 80K, and over 0.1 W at 300K, as shown in Fig. 2.11. The strong mid-IR power makes it promising for DFG process, because the DFG power is proportional to the product of power of two mid-IR lasers.

The most important thing is that we observed THz radiation at 55 μm, which survived up to 250K. The spectra are shown in Fig. 2. 12. This was the first THz

semiconductor device at thermal electrically (TE) cooled temperature, and was the highest operation temperature for THz semiconductor lasers on record!

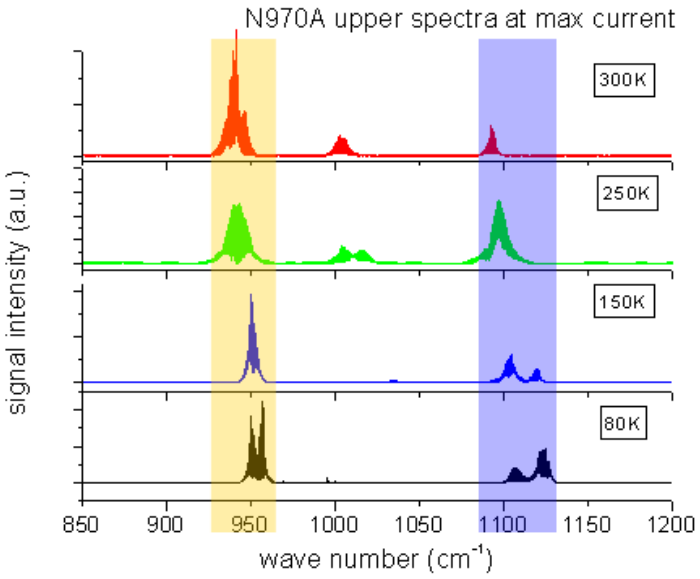

Fig. 2.10. Mid-IR emission spectra at 80K, 150K, 250K and 300K. Emissions at two wavelengths were realized at various temperatures, although there was a third wavelength at higher temperature.

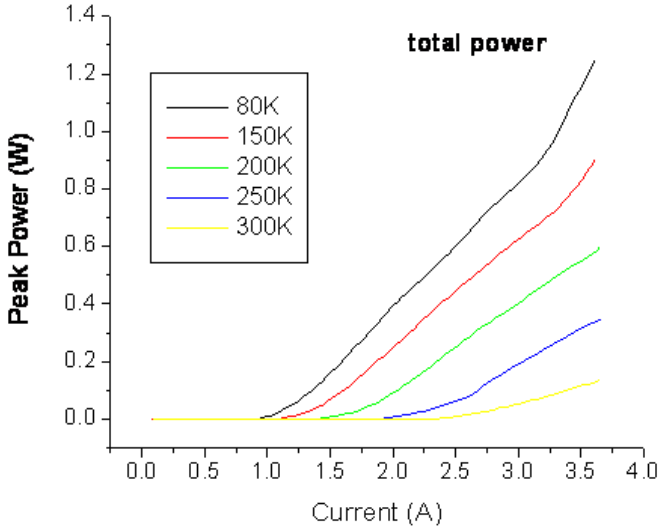

Fig. 2. 11. The total mid-IR peak power of the device at various temperatures versus the pump current.

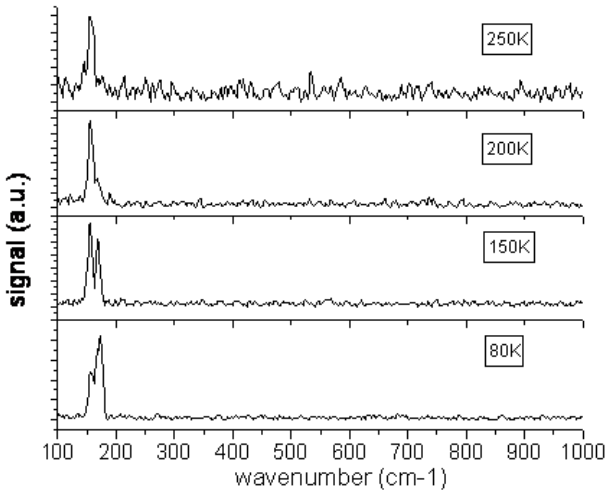

Fig. 2.12. THz emission of the device N970A at various temperatures from 80K to 250K.

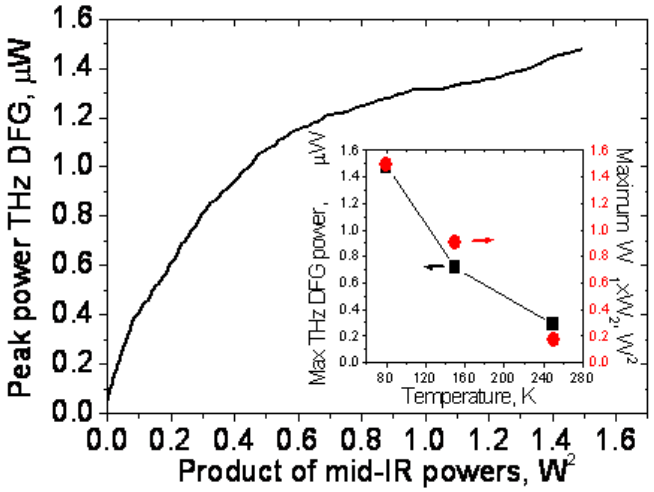

Fig. 2.13. The peak power of THz emission versus the product of two mid-IR powers at 80K, showing the maximum peak power reached 1.5 μW. The inserted picture is the THz power and product of mid-IR power at different temperatures, showing the power conversion efficiency has no significant degrading at higher temperature.

The power of THz emission of device N970A is showed in Fig. 2.13. It reached 1.5 μW at temperature 80K. Although at higher temperature, the power of THz emission dropped, but also did the power of mid-IR. From the temperature dependence of both THz power and the product of Mid-IR power, we found the power conversion efficiency, which was about $1\mu W/W^2$, was kept the almost the same. It means the DFG process was barely affected by temperature. Therefore, if we can provide more power of mid-IR laser at room temperature, we can easily achieve THz emission at room temperature.

I also did simulation for the DFG process to prove the THz emission was indeed due to the DFG process in the device. We found some characteristic peaks in the THz spectra. To understand these peaks, I took mid-IR spectra data and plugged them into Eq.

(2.14), to simulate the THz signal due to DFG process. The results matched the experimental data very well for data at both 80K and 150K, as shown in Fig. 2.14. The results also matched at higher temperatures. It is a solid proof that the THz we observed is indeed due to the DFG process by two mid-IR laser wavelengths in the device N970A.

Overall the THz DFG QCL device N970A showed very impressive and promising results. It has strong mid-IR power at two wavelengths, which provide internal pump sources for the DFG process. It has a strong nonlinearity in the cavity, which caused THz emission at 55 μm. The maximum temperature for the THz emission reached 250K, which was the highest temperature on record for THz semiconductor lasers, and the peak power of THz emission reached 1.5 μW at 80K.

For updating, after I left Capasso's group in 2007, Mikhail Belkin attached a silicon hemisphere lens at the end of device N970A, to further improve the collecting efficiency of THz emission. With this modification, the peak power of THz emission observed reached 7 μW at 80K, and THz emission at room temperature (300K) was observed [65]!

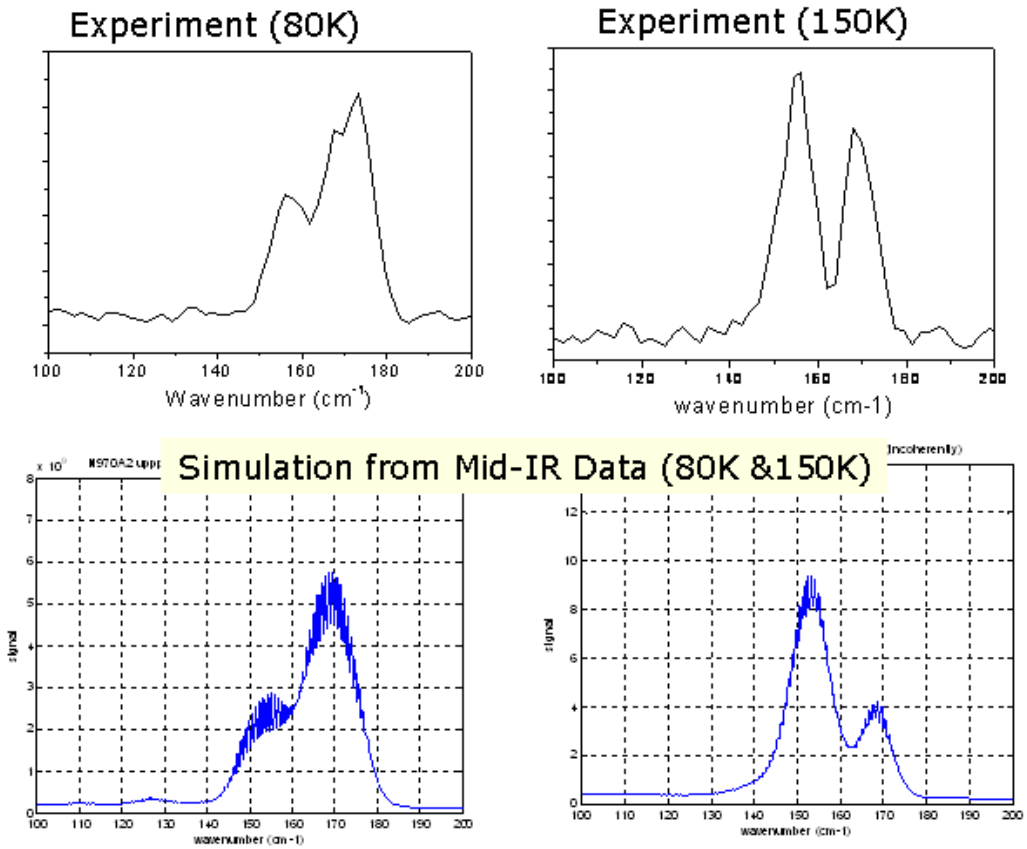

Fig. 2.14. The spectra simulation matched the experimental results. The THz spectra showed specific peaks at different temperatures (up). The simulation results at the bottom matched them pretty well.

3. SECOND HARMONIC GENERATION QUANTUM CASCADE LASER AND THE CHARACTERIZATION OF THE OPTICAL NONLINEARITY *

3.1 Introduction

The concept of 'quantum engineering' in quantum-well structures greatly impacts opto-electronics. Quantum cascade laser is one of the results of the 'quantum engineering' of intersubband optical transitions [22]. Based on the same principle, a strong nonlinear oscillator can be also designed in semiconductor quantum-well structures [9-12]. Moreover, optical nonlinearities can be monolithically integrated with a pump light source such as a QCL. It is a good approach for efficient coupling and avoiding resonant absorption of fundamental pump light. One example is the difference frequency generation QCL discussed in previous section. The second harmonic generation QCL is another one.

The QCL integrated with a SHG process was demonstrated in 2003. In Ref. 48, Nina Owschimikow *et al.* monolithically integrated two-stack two wavelength QC laser and coupled quantum-well structures with strong susceptibilities for both sum frequency and second harmonic generation. They observed two SHG signals at 3.6 μm and 4.8 μm

---

* Part of the data reported in this section is reprinted with permission from "Second-Harmonic Generation in Quantum Cascade Lasers with Electric Field and Current Dependent Nonlinear Susceptibility" by D. Qu, F. Xie, G. Shu, S. Momen, and E. Narimanov, *et al.* 2007, *Appl. Phys. Lett.* **90**, 031105, Copyright [2007] by American Institute of Physics journals (AIP).

and the SFG signal at 4.1 μm. Clare Gmachl *et al.* later optimized the SHG QCL and achieved second order susceptibility of 4.7×10^{-5} esu [49], and found a new approach of integration in which the SHG three-level system was embedded within the quantum wells of the active region of a QCL, instead of adding additional quantum-well layers, as mentioned in the section 1.5.

After that a few other groups also reported SHG QCLs [66-67]. In most of the SHG QCL devices, the nonlinear power conversion efficiencies of SHG were found nearly constant within a factor of 2 regarding pump current. In 2006, we found strong increase of nonlinear power conversion in the SHG QCL device D3056 [68]. The understanding of this interesting result offers the possibility to design structures with the maximum nonlinear light conversion efficiency at the highest linear light power. Therefore, the performance of SHG in QCLs and in other nonlinear QC lasers will be improved.

3.2. The Design of SHG QCL Device D3056 and the Second Order Susceptibility

Device D3056 was also designed with the monolithic integration approach of SHG process within a QCL the band-diagram of which is shown in Fig. 3.1. The laser transition 3-2 was designed at 142 meV (about 8.7 μm). An energy state 4 was designed over the laser upper state 3, with energy separation about 122 meV, which is a little lower than the laser transition energy. Therefore energy states 2, 3 and 4 form a three-

level system for second harmonic generation at 142 meV. The SHG signal is expected at 284 meV, which is about 4.3 μm. Most of free electrons in the quantum-well system assemble at upper laser level, state 2, under lasing condition. One would suspect strong absorption of laser frequency from level 3 to level 4. However, strong absorption from state 3 to 4 is avoided due to about 20 meV detuning of transition 3-4 from the laser frequency.

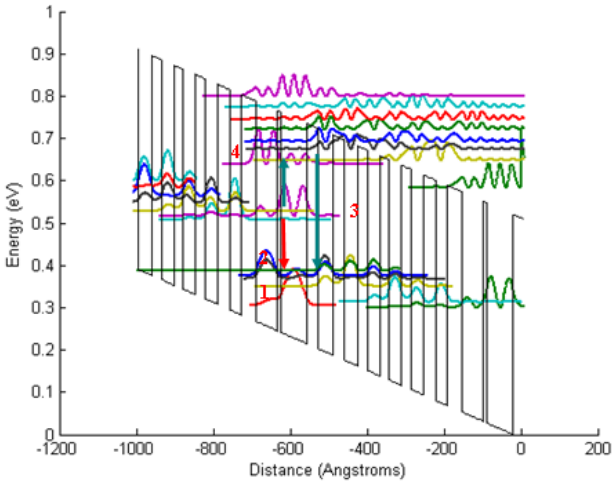

Fig. 3.1. The band diagram with modulus squared of essential electron wave functions. The structure is under electrical bias of 42 kV/cm. The barrier (InAlAs, bold) and well (InGaAs) thicknesses in nanometers from right to left starting from the first active region well are as follows (in Angstrom): 68/**10**/55/**40**/29/**32**/30/**28**/31/**24**/31/ **27**/35/**30**/38/**28**. Underlined layers indicate a doping density of 2.0×10^{17} cm^{-3}.

The second order susceptibility can be obtained by adjusting Eq. (1.20), and it can be expressed as;

$$\chi^{(2)} = \frac{e^3 N_e}{2\hbar^2}\left[\frac{d_{23}d_{34}d_{24}}{\Delta_{42}-i\gamma}\left(\frac{n_2-n_3}{\Delta_{23}-i\gamma}+\frac{n_4-n_3}{\Delta_{43}-i\gamma}\right)\right], \qquad (3.1)$$

where N_e is the total electron density, $\Delta_{ij}=(\omega_i-\omega_j)-\omega_p$ is the detuning of transition from the pump frequency (or double pump frequency for transition 4-2), γ is the common homogeneous broadening factor about 10 meV, d_{ij} is the dipole moment of transition i-j, and n_i is the electron population of energy state i.

The analysis of nonlinear optical power in the SHG process is similar to that of the DFG process in previous section. Considering waveguide loss and mirror loss at facets of the device, we can obtain the optical power of SHG signal as

$$W_2 \approx \frac{32\pi^3\omega_2^2\left|\chi^{(2)}\right|^2\left[1+e^{-2\alpha_2 L}-2e^{-\alpha_2 L}\cos(\Delta kL)\right](1-R_2)}{n_1^2 n_2 c\Gamma_{eff}\left(\Delta k^2+\alpha_2^2\right)(1-R_1)^2}W_1^2, \tag{3.2}$$

with

$$\Gamma_{eff}=\left|\chi^{(2)}\right|^2\frac{\int\left(H_{\omega_2}(x,z)\right)^2 dxdz\left(\int\left(H_{\omega_1}(x,z)\right)^2 dxdz\right)^2}{\left|\int H_{\omega_2}(x,z)H_{\omega_1}{}^2(x,z)\chi^{(2)}(x,z)dxdz\right|^2}, \tag{3.3}$$

where $\omega_2=2\omega_1$ is the SH frequency, α_2 is the waveguide loss of SHG signal, R_1 is the facet reflectivity of the fundamental signal, R_2 is that of SHG signal, Δk is phase mismatch of SHG, L is the length of a laser cavity, and Γ_{eff} is the effective confinement factor, which is similar to Eq. (2.15).

3.3. The Experimental Setup and Results for Device D3056

The experimental setup is also similar to Fig. 2.9. The difference is that we employed liquid nitrogen cooled external InSb photo detector, which is much more

sensitive in the near-IR range, instead of a bolometer to measure the SHG signal. A simple filter of a glass slide was used to block the fundamental optical power in front of the InSb detector.

The device was characterized at 80K, and was operated with pulsed current pump. The repetition rate was 80 kHz, with 12.5 ns pulse width. The device lased at 8.4 μm, and the spectra were shown in Fig. 3.2. The SHG signal at 4.2 μm was observed, as shown in Fig. 3.3. From the spectra at various currents, we found the frequency of the SHG signal is stable regarding the injection current, although the frequency of fundamental signal has a slight shifting.

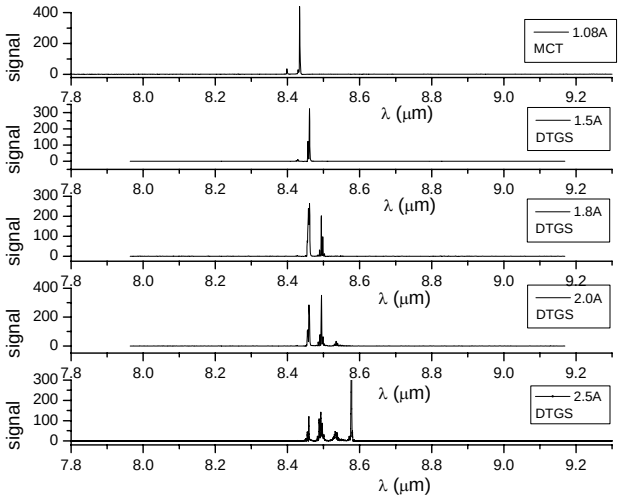

Fig. 3.2. The spectra of fundamental pump light. The spectra were taken at various injection current, from 1.0 A to 2.5 A (from top to bottom). The laser was working at about 8.5 μm.

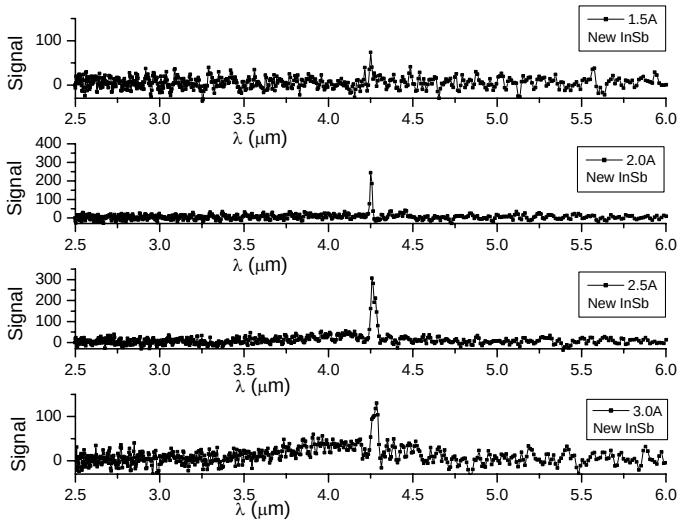

Fig. 3.3. The spectra of SHG signal at various injection current. They were taken from 1.5 A to 3.0 A (from top to bottom). The wavelength of SHG signal is about 4.25 μm, and the frequency of SHG signal was very stable.

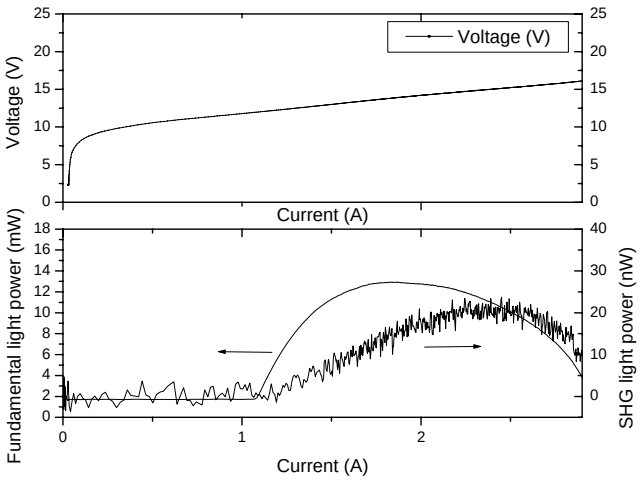

Fig. 3.4. The L-I-V curve of device D3056. The upper one is the voltage vs current characteristic. The lower one is the output power measured by room temperature HgCdTe (MCT) detector and liquid nitrogen cooled InSb detector for mid-IR laser power and SHG power respectively.

The L-I-V curves of the device D3056 is shown in Fig. 3.4. The lasing threshold current was found at 1.05 A, with bias voltage about 12 V. The device has a ridge about 16 μm wide, and is 2.3 mm long. Therefore the threshold current density is about 3 kA/cm^2. The maximum mid-IR pump power reached 12 mW per facet. The SHG signal was observed almost immediately after the pump laser was turned on. Due to non phase-matched design, the SHG peak power only reached 22 nW, as shown in Fig. 3.4.

Interestingly, the SHG power did not drop down when the fundamental power started decreasing, although the SHG power should be proportional to the square of the fundamental power. It means the nonlinear power conversion efficiency increased actually with increasing of injection current density, even after the fundamental power rolled over. We plot the nonlinear power conversion efficiency η, which is described by (3.4), versus the laser injected current in Fig. 3.5. We observed a significant increase of the nonlinear power conversion efficiency with current.

$$\eta = W(2\omega)/W^2(\omega) \ . \qquad (3.4)$$

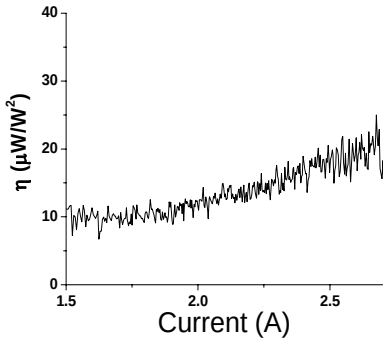

Fig. 3.5. The nonlinear power conversion efficiency vs the pump current. We observed the increasing of the conversion efficiency with the pump current.

Plugging Eq. (3.2) into Eq. (3.4), we can easily obtain the expression of the conversion efficiency as

$$\eta \approx \frac{32\pi^3\omega_2^2\left[1+e^{-2\alpha_2 L}-2e^{-\alpha_2 L}\cos(\Delta kL)\right](1-R_2)}{n_1^2 n_2 c\Gamma_{eff}\left(\Delta k^2+\alpha_2^2\right)(1-R_1)^2}\left|\chi^{(2)}\right|^2 . \tag{3.5}$$

Equation (3.5) indicates that the conversion efficiency η could depend on many parameters, such as ω_2, n_1, n_2, waveguide loss α, mirror reflectivitiesR_1 and R_2, or the second order susceptibility $\chi^{(2)}$. In Eq. (3.5), L is a fixed value, while n_1, n_2, α_2, Δk, R_1, and R_2 are all only depend on fundamental frequency ω_1 or SHG frequency ω_2, or both. However, we barely observe pump current dependence of either the SHG frequency or the fundamental frequency from the spectra of Fig. 3.2 and 3.3. It means that all the parameters can not be the source terms of pump current dependence of the power conversion efficiency, namely only the second order susceptibility could cause the pump current dependency.

There are different mechanisms causing the increasing of the second order susceptibility of SHG process in the device D3056. From Eq. (3.1), one could expect the change of dipole moments, population densities at different states, or detuning factors of different transitions, might cause the change of $\chi^{(2)}$ with current. More details will be discussed in following sub-section.

3.4. The Analysis of the Nonlinear Susceptibility of SHG in Device 3056

As mentioned above, the enhancement of the nonlinear power conversion efficiency with current was observed in device D3056. Increasing of the nonlinear susceptibility with current could be the reason. Understanding the mechanism of the enhancement would enable people to optimize optical nonlinearities, such as SHG, in QCLs, and to achieve the best performance.

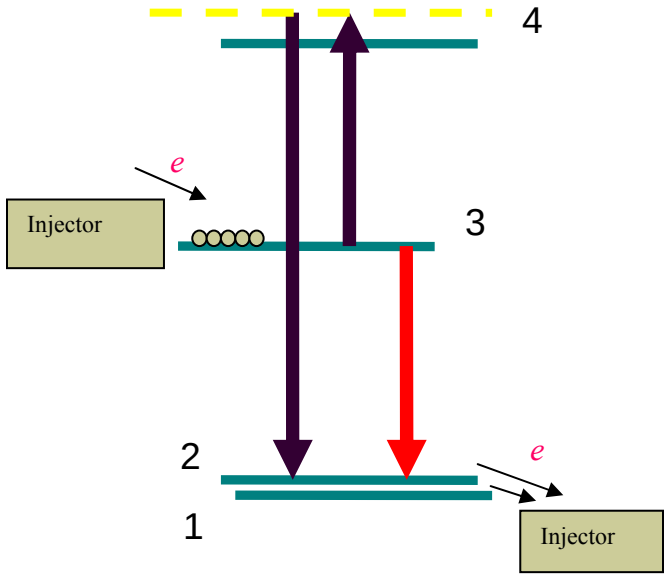

Fig. 3.6. The schematic of electron energy states in laser active region. Transition 3-2 is the laser transition. Electrons are injected from injector to upper laser state 3, and are depleted from lower laser state 2 to injector. Most electrons are accumulated on state 3. States 2-3-4 and 1-3-4 are two sets of resonant three-level system for the SHG process.

Here we give two interpretations for the enhancement of the nonlinear susceptibility with the pump current. First, the nonlinear susceptibility increased due to

the changed populations at the upper laser level and the lower laser level with the current. Second, when the pump current was increased, so did the electrical bias. The change of the bias resulted in the modified band alignment, dipole moments of transitions, and detuning factors in the device. In the first interpretation, the applied electrical bias was assumed unchanged. In the second one, the population rate at each state was assumed changed. Both mechanisms would result in the increasing of the nonlinear susceptibility with the pump current.

The first mechanism can be interpreted within coupled density matrix equations. A simplified sketch of energy state diagram is shown in Fig. 3.6. In the device, at each period of active region, electrons are injected from the previous injector state to upper lasing state 3, and are depleted from lower lasing state 2 to the next injector very fast by resonant longitudinal optical (LO) phonon scattering. Moreover, the life time of state 3 is much larger than that of state 2 and 1. Therefore most of electrons in the active region are accumulated on state 3. When the optical gain, which is described as Eq. (2.17) and is proportional to the population inversion, becomes larger than the loss in the waveguide, the laser starts lasing. Under lasing condition, electrons are stimulated to lower lasing state 2, and emit photons [69]. The coupled density matrix equations for states 1, 2, 3, and Rabi frequency Ω are described by [64],

$$\frac{d\Omega}{dt} + \kappa\Omega = ig\sigma_{32}\,, \tag{3.6}$$

$$\frac{d\sigma_{32}}{dt} + \Gamma_{32}\sigma_{32} = i\Omega(n_3 - n_2)\,, \tag{3.7}$$

$$\frac{d\sigma_{43}}{dt} + \Gamma_{43}\sigma_{43} = i\Omega(n_4 - n_3)\,, \tag{3.8}$$

$$\frac{\partial n_1}{\partial t} = r_{31}n_3 + r_{21}n_2 + r_{43}n_4 - r_{12}n_1 - r_{1i}n_1 , \tag{3.9}$$

$$\frac{\partial n_2}{\partial t} = r_{32}n_3 + r_{12}n_1 - r_{21}n_2 - r_{2i}n_2 + r_{43}n_4 - 2\,\mathrm{Im}\left[\sigma_{32}\Omega^*\right], \tag{3.10}$$

$$\frac{\partial n_3}{\partial t} = j - (r_{32} + r_{31} + r_{3i})n_3 + r_{43}n_4 + 2\,\mathrm{Im}\left[\sigma_{32}\Omega^*\right], \tag{3.11}$$

$$\frac{\partial n_4}{\partial t} = -r_{42}n_4 - r_{41}n_4 - r_{43}n_4 - r_{4i}n_4 + 2\,\mathrm{Im}\left[\sigma_{43}\Omega^*\right], \tag{3.12}$$

$$\Gamma_{ij} = \Delta_{ij} - i\gamma_{ij} , \tag{3.13}$$

$$g = \frac{2\pi\omega N d_{32}\Sigma}{\hbar n_{eff}^{\ 2}} , \tag{3.14}$$

where the Rabi frequency $\Omega = d_{32}\varepsilon/\hbar$, ε is the amplitude of the electric field of the laser mode, σ_{ij} is the off diagonal element of the density matrix, j is the current density, n_i is the population at ith state, r_{mn} is the relaxation rate from state m to n, r_{mi} is the relaxation rate from state m to injector, Δ_{ij} is the detuning of the transition i-j from corresponding optical field, γ_{ij} is the spectrum broadening factor, which is usually replaced by common broadening 10 meV, g is the optical gain, κ is waveguide loss, n_{eff} is the effective refractive index of the waveguide mode, N is the total electron density in the active region, and Σ is the confinement factor of the laser mode in the active region.

By using the transfer-matrix algorithm for calculating electron wave functions in a multi-quantum-well structure [70], we can simulate and solve the eigen wave functions of electrons, and obtain all the information, such as dipole moments, relaxation rates etc. In table 3.1, all parameters of device D3056 under 42 kV/cm bias are listed. Inserting those values into the coupled density matrix equations from Eq. (3.6) to (3.14), we can solve numerically the current density dependence of populations at each electron energy

state $n_i(j)$. Then we inserted the populations into the expression of the second order susceptibility Eq. (3.1) and obtained the current density dependence of the second order susceptibility, which is plotted in Fig. 3.7 (a). We compared it with the experimental data of nonlinear power conversion efficiency, which is shown in Fig. 3.7 (b), and found they followed similar tendency regarding the current density. It supports our hypothesis that the change of populations due to increasing current density caused the increase of the nonlinear power conversion efficiency.

Table 3.1 (a) Parameters of transitions between energy states from 1 to 4.

	2-1	3-2	3-1	4-3	4-2	4-1
Energy E_{ij} (meV)	N/A	141	148	122	263	270
Dipole moments (Å)	N/A	19.2	8.1	28.4	4.5	6.8
Life time τ (ps)	0.4	6.5	5.7	N/A	N/A	N/A

Table 3.1 (b) Life time τ from energy states to injector.

	4-i	3-i	2-i	1-i
Life time τ (ps)	N/A	1.7	1.0	0.9

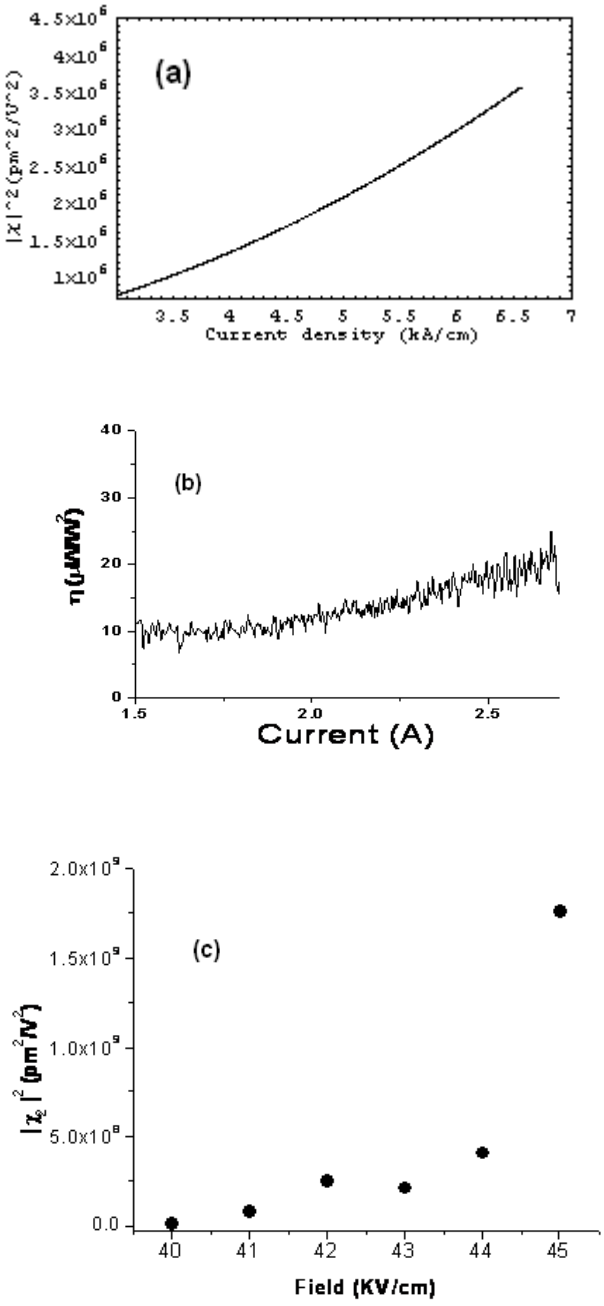

Fig. 3.7. The experimental result of the second order susceptibility and simulation results from two methods. (a) The simulation result of the second order susceptibility based on population solutions of coupled density matrix equations. (b) The experimental data of nonlinear power conversion efficiency. (c) The theoretical data of the absolute squared second order susceptibility based on different applied electric field.

The problem with this hypothesis is that the applied electric field was assumed unchanged in the simulation. However, it is probably not exactly true. The applied bias on cascade quantum-well structure increased somehow with the pump current. It can be seen from the L-I-V curves from Fig. 3.4. Therefore we studied the other hypothesis.

The slight change of the applied electric field with pump current caused the change of eigen wave functions for all electron energy states. It further caused the changing of dipole moments and energies of transitions. This affects the nonlinear susceptibility of the SHG process. From Fig. 3.8, we see a strong change in the wave function of energy state 3', which causes an increase of dipole moments between 3' and state 2 (4), when the electric field changes from 41 kV/cm to 45 kV/cm. Moreover, state 3' is the last state in the previous injector. It shares the Fermi level with state 3, namely the population of electron density at this state is large. Therefore the strong change of dipole moments of 3'-2 and 3'-4 will certainly cause a change of the nonlinear susceptibility.

Guided by this idea, we collected all the information on dipole moments and shifting of energy states from 40 kV/cm to 45 kV/cm. Given the condition that most of the electrons are located at either energy states 3 or 3' under the lasing condition, we calculated the nonlinear susceptibility versus the applied bias, as shown in Fig. 3.7 (c).

The result showed that the square of the nonlinear increased about 7 times from 42 kV/cm to 45 kV/cm. It indicated that the dipole moments and energy levels change due to a slight increase of an applied electric field could also be one of reasons of the increase of nonlinear power conversion efficiency.

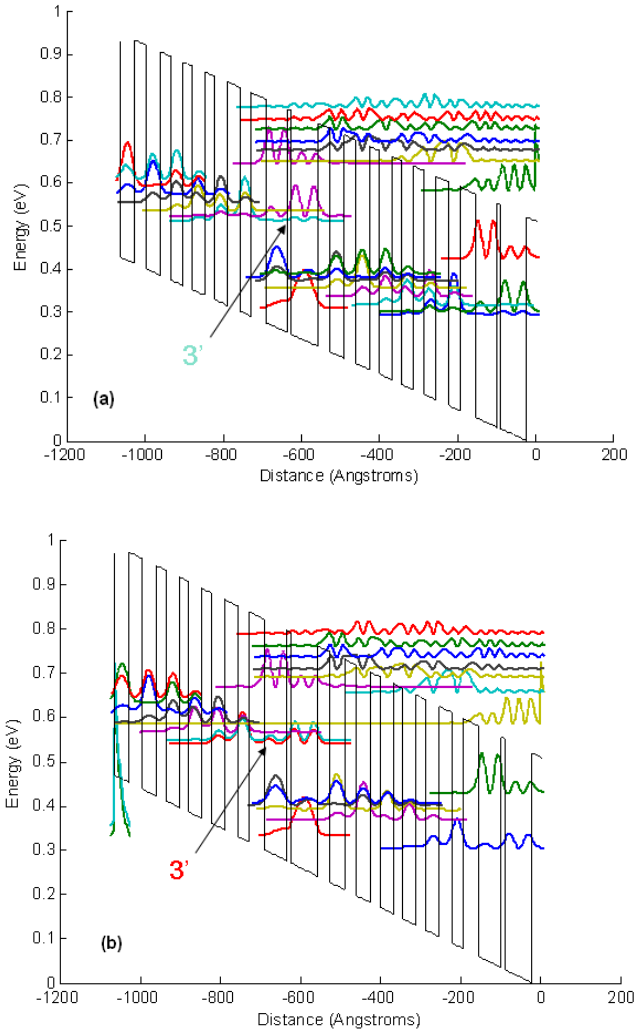

Fig. 3.8. The band diagrams of device D3056 at (a) 41 kV/cm, and (b) 45 kV/cm. The wave function of energy state 3' changed significantly. It caused strong change of dipole moments between 3'-2 and 3'-4.

As discussed above, both the change in populations due to increasing current density and the change in dipole moments caused by the shift of an applied electric bias could cause the variation of the nonlinear power conversion efficiency. The increase of nonlinear power conversion efficiency in SHG QCL device D3056 could be a mixed result of both mechanisms indicated above.

4. IN-PLANE MONOLITHIC INTEGRATION OF NONLINEARITIES WITH QCL *

4.1 Introduction

As discussed in previous two sections, the active region of a quantum cascade (QC) laser can be integrated with a cascade of intersubband transitions designed for a nonlinear conversion of laser light into coherent radiation at different frequencies [71]. The monolithic integration of optical nonlinearities with QCLs yields compact electrical current pumped devices, which are valuable from the practical point of view. Normally a nonlinear medium is required in a QCL structure. It can be a nonlinear active core with specifically designed quantum-well structures. Also, it can be designed in the very laser core so that there is only one active core in a device, as the DFG QCL and the SHG QCL discussed in previous two sections. However, in this method, it is sophisticate to design the active layers. There are tradeoffs between optimizing QCL and nonlinearities. It results in a poor flexibility to implement various nonlinearities, and probably poor performance for either pump laser or nonlinear susceptibilities.

Having a nonlinear active core separate from laser active core provides a good solution to flexibly design nonlinear active layers. We can grow an active core on top or

---

beneath the laser active core, namely vertically separate them, as shown in Fig. 4.1. This scheme is friendly to the device growth and processing procedures. However, it may compromise nonlinear conversion efficiency, because the modal overlap with laser and nonlinear stages could be low.

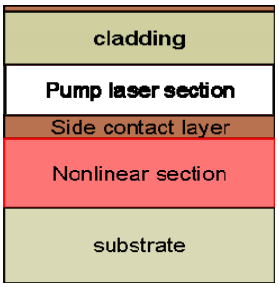

Fig.4.1. The scheme of the vertical integration of nonlinearities with QCL. The nonlinear active core (section) is separated from that of pump laser.

An alternative scheme of monolithic integration of nonlinearities within a QCL is proposed here, an in-plane integration scheme. In this scheme, a device is separated horizontally along the waveguide into a pump laser section and a nonlinear section. Two separated contacts induce two different applied voltage biases on two sections. This scheme provides a great flexibility to integrate optical nonlinearities with a QCL.

4.2 The Scheme of In-Plane Integration

The scheme of in-plane integration is shown in Fig. 4.2. There is only one epitaxial layer of active multi-quantum-well structure grown in a device. The whole

device is separated longitudinally, and two sections are applied different voltage bias on. Since the electron energy states in the quantum-well structures are depending on the applied bias or the electric field, each section can independently work as either a pump QC laser or an optical nonlinear element. Actually this scheme is similar to the two-section DFG diode laser [72].

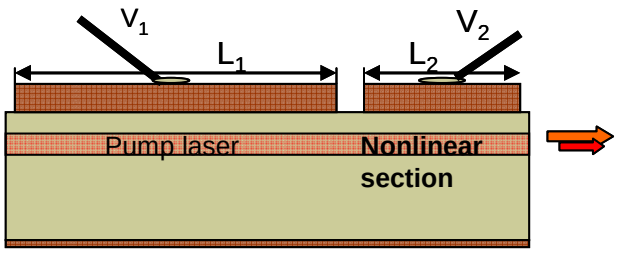

Fig. 4.2. The scheme of in-plane integration of nonlinearities. Two different parts operate under different voltage bias and serve two different functions: Pump laser and nonlinear conversion section.

Although the in-plane integration seems to have limited applications because the nonlinear section must share the same design of active core with the pump laser, surprisingly, this scheme shows great flexibility in implementing various nonlinearities. The in-plane integration scheme avoids some problems of both vertical integration and complete integration. The overlap between waveguide modes profile of pump laser and the nonlinear active section is usually much higher than that of vertical integration scheme, since the nonlinear active section shares the same area with that of the laser active section on the cross section profile of the device. An Additional advantage of the in-plane integration is that the nonlinear section is independently controlled by applied

bias, and it can be different from that of the QC laser section, which is usually under fixed applied bias to align all the energy states. Therefore a wide tunability of optical nonlinearities might be achieved by tuning the applied bias. Of course, the attention must be paid that the value of gain in the laser section g multiplied by the length of laser section L_1 should be higher than the sum of an absorption loss in the nonlinear section $\alpha_2 L_2$ and a total waveguide loss plus a mirror loss.

Various nonlinearities can be integrated with the in-plane scheme. The tunability of nonlinearities can result in a widely tunable laser if we integrate Raman scattering effect in the nonlinear section. SHG section in the in-plane integration scheme can yield a short wavelength emission at 2-4 μm by fully utilizing the whole depth of quantum-well structure. Moreover, by inserting a saturable absorber as the nonlinear section one can realize a mode locked laser.

4.3 Widely Tunable Raman Laser Based on the In-Plane Integration Scheme

The possibility of Raman amplification using intersubband transitions has been theoretically discussed in Ref. [73]. The first Raman laser based on ISBT in a GaAs/AlGaAs double quantum well structure was demonstrated in 2001 with an external CO_2 laser pumping source [52]. Monolithic integration with a pump laser, the first injection-pumped Raman laser, which was demonstrated in 2005, showed very high conversion efficiency of about 30 % [47].

The tunability in conventional Raman lasers or amplifiers is associated with changing the wavelength of an external pump laser, while the Stokes (or Anti-Stokes) shift remains fixed. In the in-plane integration scheme, we have a different situation. The Raman shift which is determined by the energy difference of two lower subbands depends by the applied bias on the nonlinear section, although the QC pump laser in the laser section has very limited tunability, which does not affect the Raman scattering processes. Therefore a widely tunable Raman laser is achievable.

Almost every QCL's active region is a potential Raman scattering active region under certain applied electric field due to the phonon scattering design for the depletion of lower laser level. For example, the active region of a high power QCL at 8 μm works under an electric field of 60 kV/cm [27], as shown in Fig. 4.3 (a). The same quantum-well structure of a QCL can serve as a Raman laser under a different electric field on the nonlinear section. In this case, as shown in Fig. 4.3 (b), the same structure shows the property of a Raman scattering medium under a bias of -10 kV/cm. The Raman shift equals the energy separation of energy state *1* and *2*. The transition 1-3 is close to the resonance of pump laser, but with a detuning of about 10 meV. A strong resonant absorption is avoided.

We can obtain the gain *g* at the Stokes frequency by solving the density matrix equations [64].

$$g_s = \frac{4\pi\omega_s e^2 d_{32}^2 \Gamma_{eff}}{\hbar c n_s} \mathrm{Re}\{\frac{1}{\Gamma_{32} + |\Omega_d|^2 / \Gamma_{21}^*}[\frac{|\Omega_d|^2 (n_1 - n_3)}{\Gamma_{21}^* \Gamma_{31}^*} - (n_2 - n_3)]\}, \qquad (4.1)$$

where

$$\Gamma_{32} = \gamma_{32} + i(\omega_{32} - \omega_s) \,, \tag{4.2}$$

$$\Gamma_{31} = \gamma_{31} + i(\omega_{31} - \omega_d) \,, \tag{4.3}$$

$$\Gamma_{21} = \gamma_{21} + i(\omega_{21} - \omega_d + \omega_s) \,, \tag{4.4}$$

$$\Omega_d = ed_{31}E_d / \hbar \,, \tag{4.5}$$

where E_d is the electric field of internal optical pump, d_{mn} is the dipole moment of transition m-n, γ_{mn} is the broadening or dephasing rate of transition m-n, ω_d and ω_s are the frequencies of pump and Stokes respectively, Γ_{eff} is the optical confinement of the Stokes signal, n_s is the effective refractive index of Stokes mode, and n_i (i=1,2,3) is the electron density at ith energy state.

In the nonlinear section, most of the free electrons from the dopants at injection layers of QCL [22] stay at the lowest state, level 1. It means n_2~0 and n_3~0 in Eq. (4.1). A positive gain at Stokes frequency is reached. Therefore, as long as the intensity of pump field is strong enough, the optical gain at the Stokes frequency would overcome the loss and then the Stokes frequency would be at lasing.

The Raman shift depends on the applied electric field on the nonlinear section, as mentioned above. The energy separation of transition 3-2 E_{21} is changed from 48 meV to 59 meV when a different electric field, such as -30 kV/cm, is applied, as shown in Fig. 4.3 (c). It means the Stokes signal is tuned with more than 10 meV. More details about the variation of the parameters of the Stokes effect is listed in Table 4.1.

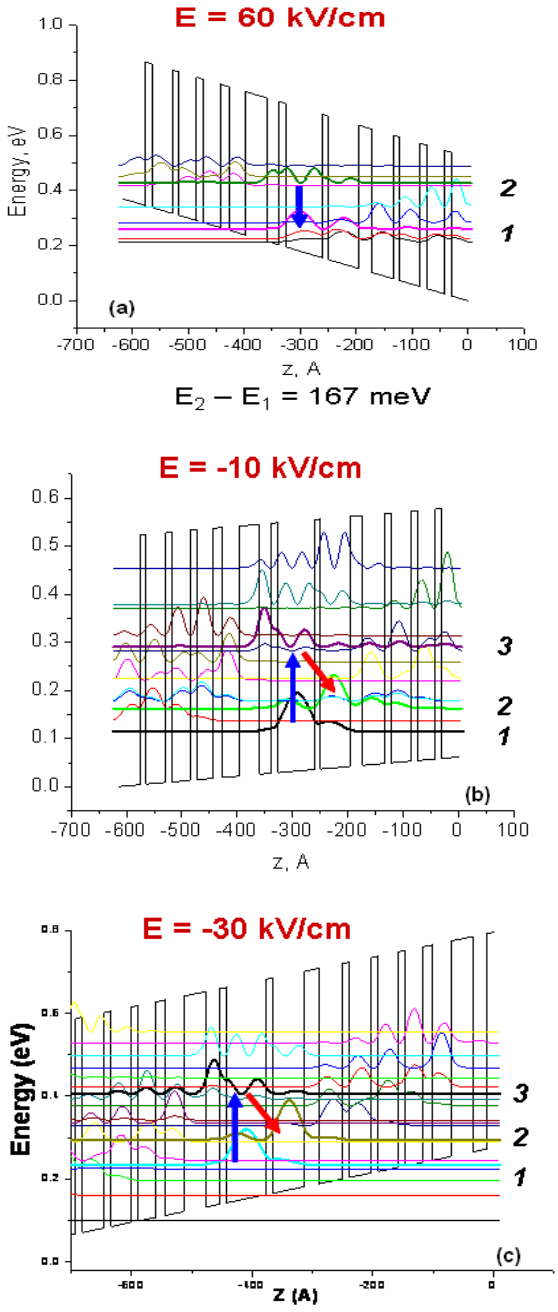

Fig. 4.3. The QCL structure under different biases. (a) The band diagram of an 8 μm QCL under an electric field of 60 kV/cm. The laser transition is 2-1. (b) The band diagram of the same structure in nonlinear section under an electric field of -10 kV/cm. The energy state 1, 2, and 3 form a Raman scattering active region. (c) The band diagram of the structure under a bias of -30 kV/cm.

Table 4.1. Parameters of energy separation and dipole moments at different applied electric fields.

Electric field	E_{12} (meV)	E_{13} (meV)	d_{13} (Å)	d_{23} (Å)
-5 kV/cm	44	178	9.7	13.2
-10 kV/cm	48	175	9.9	15
-15 kV/cm	51	173	10.6	16.4
-20 kV/cm	54	171	9.5	14.4
-25 kV/cm	57	166	8.5	13.6
-30 kV/cm	60	171	10.4	16.7
-35 kV/cm	63	169	11	17.4
-40 kV/cm	65	168	10.6	15.8
-45 kV/cm	69	165	11.8	19.4
-50 kV/cm	71	164	12.1	19.7

From the data in Table 4.1, we obtained more than 25 meV tunability of the Raman shift E_{12}, by changing the applied bias from -5 kV/cm to -50 kV/cm. On the other hand, the energy separation E_{13} changes only slightly and still keeps near resonance with the pump. The reason of different variations of energy separations is that the transition 2-1 is diagonal in space domain and would experience a linear Stark effect, while the transition 3-1 is a vertical transition and would experience a quadratic Stark effect which is much weaker.

From Eq. (4.1), we know that the Raman gain is proportional to the square of the dipole moment between states 3-2. It also depends on the dipole moment between 3-1 through the Rabi frequency Ω_d. With increasing applied bias on the nonlinear section, from the data in Table 4.1, the dipole moment d_{13} was kept stable, and the dipole d_{23}

even increased about 50%. It means a stable or even slightly increased Raman optical gain can be achieved when more than 0.6 meV per kV/cm tunability is realized by adjusting the applied electric field on the nonlinear section.

Although more tunability may be achieved with even higher applied electric field, the population of electrons at lowest energy state might be depleted by an increased current with a higher electric field. Moreover a smaller energy separation between 3-1 at a higher electric field would cause a strong absorption at the nonlinear section, which should be avoided.

This is just one example. Although the tunability still is limited by certain electric field bias, we still can spatially separate energy states 1 and 2 to increase the linear Stark effect and achieve more tunability per unit change of electric field.

4.4 The In-Plane Integration for Second Harmonic Generation

The Raman scattering is not the only nonlinearity which can be implemented with the in-plane integration scheme. With SHG one can extend the emission wave-length to 3 μm or shorter, as discussed in the first section.

Since a lot of details of integrating SHG with a QCL have been discussed in section 3, we just show schematically the in-plane integration of SHG process here.

A coupled quantum-well structure of 63/20/42 Å, which is designed for the active region of a QCL working at 6.4 μm, is shown in Fig. 4.4 (a). It is under an applied

electric field of 60 kV/cm. But, in the nonlinear section, the same structure is under an electric field of -20 kV/cm. The electron energy states in the couple quantum well form two sets of three-level systems of SHG process, with about 20 meV detuning from resonance, as shown in Fig. 4.4 (b). A SHG signal at 3.2 μm is expected. In one of the three-level systems, the dipole moments are d_{12}=14 Å, d_{23}=19 Å, and d_{13}=2 Å. As a result, a second order susceptibility of 10^4 pm/V is estimated with an average doping rate of 10^{17} cm^{-3}.

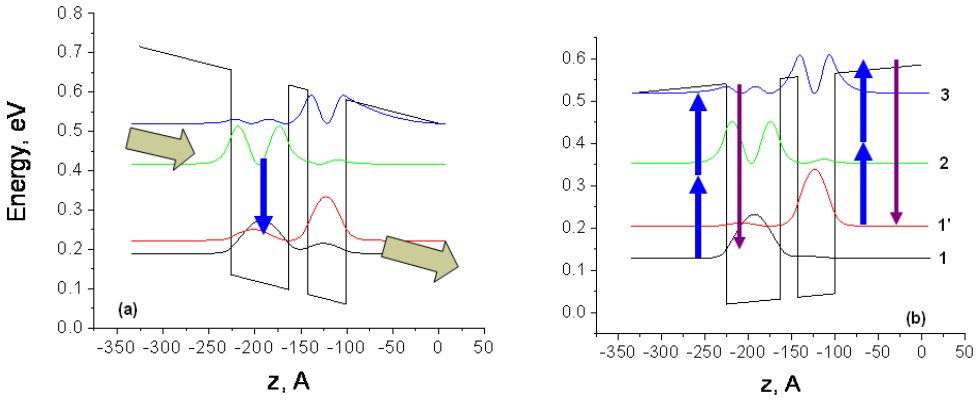

Fig. 4.4. The band diagrams of a couple double quantum-well structure. (a) The structure is under an electric field of 60 kV/cm and serves as a QCL working at 6.4 μm. The gray arrows indicate the direction of injected electron current. (b) The structure is under an electric field of -20 kV/cm and forms two three-level systems, 1-2-3 and 1'-2-3.

A shorter wavelength of SHG signal can be realized by using a strain-compensated semiconductor material system, such as $Ga_{0.41}In_{0.59}As$/ $Al_{0.56}In_{0.44}As$, which has a higher conduction band offset between the barrier and the well materials. Therefore a deeper quantum well structure can be used to accommodate further

separated energy states. For example, a double quantum-well structure of 68/14/49 Å works as an active core of a QCL at 6 μm under an electric bias of 60 kV/cm, and works as a SHG medium at the nonlinear section under a bias of -60 kV/cm, with 15 meV of detuning from resonance.

Overall, the scheme of in-plane integration of optical nonlinearities with QCLs shows strong promising results in implementing various nonlinear processes, such as the Raman scattering and SHG. More applications can also be achieved with this scheme. For example, THz emission based on the frequency-down conversion is also available with a Raman scattering scheme [71].

5. FREQUENCY UP-CONVERSION IN COUPLED QUANTUM-WELL STRUCTURE FOR MID/FAR-IR DETECTION

5.1 Introduction

Quantum cascade lasers and the optical nonlinearities integrated QCLs are promising optical sources at infrared range. On the other hand, optical nonlinearities can also be implemented for mid-infrared (mid-IR) detection.

There are two main types of photo-detectors in the infrared range, thermal and photonic. Thermal type IR detectors utilize the thermal effect of incident IR radiation and various temperature dependent phenomena. They include detectors based on changes in resistance with temperature, such as bolometers and mircobolometers, or detectors based on thermoelectric effect, such as thermocouples and thermopiles. Photonic type IR detectors mainly are based on the interaction between photons and electrons in semiconductors. Usually they have much better response time and sensitivity than thermal type detectors. Most infrared photonic detectors are based on narrow band gap semiconductor materials. Electrons are excited from valence band or impurity states to conduction band by the incident IR radiation, and then the conductivity change or the photo-voltage generated in a p-n junction is monitored. The most commonly used photonic detectors include Mercury Cadmium Telluride (MCT) detectors with a spectral range from 0.8 μm to 25 μm, InGaAs photodiodes with a

spectral range from 0.7 μm to 2.6 μm, and InAs photovoltaic detectors with a spectral range from 1 to 3.8 μm. Although very sensitive, they usually need to be cooled to cut thermal noise.

Another type of photonic IR detectors is quantum well infrared photodetectors (QWIP) [74], which utilize intersubband transitions of electrons (n-type QWIP) [76-79] or holes (p-type QWIP) [80-84]. Due to the selection rules in conduction band ISBT, the n-type QWIP can not couple with a normally incident radiation, or they require grating on the top [83] of a structure. However, the p-type QWIP usually allow normal incident optical coupling without any grated structure, but typically the hole intersubband absorption is weaker than both the conduction ISBT and the valence band to conduction band absorption [74].

Currently existing mid/far-infrared semiconductor photodetectors, as mentioned above, already demonstrate near background-limited performance at low temperatures. Fig. 5.1 shows the various types of semiconductor photodetectors and the back ground limit at room temperature. However, at room temperature, they suffer from high dark currents due to thermal excitations across low-energy interband or intersubband transitions. Furthermore the performance is limited by the exponentially raising background limit at mid/far-IR range when compared to their near-IR counterparts. These are physical fundamental limits which can not be avoided by any method of direct detection.

An alternative method of mid/far-IR detection is using frequency up-conversion technology to convert mid/far-IR radiation to near-IR or visible wavelength by suitable

nonlinear optical interaction [85-87]. This approach can utilize superior near-IR/visible photo detectors, such as avalanche photodiodes (APD), which have detectivities several orders higher than mid/far-IR detectors, as shown in Fig. 5.1.

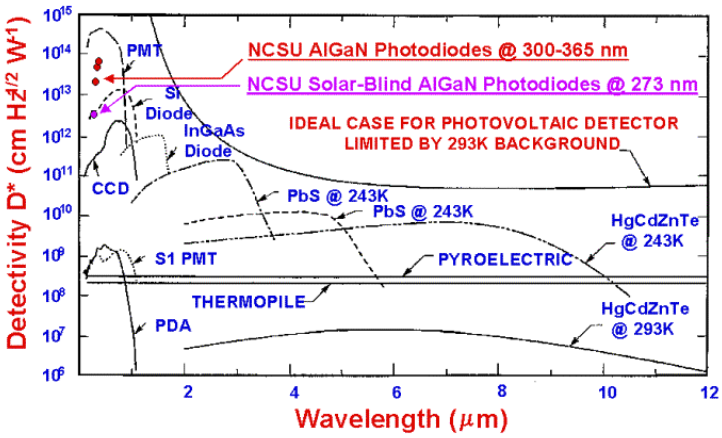

Fig. 5.1. Detectivity curves for various type infrared photodetectors at room temperature and the background limit.

Frequency up-conversion is basically an optical nonlinearity, sum frequency generation, as shown in Fig. 5.2. An optical field at low frequency is mixed with a strong pump light, and correspondingly an optical at higher frequency is generated. Frequency up-conversion is widely used in chemical materials imaging and telecom applications [88-89]. In the area of telecom, efficient up-conversion from 1.3-1.55 μm into the operation range of silicon APDs has been achieved [90-91]. Frequency up-conversion from mid-IR was achieved in as early as 1995 [92], and it is proposed to be used at free space communication [93]. Recently mid-IR single photon counting using sum frequency generation in a periodically poled lithium niobate crystal and a silicon APD

has been reported [94]. However, the conversion efficiency in frequency up-conversion for mid/far-IR detection can still be improved by substituting the nonlinear crystal with a properly designed quantum-well structure.

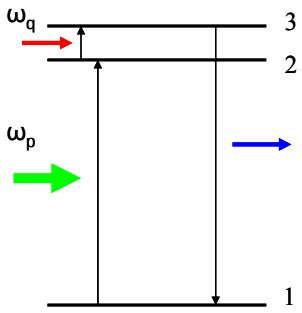

Fig. 5.2. The scheme of frequency up-conversion, usually the frequency of strong pump light ω_p is much higher than that of incoming signal ω_q. As a result, a sum frequency (ω_q+ω_p) is generated.

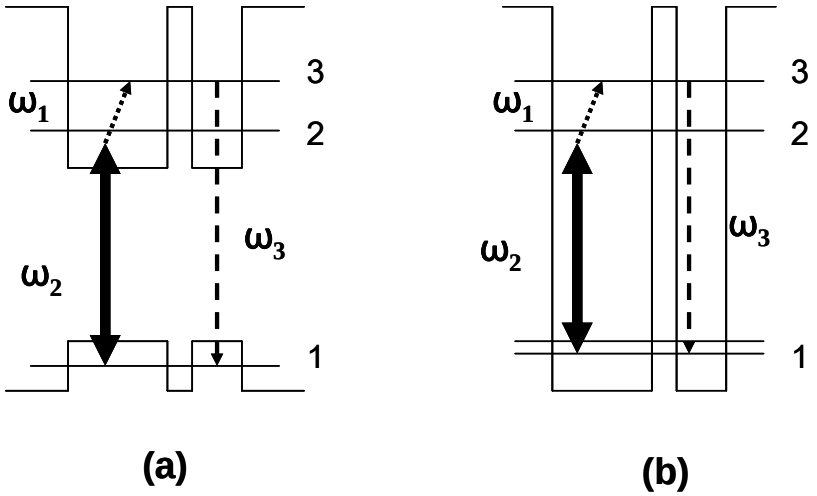

Fig. 5.3. A sketch of near-resonant SFG employing interband and intersubband transitions, (a), or intersubband transition only, (b). The bold solid lines represent the near-IR pump light at frequency ω_2, dotted lines represent the mid/far-IR signal at frequency ω_3, dashed lines represent the up-conversion radiation at frequency $\omega_3=\omega_1+\omega_2$.

5.2 Frequency Up-Conversion Scheme with Quantum-Well Structures

As discussed in previous sections, nonlinearities could be strongly enhanced in a resonant cascade scheme where fields are near resonance with the optical transitions in cascade quantum-well structures [27,49,51,95]. Based on this idea, we designed frequency up-conversion processes in quantum-well structures, in which both intersubband and interband transitions were employed. A sketch of near resonant up-conversion with interband and intersubband transitions or intersubband transitions only is shown in Fig. 5.3 [85].

Due to the different selection rules of conduction-band intersubband transitions and interband transitions [74], different geometries are used to couple optical fields. If only conduction intersubband transitions are employed, only z-polarized component of both pump and signal fields could be coupled, namely both of them are induced from the side of the structure. If the interband transition is employed, as shown in Fig. 5.3 (a), the pump light will be induced with normal incidence, but the mid-IR signal will be induced from the side. They result in different optical geometries. A specific structure will be discussed below.

A double coupled structure for frequency up-conversion of type (a) was designed as 32/20/22 Å, where the well material is InP lattice matched InGaAs, and the barrier material is AlInAs, as shown in Fig. 5.4. The relative energy states are shown in Fig. 5.5.

As shown in the figure, the energy subbands *hh1-e1-e2* form a three-level system of SFG. The structure is designed to convert a mid-IR signal at 10 μm, with a strong near-IR optical pump at 1.3 μm, to near-IR 1.15 μm. The structure is not intentional doped; therefore idealy the whole population of electrons is on the valence subband hh_1 at low temperature.

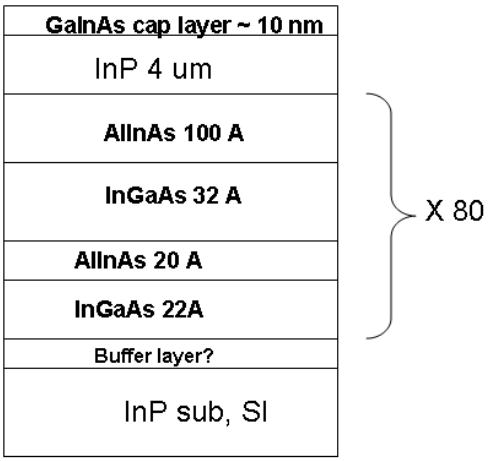

Fig. 5.4. The profile of cascade double wells structure for frequency-up conversion scheme.

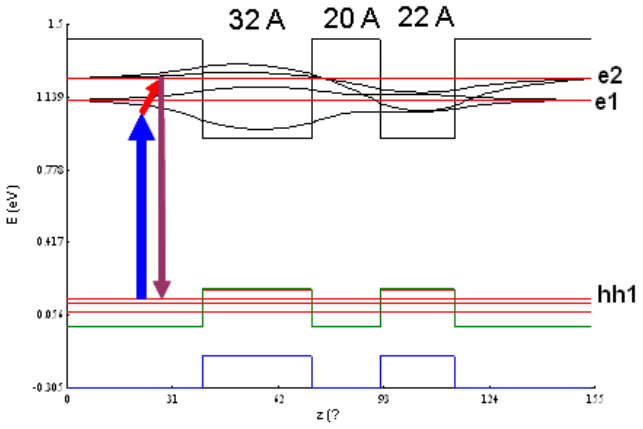

Fig. 5.5. The band diagram of the double quantum-well structure for the frequency up-conversion.

5.3 The Nonlinear Susceptibility for Frequency Up-Conversion

As we always mentioned, one of the most important things in a nonlinear process is the nonlinear susceptibility. However, in this scheme, because the band dispersions of the conduction subband and the valence subband have opposite signs, the energy separation between them varies, depending on the electron momentum vector $k_{||}$, which is the momentum component parallel to the interface of semiconductor layers. Due to this reason, the conduction subbands and the valence subband can not be treated as simple sharp energy levels.

Given a three-level system with all electron population located on lowest energy level, we can describe the nonlinear susceptibility of sum-frequency generation $\chi^{(2)}$ as:

$$\chi_{ijk}^{(2)}(\omega_1+\omega_2,\omega_1,\omega_2) \cong \frac{N}{2\hbar^2}\cdot\frac{u_{lm}^{i}u_{nl}^{j}u_{mn}^{k}}{[(\omega_{nl}-\omega_1-\omega_2)-i\cdot\gamma_{nl}][(\omega_{ml}-\omega_1-i\cdot\gamma_{ml})]}, \qquad (5.1)$$

where all electrons are assumed on level l, N is the electron density, ω_1 and ω_2 are pumping light and probe light frequencies respectively, $u_{lm}^{i}=e\cdot d_{lm}^{i}$ is the ith component of the dipole moment between level l and m, and γ_{nl} is the homogeneous broadening of the transition between levels n and l.

As mentioned above, the subbands of conduction band have opposite sign of effective mass against that of valence band, as shown in Fig.5. 6. The energy differences depend on $k_{||}$, and so do the dipole moments and electron density of states. The result is the nonlinear susceptibility also depends on $k_{||}$. The total nonlinear susceptibility could be expressed as an integral over $k_{||}$:

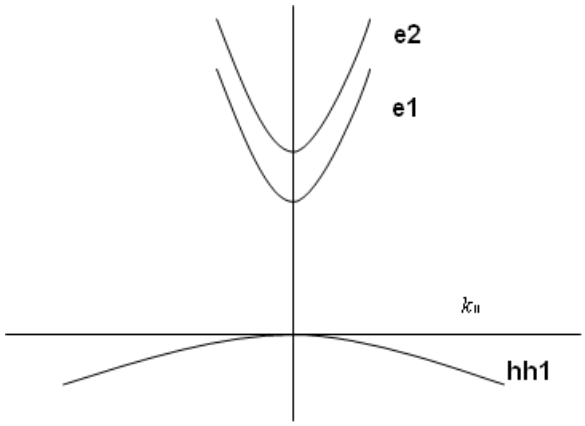

Fig. 5.6. The sketch of band dispersion of conduction and valence subbands vs $k_{||}$ vector.

$$\chi_{tot}^{(2)} = \int \chi^{(2)}(\omega_3 = \omega_2 + \omega_1, \omega_2, \omega_1, k_{||}) \cdot d\vec{k}_{||}^{\,2} \,, \tag{5.2}$$

where

$$\chi^{(2)}(\omega_3 = \omega_2 + \omega_1, \omega_2, \omega_1, k_{||}) = \frac{1}{2\hbar^2}\frac{\partial N}{\partial k_{||}} \times \frac{u^i_{v,c2}(k_{||})u^j_{v,c1}(k_{||})u^k_{c1,c2}(k_{||})}{[\omega_{c2}(k_{||}) - \omega_v(k_{||}) - \omega_3 - i\cdot\gamma_{c2,v}][\omega_{c1}(k_{||}) - \omega_v(k_{||}) - \omega_1 - i\cdot\gamma_{c1,v}]} \,, \tag{5.3}$$

where $\frac{\partial N}{\partial k_{||}}$ is the density of states per unit volume, and $\frac{\partial N}{\partial k_{||}} = \frac{1}{2\pi^2 L}$, L is the thickness of the quantum well. With parabolic approximation for the $k_{||}$ dependent energy bands, we have:

$$\omega_{c1}(k_{||}) = \frac{E_{c1}}{\hbar} + \frac{\hbar k_{||}^2}{2m_1^*} \,, \quad \omega_{c2}(k_{||}) = \frac{E_{c2}}{\hbar} + \frac{\hbar k_{||}^2}{2m_2^*} \,, \quad \omega_v(k_{||}) = \frac{E_v}{\hbar} + \frac{\hbar k_{||}^2}{2m_v^*} \,, \tag{5.4}$$

where E_{c1}, E_{c2} are the minimum values of two selected conduction subbands, E_v is the maximum value the selected valence subband; m_1^*, m_2^*, m_v^* are the effective masses of

each subband, and m_v^* is negative. Furthermore, we also assumed that the dipole moments are independent on $k_{\|}$. After that, we may write the second order susceptibility of the system as:

$$\chi_{tot}^{(2)} = \int_0^{k_b} \frac{k_{\|} dk_{\|}}{2\pi L\hbar^2} \frac{U}{(\delta_2 + \frac{\hbar k_{\|}^2}{2m_{r2}^*} - i\gamma_{c2,v})(\delta_1 + \frac{\hbar k_{\|}^2}{2m_{r1}^*} - i\gamma_{c1,v})}, \tag{5.5}$$

where k_b is the value of $k_{\|}$ at the edge of the Brillouin zone, $U = u_{v,c2}^i u_{v,c1}^j u_{c1,c2}^k$,

$\delta_1 = \frac{E_{c1} - E_v}{\hbar} - \omega_1$, $\delta_2 = \frac{E_{c2} - E_v}{\hbar} - \omega_3$, $1/m_{r1}^* = 1/m_1^* - 1/m_v^*$, and $1/m_{r2}^* = 1/m_2^* - 1/m_v^*$.

We replaced $\gamma_{c2,v}$ and $\gamma_{c1,v}$ by a common factor γ. After integration and some approximation, the second order susceptibility is obtained as

$$\chi^{(2)} = \frac{U}{2\pi L\hbar^3} \frac{m_{r1}^* m_{r2}^*}{\delta_1 m_{r1}^* - \delta_2 m_{r2}^* + i\gamma(m_{r2}^* - m_{r1}^*)} \times \left[\frac{1}{2}\ln\frac{m_{r1}^*(\delta_1^2 + \gamma^2)}{m_{r2}^*(\delta_2^2 + \gamma^2)} + i(\tan^{-1}\frac{\delta_1}{\gamma} - \tan^{-1}\frac{\delta_2}{\gamma})\right]. \tag{5.6}$$

For the structure designed above, we have the dipole moments $d_{v\text{-}c1}$=7 Å, $d_{v\text{-}c2}$= 1.5 Å, and $d_{c1\text{-}c2}$=25 Å. With assuming $m_{r1}^* \approx m_{r2}^* \approx 0.06m_e$, $L \approx 1\times10^{-6} cm$, and $\hbar\gamma \approx 10meV$, we estimated $\left|\chi^{(2)}\right|$ about $1.2\times10^{-5} statV^{-1}\cdot cm$.

To avoid resonant absorption for the pump light, detuning of about 20 meV for pump is usually introduced. In this case, detuning by less than 35 meV of mid-IR signal from transition e_1 to e_2 is allowed without significantly decreasing the absolute square of the nonlinear susceptibility, as shown in Fig. 5.7.

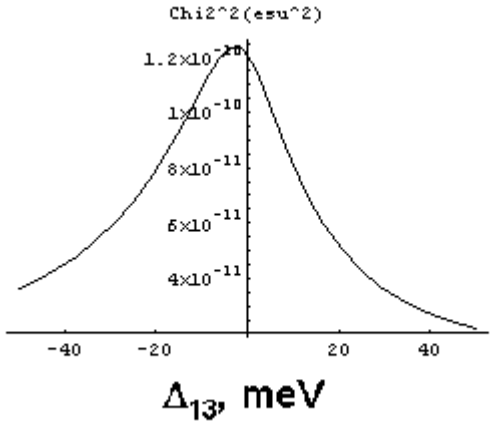

Fig. 5.7. The spectrum of absolute square of $\chi^{(2)}$ vs detuning $\Delta_{v\text{-}c2}$ with 20 meV detuning of pump. The bandwidth of $|\chi^{(2)}|^2$ is about 35 meV.

5.4 Optimization of Double Quantum-Well Structure for Frequency Up-Conversion

The nonlinear susceptibility is proportional to the product of three dipole moments, $d_{v\text{-}c1}$, $d_{v\text{-}c2}$, and $d_{c1\text{-}c2}$, as indicated in Eq. (5.6). To maximize the product of dipole moment and optimize the nonlinear susceptibility, we need to decide the thickness of two wells (t_1, t_3) and barrier (t_2). We investigated the asymmetrical ratio effect to the product of dipole moments, as shown in Fig. 5.8. It seems that an asymmetrical ratio of about 0.1 results in an optimized product of dipole moments.

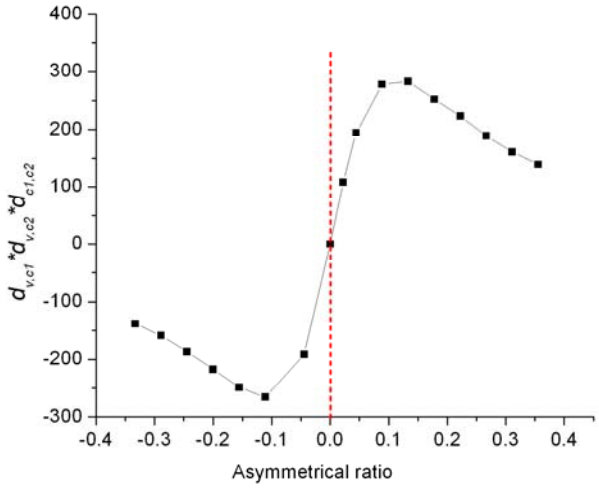

Fig. 5.8. The asymmetric effect of the product of dipole moments. The asymmetry ratio is defined as $(t_1-t_3)/(t_1+t_2+t_3)$. The total thickness is 90 Å, with t_2=10 Å.

The energy of mid-IR resonant transition *e1-e2* is also dependent on the asymmetrical ratio, as shown in Fig. 5.9.

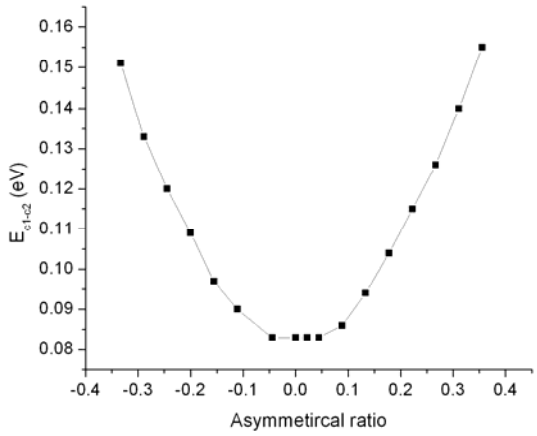

Fig. 5.9. The asymmetry ratio of energy separation of states e_1 and e_2. The total thickness is 90 Å, with t_2=10 Å.

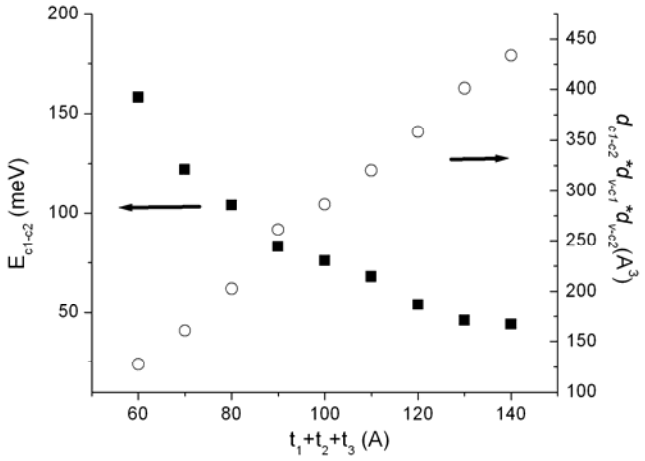

Fig. 5.10. The effects of total thickness on the energy separation of states e_1 and e_2, and the product of three dipole moments.

The effects of total thickness of quantum-well structure (t_1+t_2+t_3) on the transition energy of *e1-e2* and the product of three dipole moments are also investigated, as shown in Fig. 5.10. The product of the dipole moments increases with the total thickness, and the transition energy decreases with the total thickness. Based on the results of Fig. 5.8-5.10, we can design and optimize the double quantum-well structure for a specific mid-IR wavelength at which we want to detect the mid-IR signal. The total thickness would be determined first, and then the asymmetry ratio would be adjusted to optimize the structure.

5.5 The Optical Geometry for the Frequency Up-Conversion Scheme

The frequency up-conversion process in the structure shown in Fig. 5.5 only couples the z-polarized component of mid-IR signal and x- or y-polarized component of near-IR optical pump field. Therefore, a crossed beam optical geometry, which is particularly convenient for phase-matching, is employed, as shown in Fig. 5. 11. The mid-IR signal is propagating in x-direction, and the near-IR pump is induced in z direction. The SFG signal is coming out from the surface with an angle to the normal direction of the surface.

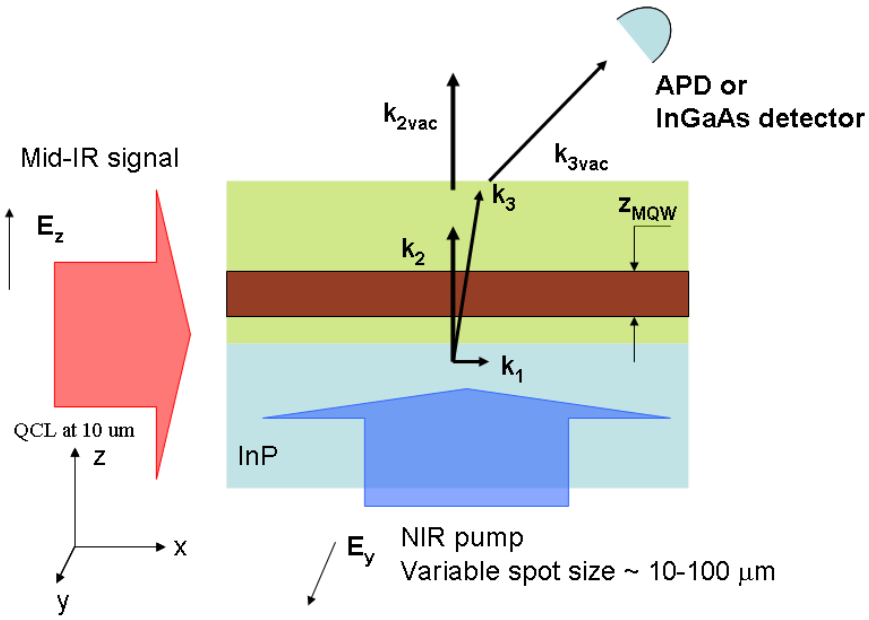

Fig. 5.11. The optical geometry of the quantum-well structure for mid-IR detection frequency up-conversion. The mid-IR signal is propagating in x-direction, and is coupled into the waveguide as a TM mode. The y-polarized near-IR pump is incident in z direction, hitting the substrate of a structure.

Since the thickness of active region Z_{MQW} is usually very small (less than one micrometer), the phase matching condition becomes

$$\Delta k_x = k_1 - k_x = 0 \,. \tag{5.7}$$

The propagating direction of the SFG signal in the structure for phase matching condition must satisfy Eq. (5.7), namely the angle of between vector k and k_2 is approximately $\tan^{-1}(k_1/k_2)$, i.e. about 7 degree for the structure discussed above. After entering air, the SFG propagates with an angle of about 20 degree to the normal direction of the surface of structure. The separation of the weak SFG signal from original strong near-IR pump light could help retrieving the SFG signal with an APD or other near-IR detectors.

Given a pump light with intensity I_2 and a mid-IR signal power of P_1, a frequency up-conversion structure with a thickness of L_z and a length of L_x, we calculated the power of the SFG signal, by solving Maxwell's equations as [85]

$$P \cong \frac{8\pi^3\omega^2}{c^3 n_1 n_2 n}\left|x^{(2)}\right|^2 L_x L_z \Gamma I_2 P_1 \,, \tag{5.8}$$

where Γ is the coupling confinement factor of mid-IR signal with the active region in the waveguide like structure, n_1, n_2, and n are the refractive indices of three optical fields in the active region.

5.6 The Figure of Merit of Frequency Up-Conversion Scheme for Mid-IR Detection

The main figures of merit of the frequency up-conversion scheme for mid-IR detection are responsivity *R*, and the noise equivalent power (NEP). The later one determines the detectivity *D*, a basic parameter of a detector, as

$$D^* = \frac{\sqrt{A \cdot \Delta f}}{NEP}\ , \qquad (5.9)$$

where A is the area of the photosensitive region of the detector, Δf is the effective noise bandwidth. The detectivity of a detector decides how faint a signal can be detected with this detector. On the other hand, the responsivity R is the parameter determining how strong of the current signal can be received in the detector based on one unit power of incident optical signal, and it can be expressed as

$$R = \frac{I_{APD}}{P_1} = \eta_{up}\eta_c R_{APD}\ , \qquad (5.10)$$

where R_{APD} is the APD responsivity, up-conversion efficiency $\eta_{up}=P/P_1$, and η_c is the coupling efficiency of the SFG signal to APD. The R_{APD} of a Si APD can reach 100 A/W at near-IR range [97], which is more than 100 times larger than that of regular mid-IR detector. The coupling efficiency can be close to 1. The up-conversion efficiency η_{up} can reach 0.1% with a pump intensity of 10^6 W/cm^2 in our structure.

Although there are two steps in the scheme, up-conversion process and subsequent detection by a near-IR APD, the NEP can still be suppressed. There are several main sources of noise for the detection system, an intrinsic noise of the near-IR APD, the background radiation at the frequency of SFG, the background radiation at the

mid-IR signal frequency which is up-converted by the SFG process, and the spontaneous recombination emission of the QW structure in the absence of a signal. The NEP can be described as

$$\mathrm{NEP} = \frac{\hbar\omega_1}{\eta_{tot}}\langle n_{tot}\rangle = \frac{\hbar\omega_1}{\eta_{tot}}(\langle n_{DC}\rangle + \langle n_{BG}^{up}\rangle + \langle n_{BG}^{NIR}\rangle + \langle n_{sp}\rangle), \tag{5.11}$$

where $\langle n_{DC}\rangle$ is the equivalent photon number of the intrinsic noise in an APD, $\langle n_{BG}^{up}\rangle$ is that of mid-IR background radiation within a bandwidth of about 30-40 meV at frequency ω_1, $\langle n_{BG}^{NIR}\rangle$ is that of near-IR background radiation, $\langle n_{sp}\rangle$ is that of noise due to the spontaneous recombination, and the total photon conversion efficiency η_{tot} is given by

$$\eta_{tot} = \frac{\omega_1}{\omega}\eta_{up}\eta_c\eta_{APD}, \tag{5.12}$$

where η_{APD} is the quantum efficiency of APD.

Among the sources of NEP, as described in Eq. (5.11), the intrinsic noise of an APD is very low. Recently a NEP value of an InGaAs APD at room temperature was reported as 10^{-15} W/Hz$^{1/2}$ [96]. For the noise from mid-IR, the strong mid-IR background noise can be filtered out, because only a small part of the background radiation at a specific range of frequency and spatial mode will pass the selective up-conversion process, and then be detected by an APD. Therefore the value of $\langle n_{BG}^{up}\rangle$ is very small. The background of near-IR radiation is much lower than that of mid-IR range, as discussed in the introduction. The noise from the spontaneous recombination at the near-IR range depends on the population at the conduction subbands. For an un-doped

quantum-well structure, the electrons at the conduction subbands are mainly due to the excitation of electrons and holes by the near-IR pump. It can be greatly suppressed by introducing proper detuning of the near-IR pump from the band gap. By introducing a detuning of about 30 meV, with a pump intensity of 10^6 W/cm^2, the NEP value due to the spontaneous recombination is less than the intrinsic NEP value of an APD. Overall, the total NEP level of the detection system is much less than that of a regular mid-IR photo detector at room temperature.

Overall, the proposed mid/far-IR photo detection scheme based on a coherent SFG process in the coupled quantum-well showed high detectivity at room-temperature comparable to that of state of the art mid-IR detectors. The up-conversion efficiencies in the coupled quantum-well structures are significantly improved compared to that of a nonlinear crystal. The scheme can be further implemented with a diode pump laser, and an injection-pumped device can be yielded.

6. LASING WITHOUT INVERSION IN THE QUANTUM CASCADE LASER FOR TERAHERTZ EMISSION

6.1 Introduction

The concept of lasing without inversion (LWI) was first introduced by S. E. Harris, M. Scully, and O. Kocharovskaya *et al.* at the end of 1980's [98-99], although some elemental ideas came out much earlier [100, 110-111]. The basic idea of LWI is to introduce a quantum coherence or interference in the medium with a strong driving field, and to partially eliminate resonant absorption on another transition or to achieve an optical gain without the population inversion on the transition of interest [64, 101-104].

The LWI has been intensively studied theoretically and experimentally since then. A review of LWI is given in Ref. [105]. Experimental demonstrations of LWI or AWI (amplification without inversion) have been reported since 1993 [106-109]. Mainly, LWI has been proposed in both a two-level system and a three-level (or multi-level) system. The examples of the former included recoil-induced lasing [110] and coherently driven two-level systems [111]. The LWI in a three-level system can be realized by introducing Fano-type quantum interference [98, 100], or with a coherently optical driven transition [99,112]. Usually LWI in three-level systems were proposed with three types of scheme, cascade or ladder type scheme, V-type scheme, and Λ-type scheme, as shown in Fig. 6.1 [113].

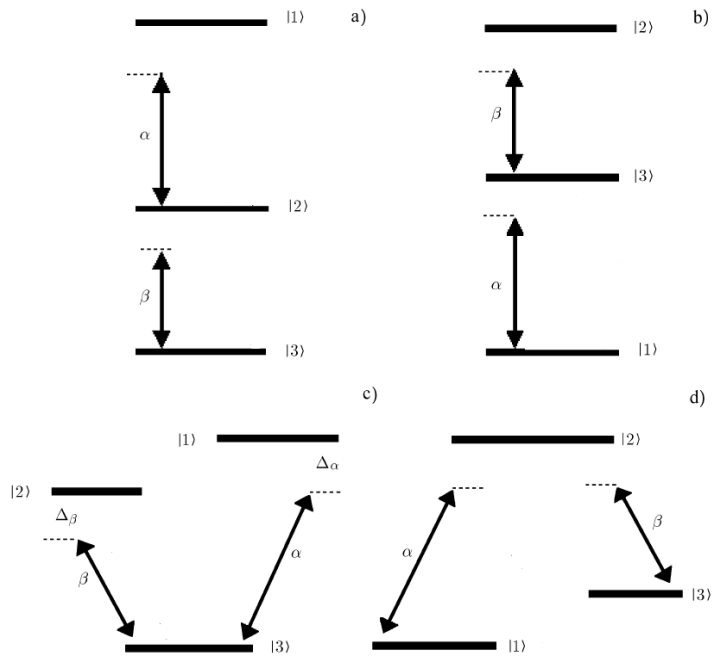

Fig. 6.1. Various schemes of LWI in three-level systems. (a) Cascade or ladder scheme with pump β at lower transition. (b) Ladder scheme with pump at higher transition. (c) V type scheme. (d)Λ type scheme.

Most of the LWI schemes require a strong external driving. However, external optical driving would usually result in a lot of troubles, such as low coupling efficiency due to absorption and reflection, transverse inhomogeneity, and low confinement coefficients of driving and probe beams. From the application point of view, electrical pumping is more applicable. A. Belyanin *et al.* proposed a LWI scheme with self-generated driving field in a ladder type three-level system [64]. Therefore the optical driving and probe would be generated in the same active medium.

LWI could be very useful in situations where population inversion is difficult to achieve or maintain due to ultra fast relaxation or inefficient pumping. The examples

include high frequency ultraviolet, x-ray, gamma ray lasers [114], and THz lasers which were discussed in section 2. Without any doubt, the topic of realizing THz laser based on a LWI scheme is very attractive.

The scheme of LWI with self-generated driving field is a chosen to implement the LWI scheme for THz radiation in this thesis. As discussed in previous sections, cascade quantum-well structures and QCLs can be modified and have great flexibility to design suitable transition as we need.

6.2 The Upper Ladder Scheme of LWI and the Basic Equations

We chose an upper ladder scheme to realize the LWI for THz radiation within, as shown in Fig. 6.2. The theoretical possibility of THz lasing is investigated.

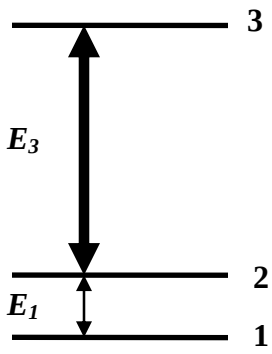

Fig. 6.2. The upper ladder scheme of a three-level system. A strong driving field E_3 generated between the transition 3-2 leads generation of field at 2-1 in THz range without population inversion of 2-1.

In this scheme, a strong pump field on E_3 is generated at transition 3-2, and field E_1 is induced without population inversion between energy states 2 and 1. Following the Ref. [64], the analysis is based on Maxwell equations and coupled density-matrix equations. All the optical fields and polarizations are represented by a series corresponding orthonormal set of cavity modes F_λ and slowly varying complex amplitudes. The electric field is expressed as:

$$E_j(r,t) = \sum_\lambda \frac{1}{2}\varepsilon_j(t)F_{j\lambda}(r)\exp(-i\omega_j t) + c.c. \qquad (6.1)$$

where j is the index of polarization, λ is the index of cavity mode. The corresponding wave equation can be expressed in term of complex Rabi frequency $e(t)$, for example of field e_1

$$\frac{de_1}{dt} + \kappa_1 e_1 = \frac{2\pi i \omega_{c1} d_{12}^2 N}{\hbar n_{eff1}^2} \int \sum \sigma_{21} F_{1\lambda}(r) dr \ , \qquad (6.2)$$

where the Rabi frequency $e(t) = d\varepsilon(t)/2\hbar$, κ_1 is the cavity loss, ω_{c1} is the frequency of cavity mode, d_{12} is the dipole moment of transition between states 1 and 2, N is the total volume density of electrons, n_{eff1} is the effective refractive index of the cavity mode for field e_1, and σ_{21} is one of the slowly varying amplitude of the off-diagonal elements of the density matrix.

In the three-level system, σ_{21} can be obtained by solving the density matrix equations,

$$d\sigma_{21}/dt + \Gamma_{21}\sigma_{21} = ie_1 n_{12} - ie_2\sigma_{32}^* + ie_3^*\sigma_{31} \ , \qquad (6.3)$$

$$d\sigma_{31}/dt + \Gamma_{31}\sigma_{31} = ie_2 n_{13} - ie_1\sigma_{32}^* + ie_3^*\sigma_{21} \ , \qquad (6.4)$$

$$d\sigma_{32}/dt + \Gamma_{32}\sigma_{32} = ie_3 n_{21} - ie_1\sigma_{31}^* + ie_2^*\sigma_{21} \quad , \tag{6.5}$$

where $n_{ik}=\rho_{ii}-\rho_{kk}$, and

$$\Gamma_{21} = \gamma_{21} + i(\omega_{21} - \omega_{c1}) \quad , \tag{6.6}$$

$$\Gamma_{31} = \gamma_{31} + i(\omega_{31} - \omega_{c2}) \quad , \tag{6.7}$$

$$\Gamma_{32} = \gamma_{32} + i(\omega_{32} - \omega_{c3}) \quad , \tag{6.8}$$

where γ_{ik} is the broadening factor of transition between states i and k and is replaced by common broadening factor of 5 meV, $\omega_{ik}=(E_i-E_k)/\hbar$ is the energy difference between states i and k.

In order to obtain the information of the population at each energy state, we solved the coupled equations of population. Given an open three-level system, with the absence of field e_2 which is resonant to transition 3-1, the density-matrix equations for population ρ_{ii} at ith state can be written as

$$d\rho_{11}/dt = -2\,\mathrm{Im}[e_1^*\sigma_{21}] + j_1 + r_{21}\rho_{22} + r_{31}\rho_{33} - r_1\rho_{11} \quad , \tag{6.9}$$

$$d\rho_{22}/dt = 2\,\mathrm{Im}[e_1^*\sigma_{21}] - 2\,\mathrm{Im}[e_3^*\sigma_{32}] + j_2 + r_{32}\rho_{33} - r_{21}\rho_{22} - r_2\rho_{22} \quad , \tag{6.10}$$

$$d\rho_{33}/dt = 2\,\mathrm{Im}[e_3^*\sigma_{32}] + j_3 - r_{31}\rho_{33} - r_{32}\rho_{33} - r_3\rho_{33} \quad , \tag{6.11}$$

where r_{ik} is the relaxation rate from state i to k, r_i is the relaxation rate from state i to anywhere else, and j_i is the injection rate of electrons to the state i.

A net gain of field e_1 can be achieved with a strong driving field of e_3. If the system is under steady condition of operation, all the terms of time derivative should be vanished. Therefore, for the solution of steady state, σ_{21} can be obtained by solving Eq. (6.3-6.5) after some approximations,

$$\sigma_{21} = ie_1(n_{12} + \frac{|e_3|^2 n_{23}}{\Gamma_{32}\Gamma_{31}})/(\Gamma_{21} + \frac{|e_3|^2}{\Gamma_{31}}) \ , \qquad (6.12)$$

where the quadratic terms of weak field e_1 are ignored. We can then just plug it into Eq. (6.2), and obtain the optical gain g_1 of field e_1 as

$$g_1 = \mathrm{Re}[\zeta \cdot \frac{(n_{21} + |e_3|^2 n_{32}/\Gamma_{32}\Gamma_{31})}{\Gamma_{21} + |e_3|^2/\Gamma_{31}}] \ , \qquad (6.13)$$

where

$$\zeta = \frac{2\pi\omega_{c1}d_{12}^2 N}{\hbar n_{eff1}^2}\int\sum F_{1\lambda}(r)dr \ , \qquad (6.14)$$

As we proposed above, the transition 3-2 is a self generated laser transition, namely a strong population inversion exists between 3-2. Therefore, it is reasonable to assume that almost all the population of electron in the system is located at state 3, nearly no electrons are located at state 2 or 1. In this case, the population difference of 2-1 $n_{21} \rightarrow 0$. Even if there is no population inversion between states 2 and 1, a positive gain for field e_1 is still can be achieved with strong driving field of e_3. This condition happens to be fulfilled when lasing at transition 3-2. A gain without population inversion at 2-1 is then obtained. When the net gain is strong enough to overcome the waveguide loss, the field e_1 starts to lase without population inversion at transition 2-1.

The LWI scheme for THz radiation is different from the DFG process as discussed in section 2. The gain in LWI scheme must overcome the waveguide loss, otherwise no light radiation will be generated. At the same time, when the threshold is reached, the THz radiation in the LWI scheme is expected to be more powerful than in

the DFG process In the DFG process, there is no 'gain' factor for THz radiation. As long as there are two pumping fields for DFG process, the THz signal will be generated no matter how large the waveguide loss is, although the THz signal could be too weak to be detected.

Let us take a close look at Eq. (6.13). We know that e_3 and n_{32} are related when lasing happens at transition 3-2. The relationship can be obtained by solving the density matrix equations (6.5) and (6.10-6.11), where all carriers are assumed only be pumped to the state 3. After a little approximation, the relationship can be expressed as

$$\left|e_3\right|^2 n_{32} = \frac{\left|\Gamma_{32}\right|(r_2 + r_{21})(r_3 + r_{31} + r_{32})}{2(r_2 + r_{21} + r_3 + r_{31})}(n_{32}^* - n_{32}) \cong \frac{\left|\Gamma_{32}\right|r_3^{'}}{2} R n_{32}^* , \qquad (6.15)$$

where $r_3+r_{31}<<r_2+r_{21}$ is an reasonable assumption for achieving population inversion at 3-2, which is the condition of lasing at transition 3-2, r_3' is the inverse of total life time of state 3. We introduced a parameter R, where $R=(n_{32}^*-n_{32})/n_{32}^*$, and n_{32}^* is the population difference between states 3 and 2 if no lasing happens with the same pumping current. It can expressed as

$$n_{32}^* = j_3 \frac{r_2 + r_{21} - r_{32}}{(r_2 + r_{21})r_3^{'}} . \qquad (6.16)$$

Usually in a typical laser system, the parameter R is estimated as 0.9. With this value, we can simplify the process to estimate the optical gain of e_1.

Based on the idea of LWI and the ladder scheme, a QCL structure is designed. The QCL has an active region which supports lasing at mid-IR wavelengths which serves as a driving field, and also a ladder type three-level system which satisfies the requirement discussed above. In a QCL, usually the value of n_{32}^* highly depends on the

doping rate in the injectors and the current density. Given a typical doping rate around 10^{17} cm^{-3}, a reasonable estimation of $N \cdot n_{32}^{*}$ is around $5*10^{16}$ cm^{-3}. More detailed discussions are in the following section.

6.3 The Quantum-Well Structure of a QCL for LWI at THz

As indicated in Eq. (6.13), the optical gain of lower transition in the scheme is proportional to the intensity of the driving field. A powerful QCL is needed to provide a strong driving field. We chose a 'bound-to-continuous' type design of QCL [29] and a mature GaInAs/AlInAs material system which is lattice matched to the InP substrate. The QCL is re-designed with proper quantum-well structure containing the ladder type three-level system discussed above. The sequence of thickness of wells and barriers is 41/24/8/68/10/61/8/56/8/50/14/43/15/37/21/42/22/39/24/38/26/39, which starts from injector barrier. The band diagram of the structure under a bias of 43 kV/cm is shown in Fig. 6.3, where the bold lines are the ladder type three-level system for LWI process.

The structure is similar to a typical bound-to-continuum QCL. A strong dipole moment between 3-2 of 33.7Å promises a driving field lasing at transition 3-2, with the photon energy of 117 meV (about 10.6 μm). The adjustments made for LWI scheme include strong dipole moments between 2-1, and resonant LO phonon scattering for both states 2 and 1 to lower energy levels [115]. The former promises a strong optical gain, as

based on Eq. (6.14). The later promises the electron populations of states 2 and 1 vanish due to an ultrafast depleting rate of resonant phonon scattering [115].

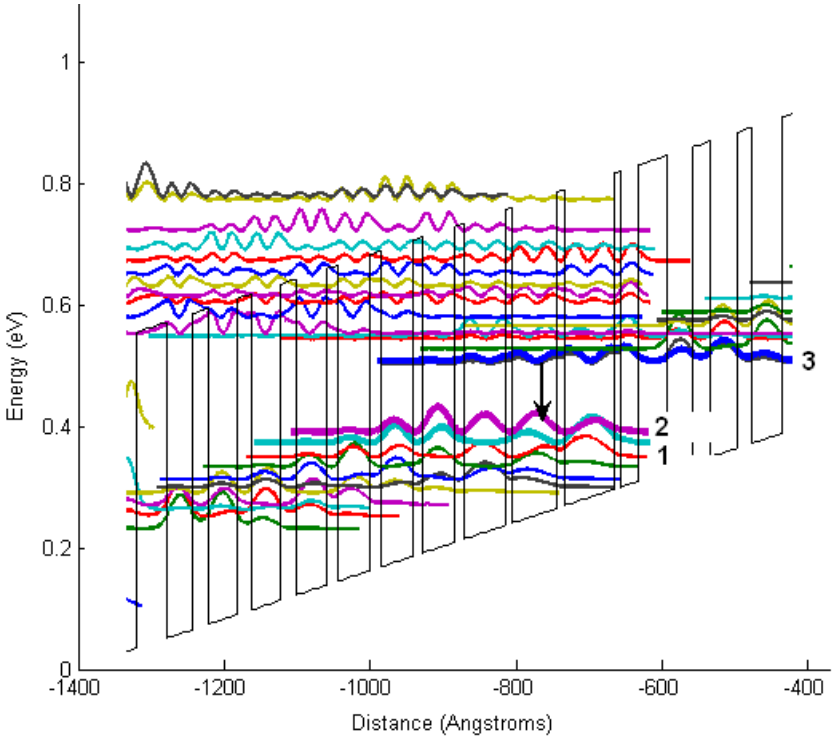

Fig. 6.3. The band structure under applied electric field of 43 kV/cm. The bold lines labeled with numbers are the three-level system for LWI process. The driving laser transition is 3-2, with a transition energy of 117 meV. The energy separation of 2-1 is 18 meV, corresponding a THz radiation of 69 μm.

To evaluate the gain of e_1, we must estimate the value of n_{32}^*, based on Eq. (6.15-6.16). We list all the life time of transitions in table 6.1. The life time of level 2 τ_2 ($1/r_2$) and the life time of level 1 are both very small, as mentioned above, due to resonant phonon scattering to lower levels. Therefore, the population difference between states 1 and 2, n_{21}, can be ignored on Eq. (6.13). The energy difference between level 1

and 2, $\hbar\omega_{21}$, is about 18 meV, and the dipole moment of transition 2-1 is 87 Å. Plugging all the parameters into Eq. (6.13-6.15), we obtained the gain of e_1 about 83 cm^{-1}.

Table 6.1. The life time of transitions from level 1, 2 and 3. (*) The energy difference between 1 and 2 is smaller than resonant LO phonon energy. The transition is dominated by electron-electron scattering, and the life time of transition is at range of 5-50 ps [116].

	τ_{32}	τ_{31}	τ_3	τ_{21}	τ_2	τ_1
(ps)	9.0	5.9	2.56	$5^{(*)}$	0.25	0.33

6.4 The Waveguide Design for THz Radiation

Due to the free carrier loss in a doped semiconductor material, a THz field usually faces strong waveguide loss in those materials. The regular waveguide design for mid-IR QCL, as shown in section 2, is suitable for THz radiation. There are mainly two types of waveguide design for THz emission at the same semiconductor material system, the metal to metal waveguide and the 2-dimensional surface plasmon waveguide, as shown in Fig. 6.4 [117].

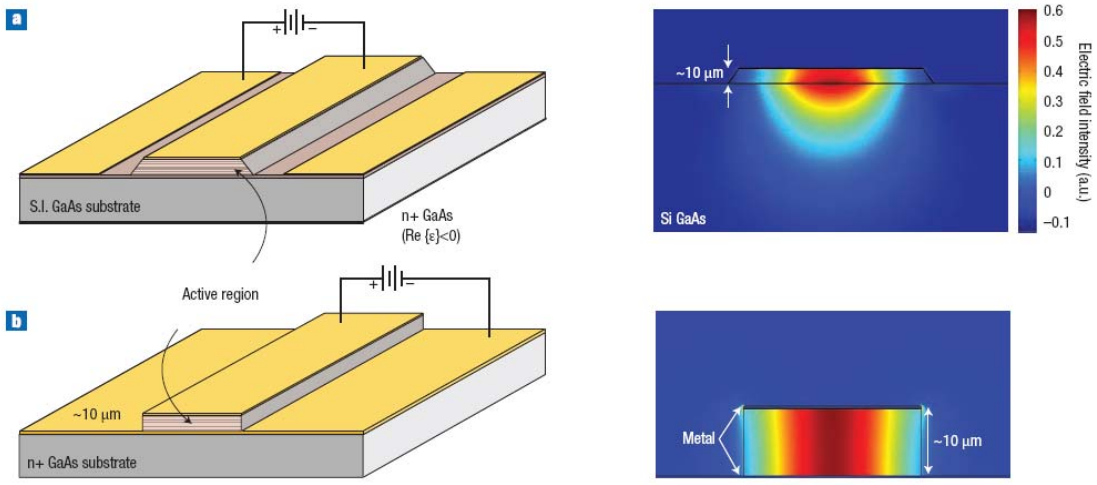

Fig. 6.4. The scheme of (a) the semi-insulator (SI) surface plasmon waveguide, and (b) the metal-metal waveguide structures [57]. The left figures are the field mode profiles in the waveguides.

In the metal-metal waveguide, the active region is sandwiched between two metal contacts. The mode is confined by the surface plasmon at the metal semiconductor interfaces. A very large confinement factor about 90% can be achieved with this waveguide structure. In the semi-insulator (SI) surface plasmon waveguide, the top of the waveguide is still a metal contact, but between the active region and substrate there is a thin and highly doped layer or heterostructure forms a 2-D electron gas (2DEG) [118-119], which serves as a bottom contact layer for a side contact. With the side contact, we do not need to dope the substrate any more. Although the confinement factor in the SI surface plasmon waveguide would be less than that of metal-metal waveguide, the modes profile of THz frequency will experience relatively lower waveguide loss.

In our case, a SI surface plasmon waveguide is chosen. An active core of QCL discussed above with about 50 periods of active region is about 4 μm thick. A 2DEG layer about 160 nm thick is grown between the active core and SI substrate [119]. As a result, the average complex refractive index of the active region is about 4.16+0.053i with averaged doping rate of 5×10^{15} cm^{-3}, and the refractive index in the SI substrate is about 3.65+0.00015i, which means much smaller loss than that of active region. The mode profile is shown in Fig. 6.5. We obtained the waveguide loss about 33 cm^{-1}, and a confinement factor of the mode at active core about 60%.

For a summary, we obtained a gain of 83 cm^{-1} against waveguide loss of 33 cm^{-1} in the LWI process at wavelength of 69 μm in a bound-to-continuum QCL driving at wavelength of 10.6 μm.

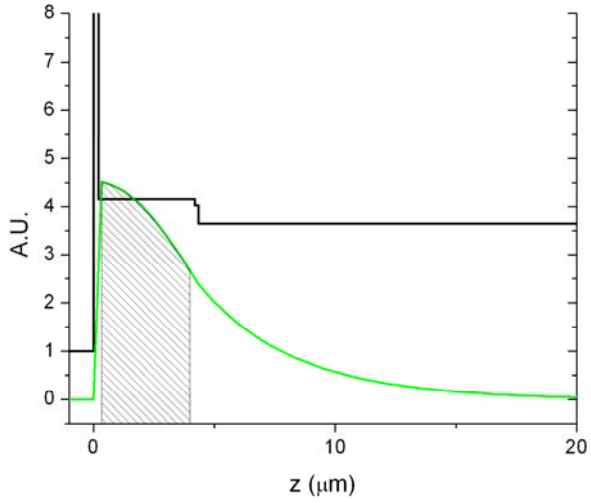

Fig. 6.5. The refractive index profile (the black line), and the TM mode profile (green line) with a 2DEG surface plasmon waveguide. The shadowed area is the part of the mode profile within the active core.

7. SUMMARY AND FUTURE WORK

Resonant nonlinearities within cascade quantum-well systems are interesting topic to research on. Various projects has been carried on or proposed.

The difference frequency generation with QCL for room temperature terahertz radiation was successfully demonstrated with the highest operation temperature around 250K. A peak power of THz of 1.5 μW is achieved at 80K.

The second harmonic generation QC lasers for near-IR light generation are discussed. Device D3056 showed interesting phenomena. The nonlinear power conversion efficiency increased with pump current. An analysis was given, and two explanations were given. One is populations change due to the change of current density caused the nonlinear susceptibility change, and the other is the change of the dipole moments among the three-level system due to applied electric field change caused the nonlinear susceptibility change.

A scheme of in-plane integration of optical nonlinearities with QCL is proposed. Giant nonlinear susceptibilities and great tunability can be achieved. By implement Raman scattering within this scheme, widely tunable lasers is proposed. A tunability of more than 25 meV can be achieved.

A frequency up-conversion scheme for mid/far-IR light detection is also proposed in the thesis. By converting mid-IR signal into near-IR range with a sum frequency generation process in a nonlinear quantum-well structure, we can employ

superior near-IR photo detector, such as Si APD. The figure of merits lies on very low noise equivalent power (NEP) and high detectivity of the system.

Moreover, a lasing without inversion (LWI) based on upper ladder scheme for THz emission is discussed. A three-level upper ladder system was embedded into a QCL working at 10 μm, which served as an internal driving field. A THz emission at 69 μm in the LWI is expected. We obtained the optical gain of THz signal about 80 cm^{-1}, with an optimized waveguide loss of 30 cm^{-1}.

Further research is needed to improve those schemes. For the THz DFG QCL, higher efficiency or nonlinear susceptibility in active region is needed, and lower losses in materials and waveguides are anticipated. Although operation at room temperature is already achieved in our research but higher power of THz radiation is required or practical application. Moreover, higher tunability could be achieved in the in-plane integration scheme with higher conversion efficiency and real sample device should be built and tested; and the experiments of mid/far-IR light detection in up-conversion scheme should be carried out and improved.

REFERENCES

[1] R. W. Boyd, *Nonlinear Optics*, Second Edition (Academic, New York, 2003).

[2] Y. R. Shen, *The Principles of Nonlinear Optics* (Wiley, New York, 1984).

[3] E. Rosencher, B. Vinter, and B. Levine, Eds., *Intersubband Transitions in Quantum Wells.* (Springer, London, 1992).

[4] H. C. Liu, B. F. Levine, and J. Y. Andersson, Eds., *Quantum Well Intersubband Transition Physics and Devices.* (Dordrecht, Netherlands: Kluwer, 1994).

[5] E. O. Kane, *Physics of III-V Compounds, Semiconductors and Semimetals*, edited by R. K. Willardson and A. C. Beer (Academic, New York, 1966), Vol. 1, p. 75.

[6] R. Q. Yang, and J. M. Xu, Phys. Rev. B. **50**, 7474 (1994).

[7] C. G. Bethea, B. F. Levine, V. 0. Shen, R. R. Abbott, and S. J. Hsieh, IEEE Trans. Electron. Devices, **38**, 1118 (1991).

[8] R. P. G. Kmnasiri, Y. J. Mii, and K. L. Wang, IEEE Electron Device Lett. **11**, 227 (1990).

[9] M. K. Gumick and T. A. De Temple, IEEE J. Quantum Electron. **QE-19**, 791 (1983).

[10] M. M. Fejer, S. J. B. Yoo, R. L. Byer, A. Harwit, and I. S. Harris, Phys. Rev. Lett. **62**, 1041 (1989).

[11] E. Rosencher and P. Bois, Phys. Rev. B, **44**, 11315 (1991).

[12] P. Boucaud, F. H. Julien, D. D. Yang, J. M. Lourtioz, E. Rosencher, P. Bois, and J. Nagle, Appl. Phys. Lett. **57**, 215 (1990).

[13] P. Boucaud, F. H. Julien, D. D. Yang, J. M. Lourtioz, E. Rosencher, and P. Bois, Opt. Lett. **16**, 199 (1991).

[14] S. J. B. Yoo, M. M. Fejer, R. J. Byer, and J. S. Harris, Jr., Appl. Phys. Lett. **58**, 1724 (1991).

[15] E. Rosencher, P. Bois, J. Nagle, E. Costard, and S. Delaitre, Appl. Phys. Lett. **55**, 1597 (1989).

[16] E. Rosencher, P. Bois, B. Vinter, J. Nagle, and D. Kaplan, Appl. Phys. Lett. **56**, 1822 (1990).

[17] H. C. Liu, E. Costard, E. Rosencher, and J. Nagle, IEEE J. Quantum Electron. **31**, 1659, (1995).

[18] M. J. Shaw and M. Jaros et al. Phys. Rev. B **50**, 18395 (1994).

[19] Federico Capasso, Carlo Sirtori, and Alfred Y. Cho, IEEE J. Quantum Electron. **30**, 1313, (1994).

[20] E. Rosencher, A. Fiore, B. Vinter, V. Berger, Ph. Bois, J. Nagle, Science **271,** 12 (1996).

[21] R. F. Kazarinov, and R. A. Suris, Sov. Phys. Semicond. **5**, 207 (1971); F. Capasso, K. Mohammed, A. Y. Cho, IEEE J. Quantum Electron. **22,** 1853, (1986).

[22] J. Faist, F. Capasso, D. L. Sivco, C. Sirtori, and A. L. Hutchinson *et al.* Science **264**, 553 (1994).

[23] J. Faist, F. Capasso, C. Sirtori, D. L. Sivco, J. N. Baillargeon, A. L. Hutchinson, S-N. G. Chu, and A. Y. Cho, Appl. Phys. Lett. **68**, 3680 (1996).

[24] C. Gmachl, F. Capasso, J. Faist, A. L. Hutchinson, A. Tredicucci, *et al.* Appl. Phys. Lett. **72**, 1430 (1998).

[25] R. Q. Yang, B. H. Yang, D. Zhang, C.-H. Lin, S. J. Murry, H. Wu, and S. S. Pei, Appl. Phys. Lett. **71**, 2409 (1997).

[26] J. Faist, A. Tredicucci, F. Capasso, C. Sirtori, D. L. Sivco, *et al.* IEEE J. Quantum Electron. **34**, 336 (1998).

[27] C. Gmachl, A. Tredicucci, F. Capasso, A. L. Hutchinson, D. L. Sivco, J. N. Baillargeon, and A. Y. Cho, Appl. Phys. Lett. **72**, 3130 (1998).

[28] A. L. Hutchinson, and A. Y. Cho, Opt. Lett. **23**, 1366 (1998).

[29] R. Maulini, M. Beck, and J. Faist, Appl. Phys. Lett. **84**, 1659 (2004).

[30] J. S. Yu, A. Evans, J. David, L. Doris, S. Slivken, and M. Razeghi, Appl. Phys. Lett. **83**, 5136 (2003).

[31] J. S. Yu, S. Slivken, A. Evans, L. Doris, and M. Razeghi, Appl. Phys. Lett. **83**, 2503 (2003).

[32] L. Ajili, G. Scalari, and J. Faist, Appl. Phys. Lett. **85**, 3986 (2004).

[33] J. S. Yu, S. Slivken, S. R. Darvish, A. Evans, B. Gokden, and M. Razeghi, Appl. Phys. Lett. **87**, 041104 (2005).

[34] A. Evans, J. S. Yu, J. David, L. Doris, K. Mi, S. Slivken, and M. Razeghi, Appl. Phys. Lett. **84**, 314 (2004).

[35] J. Devenson, O. Cathabard, R. Teissier, and A. N. Baranov, Appl. Phys. Lett. **91**, 251102 (2007).

[36] K. Ohtani and H. Ohno, Appl. Phys. Lett. **82**, 1003 (2003).

[37] H. Yasuda, I. Hosako, S. Miyashita and M. Patrashin, Electronics Letters **41,** 19 (2005).

[38] R. Teissier, D. Barate, A. Vicet, C. Alibert, and A. N. Baranov *et al.*, Appl. Phys. Lett. **85**, 167 (2004).

[39] J. Devenson, R. Teissier, O. Cathabard, and A. N. Baranov, Appl. Phys. Lett. **90**, 111118 (2007).

[40] Q. Yang, C. Manz, W. Bronner, K. Köhler, and J. Wagner, Appl. Phys. Lett. **88**, 121127 (2006); Appl. Phys. Lett. **91***,* 251102 (2007).

[41] Z. Liu, C. F. Gmachl, L. Cheng, F. Choa, F. J. Towner, X. Wang, and J. Fan, IEEE J. Quantum Electron. **44**, 485 (2008).

[42] J. S. Yu, S. Slivken, A. Evans, J. David, and M. Razeghi, Appl. Phys. Lett. **82**, 3397 (2003).

[43] S. Kumar, B. S. Williams, and Q. Hu, Appl. Phys. Lett. **88**, 121123 (2006).

[44] C. Sirtori, C. Gmachl, F. Capasso, J. Faist, D. L. Sivco, B. S. Williams, S. Kumar, H. Callebaut, and Q. Hu, Appl. Phys. Lett. **83**, 2124 (2003).

[45] H. Luo S. R. Laframboise, Z. R. Wasilewski, G. C. Aers, and H. C. Liu, Appl. Phys. Lett. **90**, 41112 (2007).

[46] Z. Liu, "Room-Temperature Continuous-Wave Quantum Cascade Lasers in the First and Second Atmospheric Windows" Ph.D. thesis, Princeton University, (2008).

[47] M. Troccoli, A. Belyanin, F. Capasso, E. Cubukcu, D. L. Sivco and A. Y. Cho, Nature **433**, 845 (2005).

[48] N. Owschimikow, C. Gmachl, A. Belyanin, V. Kocharovsky, R. Colombelli, F. Capasso, and A. Y. Cho, Phys. Rev. Lett. **90**, 43902 (2003).

[49] C. Gmachl, A. Belyanin, D. L. Sivco, F. Capasso, and A. Y. Cho, *et al.* IEEE J. Quantum Electron. **39**, 1345 (2003).

[50] J.-Y. Bengloan, A. De Rossi, V. Ortiz, X. Marcadet, and M. Calligaro *et al.* Appl. Phys. Lett. **84**, 2019 (2004).

[51] M. A. Belkin, F. Capasso, A. Belyanin, D. L. Sivco, Nature Photonics **1,** 288 (2007).

[52] H. C. Liu, Iva W. Cheung, A. J. SpringThorpe, C. Dharma-wardana, and Z. R. Wasilewski, *et al.*, Appl. Phys. Lett. **78,** 3580 (2001).

[53] M. A. Belkin, M. Troccoli, L. Diehl, A. Belyanin, and F. Capasso, Appl. Phys. Lett. **88,** 201108 (2006).

[54] *Wikipeida* http://en.wikipedia.org/wiki/Terahertz#cite_note-1, "accessed on Nov. 3 2008".

[55] R. Kohler, A. Tredicucci, F. Beltram, H. E. Beere, E. H. Linfield, A. G. Davies, *et al.* Nature **417**, 156 (2002).

[56] B. S. Williams, H. Callebaut, S. Kumar, and Q. Hu, Appl. Phys. Lett. **82,** 1015 (2003).

[57] B. S. Williams, Nature Photonics **1,** 517 (2007).

[58] M. Rochat, L. Ajili, H. Willenberg, and J. Faist, Appl. Phys. Lett. **81**, 1381 (2002).

[59] C. Sit-tori, F. Capasso, J. Faist, L. N. Pfeiffer, and K. W. West, Appl. Phys. Lett. **65,** 445 (1994).

[60] I. Tomita, H. Suzuki, H. Ito, H. Takenouchi, K. Ajito, *et al.,* Appl. Phys. Lett. **88,** 71118 (2006).

[61] K. L. Vodopyanov, M. M. Fejer, X. Yu, J. S. Harris, Y.-S. Lee, *et al.* Appl. Phys. Lett. 89, 141119 (2006).

[62] A. Straub, T. S. Mosely, C. Gmachl, R. Colombelli, M. Troccoli, *et al.* Appl. Phys. Lett. **80**, 2845 (2002).

[63] K. J. Franz, D. Wasserman, A. J. Hoffman, D. C. Jangraw, Appl. Phys. Lett. **90**, 91104 (2007).

[64] A. Belyanin, C. Bentley, F. Capasso, O. Kocharovskaya, and M. O. Scully, Phys. Rev. A **64**, 013814 (2001).

[65] M. A. Belkin, F. Capasso, F. Xie, A. Belyanin, M. Fischer, Appl. Phys. Lett. **92**, 201101 (2008).

[66] O. Malis, A. Belyanin, C. Gmachl, D. L. Sivco, M. L. Peabody, A. M. Sergent, Appl. Phys. Lett. **84**, 2721 (2004).

[67] X. Marcadet, V. Ortiz, J-Y. Bengloan, S. Dhillon, M. Calligaro, and C. Sirtori, J. Vac. Sci. Technol. B **22**, 1558 (2004).

[68] D. Qu, F. Xie, G. Shu, S. Momen, E. Narimanov, and C. F. Gmachl, Appl. Phys. Lett. **90**, 31105 (2007).

[69] M. O. Scally and M. S. Zubairy, *Quantum Optics* (Cambridge Univ. Press, Cambridge, 1997).

[70] L. R. Ram-Moham, K. H. Yoo, and R. L. Aggarwal, Phys. Rev. B **38**, 6151 (1988).

[71] F. Xie, V. R. Chaganti, D. Smith, A. Belyanin, F. Capasso, and C. Gmachl, Laser Phys. **17**, 672 (2007).

[72] B. N. Zvonkov, A. A. Biryukov, A. V. Ershov, S. M. Nekorkin, V. Ya. Aleshkin, *et al.,* Appl. Phys. Lett. **92**, 21122 (2008).

[73] G. Sun, J. Khurgin, L. Friedman, and R. A. Soref, J. Opt. Soc. Am. B **15**, 648 (1998).

[74] J. L. Pan, C. G. Fonstad Jr., Mat. Sci. Eng. **28**, 65 (2000).

[75] J. Y. Andersson, L. Lundqvist, and F. Paska, Appl. Phys. Lett. **58**, 2264 (1991).

[76] L. C. West and S. J, Eglash, Appl. Phys. Lett. **46**, 1156 (1985).

[77] C-L. Yang, D-S. Pan, and R. Somoano, J. Appl. Phys. **65**, 3253 (1989).

[78] G. Hasnain, B. F. Levine, C. G. Bethea, R. A. Logan, J. Walker, and R. J. Malik, Appl. Phys. Lett. **54**, 2515 (1989).

[79] K. W. Goossen, S. A. Lyon, and K. Alavi, Appl. Phys. Lett. **53**, 1027 (1988).

[80] L. C. Chiu, J. S. Smith, S Margaht, A. Yariv, and A. Y. Cho. Infrared Phys. **23**, 93

(1983).

[81] A. Pinczuk, D. Heiman, F Sooryakumar, A. C. Gossard, and W. Wiegmann, Surf. Sci. **170**, 573 (1986).

[82] R. P. G. Karunasiri, J. S. Park, Y. J. Mii, and K. L. Wang, Appl. Phys. Lett. **57**, 2585 (1990).

[83] B. F. Levine, S. D. Gunapala, J. PA. Kuo, S. S. Pei, and S. Hui, Appl. Phys. Lett. **59**, 1864 (1991).

[84] R. T. Rurqda and E. Garmire, Infrared Phys. **34**, 153 (1993).

[85] A. K. Wojcik, F. Xie, V. R. Chaganti, A. Belyanin and J. Kono, J. Mod. Opt., submitted.

[86] J. E. Midwinter, J. Appl. Phys. Lett. **12,** 68 (1968).

[87] R. Boyd, C. Townes, Appl. Phys. Lett. **31,** 440 (1977).

[88] J. Zhuang, L. Liang, H. H. Y. Sung, Inorg. Chem. **46,** 5404 (2007).

[89] K. Cimatu and S. Baldelli, J. A. Chem. Soc. **130**, 8030 (2008).

[90] C. Langrock, E. Diamanti, R.V. Roussev, Y. Yamamoto, M. M. Fejer, *et al.* Opt. Lett. **30**, 1725 (2005).

[91] R. T. Thew, S. Tanzilli, L. Krainer, S. C. Zeller, A. Rochas, I. Rech, S. Cova, H. Zbinden, *et al.* New J. Phys. **8**, 32 (2006).

[92] E. Damn, L. E. Bausl, R. Legros, C. Fontaine and J. G. Sole, Solid State Comm. **94**, 379 (1995).

[93] K. Karstad, A. Stefanov, M. Wegmuller, Opt. Lasers Eng. **43**, 537 (2005).

[94] G. Temporao, S. Tanzilli, H. Zbinden, T. Aellen, M. Giovannini, *et al.* Opt. Lett. **31**, 1084 (2006).

[95] L. Nevou, M. Tchernycheva, F. Julien, M. Raybaut, A. Godard, *et al.* Appl. Phys. Lett. **89,** 151101 (2006).

[96] S. Pellegrini, R. E. Warburton, L. J. J. Tan, J. S. Ng, A. B. Krysa, K. Groom, J. P. R. David, S. Cova, M. J. Robertson, *et al.* IEEE J. Quantum Electron **42**, 397 (2006).

[97] F. Raissia, and N. A. Sheeni, Sensors and Actuators A **104**, 117 (2003).

[98] S. E. Harris, Phys. Rev. Lett. **62**, 1033 (1989); S. E. Harris, and J. J. Macklin, Phys. Rev. A **40**, 4135 (1989).

[99] O. Kocharovskaya and Ya. I. Khanin, JETP Lett. **48**, 630 (1988); O. Kocharovskaya and P. Mandel, Phys. Rev. A **42**, 523 (1990).

[100] V.G. Arkhipkin and Y. I. Heller, Phys. Lett. **98A**, 12 (1983).

[101] M. O. Scully, Phys. Rev. Lett. **67**, 1855 (1991).

[102] S. E. Harris, J. E. Field, and A. Imamoglu, Phys. Rev. Lett. **64**, 1107 (1990).

[103] A. Imamoglu, J. E. Field, and S. E. Harris, Phys. Rev. Lett. **66**, 1154 (1991).

[104] Y. V. Radeonychev, M.A.Erukhimova, O.A.Kocharovskaya, and R.Vilaseca, Radiophy. and Quant. Electron. **47**, 795 (2004).

[105] J. Mompart and R. Corbalan, J. Opt. B **2**, R7 (2000).

[106] A. Nottelmann, C. Peters and W. Lange, Phys. Rev. Lett. **70,** 1783 (1993).

[107] E. S. Fry, X. Li, D. Nikonov, G. G. Padmabandu, M. O. Scully, A. V. Smith, F. K. Tittel, C. Wang, S. R. Wilkinson and S. Y. Zhu, Phys. Rev. Lett. **70,** 3235 (1993).

[108] V. D. Veer, V. Diest, A. Onszelmann and V. Linden, V. den Heuvell, Phys. Rev. Lett. **70,** 3243 (1993).

[109] A. S. Zibrov, M. D. Lukin, D. E. Nikonov, L. W. Hollberg, M. O. Scully, V. L. Velichansky, H. G. Robinson, Phys. Rev. Lett. **75**, 1499 (1995).

[110] H. K. Holt, Phys. Rev. A **16,** 1136 (1977).

[111] B. R. Mollow, Phys. Rev. A **5,** 2217 (1972).

[112] M. O. Scully, S. Y. Zhu and A. Gavrielides, Phys. Rev. Lett. **62,** 2813 (1989).

[113] J. Mompart, R. Corbalan, and R.Vilaseca, Radiophy. Quant. Electron. **47**, 783 (2004).

[114] H. Schmidt, D. E. Nikonov, K. L. Campman, K. D. Maranowski, A. C. Gossard, *et al.* Laser Phys. **9**, 797 (1999).

[115] B. S. Williams and Q. Hu, J. Appl. Phys. **90,** 5504, (2001).

[116] P. Hyldgaard and J. W. Wilkins, Phys. Rev. B. **53,** 6889 (1996).

[117] S. Kohen, B. S. Williams, and Q. Hu, J. Appl. Phys. **97,** 53106, (2005).

[118] C. Sirtori, C. Gmachl, F. Capasso, J. Faist, D. Sivco, A. L. Hutchinson, and A. Y. Cho, Opt. Lett. **23**, 1366 (1998).

[119] L. Ajili, G. Scalari, N. Hoyler, M. Giovannini, and J. Faist, Appl. Phys. Lett. **87,** 141107 (2005).

VITA

Feng Xie received his Bachelor of Science degree in applied physics and Master of Science degree in physics from the University of Science and Technology of China at Hefei, China in 2000 and 2003 respectively. He entered the applied physics program at Texas A&M University in September 2003. His research interests include nonlinear optics, and semiconductor opto-electronics.

Mr. Xie may be reached at Corning Inc., Painted Post, NY 14870. His email is fxie@tamu.edu and xief@corning.com.